

Mathematical Modeling of Cell Migration  
*Mechanisms in Dictyostelium discoideum*

A Dissertation  
SUBMITTED TO THE FACULTY OF THE  
UNIVERSITY OF MINNESOTA  
BY

Bryan A. Félix

IN PARTIAL FULFILLMENT OF THE REQUIREMENTS FOR THE DEGREE OF  
DOCTOR OF PHILOSOPHY

Hans G. Othmer

March 2023

Copyright © 2023 Bryan A. Félix. All rights reserved.

*Dedicated to the memory of my grandmothers*

GREGORIA ROACHO AND ADELAIDA LUGO.

## Acknowledgements

I extend my gratitude to Professor Hans Othmer, my advisor, who has been a source of inspiration to me. Through his guidance and example, I have learned to hold myself to high standards, think deeply about problems, and never settle with a superficial understanding. I feel fortunate to have worked with him and his amazing team of researchers.

I would also like to extend a heartfelt thank you to my undergraduate mentor, Professor Anne Shiu. It was because of her that I even considered graduate school, and I am forever grateful for the lessons she taught me. I learned from her that persistence is key and that results are just a byproduct. And from her I also discovered the importance of clear scientific communication and the joy of technical writing.

I extend my gratitude to my family for their support. They have been a constant source of encouragement and motivation throughout this journey, reminding me of my achievements and pushing me to go forward. My brother, Kevin, deserves a special mention for his help with debugging my scripts and improving this manuscript with his expertise in L<sup>A</sup>T<sub>E</sub>X. I am also thankful for the support and advice of my sister, Melissa, and my parents Martha Granados and Adan Félix.

I express my appreciation to the members of my committee - Professors Duane, Jasmine, and Jia - for their valuable comments and support. I am grateful for the many letters of recommendation they wrote to further my career. This manuscript has improved greatly thanks to their input.

I am deeply grateful to Finola Kane-Grade for helping me re-discover my love of learning and curiosity. She taught me the importance of a calm and compassionate approach to

life, and showed me that happiness can be found beyond academia. I am truly thankful for the impact she has had on my life.

I am grateful for the wonderful friends I have. Their love and appreciation mean the world to me, and I am honored to have them in my life. Special thanks to María I. Sanchez, Chen Shi, Ty W. Frazier, Shengmai (May) An, Eduardo Medina, Marco A. Avila, Luis Alcantar, Jia Gou, Nathan R. Stenberg, Jay Stotsky, Kate Meyer, Jodin Morey, Bruno Poggi, Steven Collazos, and Tuan Pham.

Finally, I am grateful to the University of Minnesota, the Department of Mathematics, the Institute of Mathematics and its Applications, and the kind people who have supported me throughout my journey. Bonny Fleming, Prof. Richard McGehee, Carla Claussen, Katherine Dowd, Robin Dixon, Georgia Kroll, Caitlin Knight, Stephanie Lawson, and Lynn Tran - I would not have been able to navigate the program without their help.

I am infinitely grateful for the support and love of everyone mentioned above. They have made this journey possible, and I am lucky to have them in my life.

This work was partially supported by the NSF award CON-75851 and The National GEM Consortium fellowship.

## **Abstract**

This study aims to understand the biochemical pathways involved in the cytoskeleton of *Dictyostelium discoideum*, particularly the self-organization process of actin structures. While previous models have explored protein dynamics in various contexts, they tend to oversimplify the underlying biochemical mechanisms. This study presents two extended models that offer updated insights into the chemical interactions and feedback mechanisms of *Dictyostelium discoideum*. The first model explores how bistability emerges from the topology of the underlying network, while the second model focuses on the mechanisms of filopodia initiation and the role of membrane curvature in their emergence.

---

## *Contents*

<b>List of Tables</b>	vii
<b>List of Figures</b>	viii
<b>1 Introduction</b>	1
<b>2 Dictyostelium Discoideum: Dicty</b>	5
2.1 Introduction . . . . .	5
2.2 The Migration Mechanisms of <i>Dictyostelium discoideum</i> . . . . .	7
2.2.1 Signaling Mechanisms . . . . .	7
2.3 Polarization of the Inositol Lipids . . . . .	10
2.4 The Actin Cytoskeleton . . . . .	15
2.5 Actin Waves in <i>Dictyostelium discoideum</i> . . . . .	20
<b>3 Investigating Multistationarity in the Phosphoinositide Model</b>	29
3.1 Introduction . . . . .	29
3.2 Mass-Action Kinetics and the Multistationary Theorems . . . . .	30
3.3 Theoretical Model of the Reaction-Diffusion System . . . . .	42
3.3.1 Biochemical Reactions . . . . .	44
3.3.2 Reaction-Diffusion System . . . . .	49

3.3.3 Conservation Laws . . . . .	53
3.3.4 Spatially Uniform Model . . . . .	55
3.4 Results . . . . .	60
3.4.1 Multistationary Analysis of the Base Network . . . . .	60
3.4.2 Feedback Analysis . . . . .	63
3.4.3 Single Steady-State Networks . . . . .	64
3.4.4 Multiple Steady-State Networks . . . . .	68
3.4.5 Parameter Identification in a Particular Case . . . . .	76
3.5 Discussion . . . . .	78
<b>4 Filopodia-like Structures in Dictyostelium</b>	<b>84</b>
4.1 Introduction . . . . .	84
4.2 Curvature Sensing and BAR Proteins . . . . .	87
4.3 Filopodia Initiation in Synthetic Bilipid Layers . . . . .	93
4.4 Mathematical Model . . . . .	97
4.5 Results . . . . .	103
4.5.1 Flat Membrane with a Prescribed Phospoinositide Pattern . . . . .	103
4.5.2 Curvature as a Mechanism to Localize Formin Hotspots . . . . .	108
4.6 Discussion . . . . .	112
<b>Bibliography</b>	<b>115</b>
<b>A Sensitivity Analysis</b>	<b>126</b>
<b>B Equilibrium Continuation</b>	<b>130</b>

---

## *List of Tables*

3.1	Species in the model	44
3.2	Chemical reactions involved in the <i>Dictyostelium discoideum</i> model	49
3.3	Total concentration values.	59
3.4	Rate constants recovered via the Newton polytope.	75
4.1	Lipid localization bias of the BAR superfamily proteins.	90
4.2	Rate constants in the filopodia model	105

---

## *List of Figures*

2.1	The life cycle of <i>Dictyostelium discoideum</i> . . . . .	6
2.2	Activation of G-protein coupled receptors. . . . .	8
2.3	Adaptation mechanisms for signal transduction. . . . .	8
2.4	Structure of the lipid bilayer. . . . .	11
2.5	PIP3 and PIP2 membrane patterns in <i>Dictyostelium discoideum</i> . . . . .	12
2.6	Pathways involved in the actin network. . . . .	14
2.7	The actin cytoskeleton. . . . .	16
2.8	Polymerization mechanisms of formins. . . . .	17
2.9	Domain composition of WAVE1. . . . .	17
2.10	Polymerization mechanisms of WASP. . . . .	18
2.11	Structure of an actin wave. . . . .	20
2.12	Typical evolution of actin waves in <i>Dictyostelium</i> . . . . .	21
2.13	Transitions between PTEN- and PIP3-rich regions. . . . .	22
2.14	Spatial organization of actin waves. . . . .	23
2.15	Coexistence of actin waves and polarization patterns. . . . .	24
2.16	Temporal sequence leading to a PIP3 band in giant cells. . . . .	25
2.17	Conversion of circular waves into band patterns of giant cells. . . . .	26
2.18	Spatial translocation of a propagating band in a giant cell . . . . .	27
2.19	Fluorescence imaging of a PIP3 band. . . . .	28

---

3.1	Small phosphorylation network.	31
3.2	Bifurcation diagram for a simplified phosphorylation network.	42
3.3	Phospholipid models	43
3.4	Ras model.	45
3.5	PI3K model.	46
3.6	Rac1 model.	47
3.7	Phosphoinositide model.	48
3.8	Actin model.	49
3.9	Basic phosphoinositide signaling pathway in <i>Dictyostelium</i> .	58
3.10	Single-mechanism, single-steady state networks	66
3.11	Maximal monostationary networks	68
3.12	Single-mechanism, multiple steady-state networks.	70
3.13	The network $\mathcal{R} \oplus \mathcal{J}_4 \oplus \mathcal{J}_5$	76
3.14	Trajectories of species starting from different initial conditions.	79
3.15	Bifurcation diagram for PIP3 against $m_5$	80
3.16	Biochemical pathways on macrophages.	81
3.17	Global dynamics for a sustained perturbation.	82
3.18	Local dynamics of the actin network.	83
4.1	Actin structures in a typical cell	85
4.2	Different initiation models of filopodia	86
4.3	Curvature sensing via BAR domain proteins.	88
4.4	Physical model of blebbing due to curvature.	89
4.5	Turing model of curvature sensing.	92
4.6	Role of integrins in mechanosensing	93

4.7 Typical structure of a filopodium . . . . .	94
4.8 Cryo images of a filopodium. . . . .	96
4.9 Diagram of the biochemical pathways leading to actin dynamics. . . . .	99
4.10 Geometry for the model. . . . .	100
4.11 Diagram of hypothetical mechanism of filopodia initiation . . . . .	102
4.12 Markov chains for the filopodia model . . . . .	104
4.13 Network density at different formin concentrations . . . . .	106
4.14 Distribution of filament orientations. . . . .	107
4.15 Filopodia simulation on a flat membrane . . . . .	107
4.16 Number of filaments for varying concentrations of formins . . . . .	108
4.17 Flat membrane . . . . .	110
4.18 A one protrusion membrane . . . . .	111
4.19 A membrane with five protrusions . . . . .	112
4.20 Effect of membrane curvature in filopodia initiation . . . . .	113
B.1 Graphical representation of the pseudo-arc-length method. . . . .	132

# Chapter 1

---

## *Introduction*

Cell migration is an essential component of species development. Organisms depend on their capacity to detect external signals such as temperature, light, chemical gradients, substrate stiffness, electric fields, and viscosity, among others, to thrive. Remarkably, single-cell organisms have evolved to integrate these signals, often many at a given time, and physically translocate towards a particular goal. For example, neutrophils respond to proteins when infectious agents are present and migrate accordingly to attack invading microbes; embryotic cells sense spatial cues from neighbor cells and segregate appropriately to give rise to structured tissues and organs. Not surprisingly, cell migration is a multicellular phenomenon as well; *Dictyostelium Discoideum* cells, during periods of starvation, secrete cyclic AMP and aggregate into slugs before germination. In the context of cancer development, tumor masses can grow and extend in the direction of nearby blood vessels to support their growth. Other pathological disorders involving migration mechanisms include osteoporosis, rheumatoid arthritis, multiple sclerosis, mental retardation, and autism [1, 2].

Therefore, it is essential to understand the underlying mechanisms involved in cellular migration to improve medical treatments. Although this area of research is active, and experimentalists collect data in abundance, we still need a comprehensive understanding. This lack of general understanding is due, in part, to the thousands of distinct molecular entities within a single organism and the many possible routes of interaction these molecules can have. Consequently, simplistic models provide skewed or no insight into the precise

---

biological mechanisms; realistic models are highly dimensional, involve many and often unknown parameters, and rely on empirical hypotheses of physical and chemical interactions. In addition to this, *in vivo* studies are expensive and time-consuming, and therefore, *in vitro* and *in silico* studies are often preferred. However, we know that cells are dynamically coupled to their extra-cellular environment, and therefore it becomes challenging to extrapolate the underlying mechanisms from *in vitro* studies. Nevertheless, simplified models can address particular observations, and simplistic modeling remains an active and fruitful area of research. In the context of cell migration, molecular localization patterns, wave-like phenomena, directed- and random-migration patterns, and actin polymerization have been extensively discussed [3, 4, 5, 6, 7, 8, 9].

Given the broad spectrum of organisms and phenomenological observations, it is unrealistic for a model to generalize for all cells. Therefore, modeling focuses on representative cells whose observations generalize well to adjacent relatives (in a molecular sense). For eukaryotic cells, whose movement is primarily driven by protrusions, *Dictyostelium discoideum* has become a common choice for experimental research. We can easily manipulate Dictyostelium cells genetically and physically. At the same time, many of its molecular components are tractable. Additionally, a model that describes migration mechanisms for Dictyostelium generalizes well to other eukaryotic cells such as neutrophils, macrophages, and tumor cells, which are of clear medical relevance [10]. For all these reasons, various physical experiments are conducted with *Dictyostelium discoideum* as a model cell to suggest and validate theoretical models.

This study revolves around understanding the *Dictyostelium discoideum* cytoskeleton, particularly the process by which actin structures emerge after protein-sequestering drugs are introduced. In these experiments, wild-type cells are treated with actin-sequestering drugs. These drugs dissolve the cytoskeleton and inhibit the cell from migrating. Af-

---

ter removing the drug, and before the cytoskeleton recovers, wave-like patterns emerge at the substrate-attached portion of the cell’s membrane. These wave patterns involve many molecules, including signal receptors at the cell’s surface, lipids at the plasma membrane, intracellular polymerases, and actomyosin motors.

Previous models have addressed some observations regarding cytoskeleton dynamics in different contexts. For example, in [3, 11, 6], the authors discuss low-dimensional models that lead to wave phenomena. However, in these studies, simplifications obscure the true nature of the underlying biochemical mechanisms. Indeed, the proposed inhibitors or catalytic molecules are hard to identify in a detailed model. Other models are more true to biology, such as the models in [12, 13], and [14], where the authors discuss the dynamical behavior of the phosphoinositide lipids PI(4,5)P<sub>2</sub> and PI(3,4,5)P<sub>3</sub> at the membrane. In these models, however, the mechanisms involved, particularly those regarding downstream feedback, are fitted to observations, and their existence is debated.

The present document aims to provide two extended models with updated insights into *Dictyostelium discoideum*’s related chemical interactions and feedback mechanisms. In particular, we will address the problem of feedback motifs by investigating their effects on the steady state of our system. Chapter 2 includes an overview of *Dictyostelium discoideum* and its migration mechanisms. Chapter 3 describes actin wave patterns observed in starved, latrunculin-treated cells. The latter part of chapter three introduces our mathematical model, starting with the theory needed for the analysis. Later in chapter three, we develop a spatio-temporal description of the underlying dynamical system. We close this section by presenting our results, including studies on the bistability of the system, sensitivity to parameters, and maximal and minimal networks that preserve stationary state properties. Chapter 4 focuses on the mechanisms of filopodia initiation. We introduce the experiments of Lee *et al.* [15] and develop a simplistic model replicating some of the ob-

---

servations. In the last part of chapter four, we investigate the effect membrane curvature has on filopodia initiation. Appendices are included to justify the methods and are meant to be a reference and summary of the source material.

## Chapter 2

---

### *Dictyostelium Discoideum: Dicty*

#### 2.1 Introduction

*Dictyostelium discoideum*, or Dicty for short, is a eukaryote that belongs to the Amoebozoa phylum, which diverged from the Opisthokonts, the phylum to which the animals belong. Dicty is often referred to as the social amoeba partly for its dependence on aggregation and population dynamics during its life cycle. Wild-type Dicty lives in the soil, reproduces by binary fission, and feeds on bacteria by engulfing and digesting microbes. However, when food sources are scarce or during starvation periods, Dicty secretes cyclic AMP (cAMP) and undergoes an aggregation cycle in which colonies, ranging from as few as 12 cells to as many as 100,000 cells, converge by chemotaxis. This aggregation cycle precedes a collective migration period that culminates in a fruiting body prior to germination (see Figure 2.1) [16].

In the wake of starvation, some *Dictyostelium discoideum* cells differentiate to become pacemakers of the process. Pacemaker cells release periodic pulses of cyclic AMP and set a center for aggregation. The rest of the cells become sensitive to the secreted cAMP, migrate in the direction of the pacemaker and also relay the signal to neighbor cells. At the aggregation center, cells merge and form a cylindrical structure, usually referred to as the *Dictyostelium* slug, alluding to its appearance. The Dicty slug secrets a slime sheath around its body and begins a migration phase. In order to optimize the conditions leading to

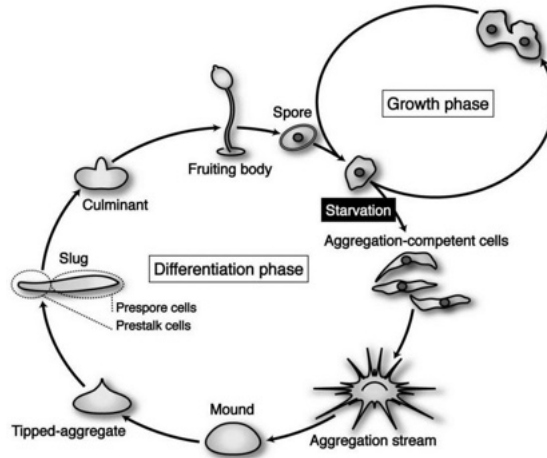


**Figure 2.1:** The life cycle of *Dictyostelium discoideum*. Taken from [17].

germination, Dicty slugs migrate away from ammonia and towards heat, light, and oxygen. Once the slug settles, it transforms into a slender stalk topped by a fruiting body with spores. The fruiting body then bursts, and the spores atop propagate, thus, renewing the cycle.

The complex life cycle of Dicty makes it an appealing organism for its characteristic behavioral patterns. Although our interest herein is in the mechanisms of chemotaxis, Dicty is extensively used as a model for intracellular signaling, polarization, phagocytosis, macropinocytosis, autophagy, quorum sensing, cell-cell interactions, predator-prey dynamics, tissue patterning, cooperativeness, and altruism. Moreover, Dicty cultures are easy to grow and inexpensive to maintain, and many of their biochemical mechanisms, proteins, and signal pathways are well conserved in mammalian cells. Thus, insights found in *Dictyostelium discoideum* have the potential to shed light on human-related diseases [18, 19].

This chapter introduces the biochemistry of *Dictyostelium discoideum* in the context of chemotaxis at the molecular level. First, we present Dicty's migration mechanisms and describe the signal transduction process. Then, in the following subsections, we present the response mechanisms of external stimuli, namely, the cell's membrane and its underlying cytoskeleton, which are the main object of the theory developed in chapters three and four.

## 2.2. The Migration Mechanisms of *Dictyostelium discoideum*

---

Finally, the last subsection introduces actin waves; a membrane-to-cytoskeleton coupled phenomena that arise in this context. Our primary goal is to understand better the underlying dynamics and shed light on not well-understood mechanisms.

## 2.2 The Migration Mechanisms of *Dictyostelium discoideum*

As noted before, Dicty has many proteins and signal pathways associated with eukaryotic development and pathological disorders. From this point onwards, our primary focus is on Dicty's biochemical interactions that facilitate chemotaxis. In this section, we will overview the existing literature. Then, we provide detailed information on the underlying biological molecules and their known mechanisms of action. At the same time, we introduce related theoretical work. We start with signaling mechanisms, namely, those responsible for sensing and transmitting chemical signals. Then, we look at the inositol lipids and the plasma membrane with an overview of front-to-back polarization. Lastly, we review the composition of the cytoskeleton and the distinct structures that emerge in a migrating cell.

### 2.2.1 Signaling Mechanisms

The G-coupled receptors (GPCRs) at the plasma membrane of *Dictyostelium discoideum* are the first layer in chemical signal reception and transduction. We know that in Dicty, folic acid and cyclic AMP (cAMP) are two chemical agents that activate GPCRs. Under normal circumstances, *Dictyostelium discoideum* tracks bacteria via folic acid. However, if cells undergo starvation, individual cells aggregate by following periodic pulses of secreted cAMP.

In the standard picture, GPCR receptors bind to chemoattractants and induce phosphorylation at their C terminals to stimulate G-protein activity. Four receptors have been dis-

## 2.2. The Migration Mechanisms of *Dictyostelium discoideum*

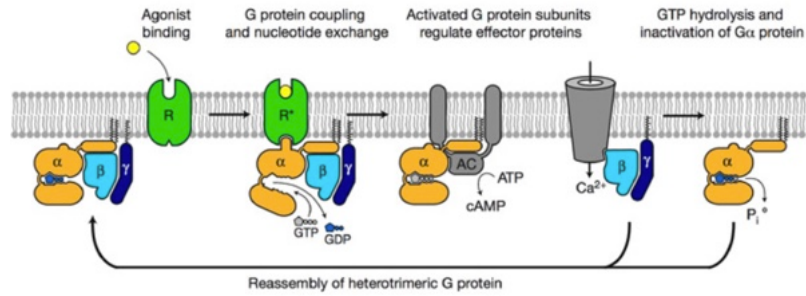


**Figure 2.2:** Activation of G-protein coupled receptors. Taken from [20]

covered in Dicty that are sensitive to cAMP (cAR1-4). Of these, only cAR1 is essential for cAMP signal transduction. Cells lacking cAR1 and cAR3 fail to migrate up the cAMP gradient, whereas cells that lack cAR3 migrate normally. Deletion of cAR2 or cAR4 results in defects only at the later stages of development [21].

Although signal detection is a consequence of GPCR activity, gradient sensing does not appear to occur at this initial step. Instead, active receptors remain uniformly active in cells under chemotactic gradients [21]. Thus, gradient sensing by amplification is an intracellular process. One theory is that, immediately upon signal reception, the transduced signal induces an excitable response. We mean a fast and sharp local activity of downstream molecules. However, excitation only occurs when the signal exceeds a certain threshold.

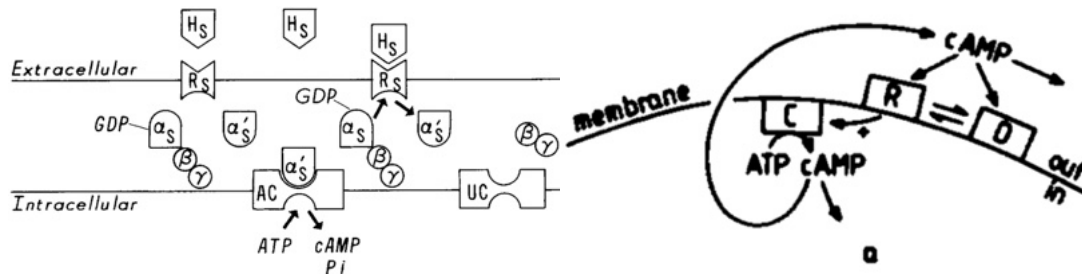


**Figure 2.3:** Adaptation mechanisms for signal transduction.

Downstream G-protein complexes carry the signal from GPCRs. G-proteins are divided

## 2.2. The Migration Mechanisms of *Dictyostelium discoideum*

---

into  $\alpha$ ,  $\beta$ , and  $\gamma$  subunits. We know that Dicty possesses at least 11 different  $G_\alpha$  subunits. However, we know only of one  $G_\beta$  and one  $G_\gamma$ . Upon cAR1-receptor activation, its phosphorylation attracts the complex  $G_{\alpha\beta\gamma}$ . Then, the  $G_{\alpha\beta\gamma}$  complex undergoes a conformational change that dissociates the  $G_\alpha$  and  $G_{\beta\gamma}$  subunits; each subunit activates other signal cascades independently (Figure 2.2). For example, the  $G_\alpha$  subunit regulates adenylate cyclase, producing intracellular cAMP. In contrast, the  $G_{\beta\gamma}$  subunit has a role in regulating actin polymerization [24, 25].

An essential property of signal reception is the capacity to adapt the response. That is, a cell must timely return to a pre-stimulus state even in the continued presence of a signal. This adaptation mechanism allows cells to change direction if needed, for example, while aggregating in the direction of a pulsating signal source. The so-called “*back of the wave*” problem remained a paradigm before the development of adaptation models. Given that chemotaxis occurs in the direction of cAMP gradients, a chemical pulse traveling outwards from the aggregation center would influence cells to move *away* instead of *towards* the center. The qualitative resolution of this paradox appears in [26]. The authors modeled adaptation by allowing GPCR receptors to saturate and desensitize with a heuristic feedback loop introduced to account for unknown downstream mechanisms.

Other studies for adaptation models in *Dictyostelium discoideum* include [27, 23, 16, 22, 28, 29, 30, 31, 32], and [24]. In [27], the authors discuss a model for cAMP secretion based on negative feedback from calcium influx into the cell. Othmer *et al.* argue in favor of an unknown at the time negative feedback loop. The case is that experimental data correlates poorly with models lacking inhibition from effectors downstream of the receptor. Another early example of signal adaptation is the model suggested by Martiel *et al.* [23]. In this article, the authors assume that the adaptation of cAMP receptors is due to conformational changes. After activation, the receptor undergoes a structural change that temporarily

### 2.3. Polarization of the Inositol Lipids

---

inhibits a response (See figure 2.3b). However, the model failed to replicate experimental observations explained by Othmer *et al.*

Following the principle of downstream inhibition, several models have been able to replicate the signal reception step before aggregation in Dicty. For example, in [22], cAMP signals activate two forms of G-protein receptors, one which acts as a response stimulus and another one that inactivates the receptor capacity for stimulating the former G-protein (see Figure 2.3a). This model successfully replicated the wave propagation patterns of *Dictyostelium discoideum* during aggregation, as discussed in [16, 22], and [28].

We remark that the current understanding of signal reception is still incomplete. Much work exists regarding chemical signaling. However, physical input from the extracellular matrix or internal sources has usually been oversimplified or wholly ignored. It is particularly challenging to uncover the biological mechanisms responsible for sensing and integrating these physical signals. Some of these mechanisms, however, are better understood now than they were a decade ago. To name one example relevant to Dicty, we now know that actomyosin cables linked to integrin-mediated adhesions in mammalian cells can induce conformal changes to proteins within the complex. For example, force applied to the adhesion complex protein CAS (or BCAR1) leads to exposure of phosphorylation sites for SCR-family kinases involved in activating Rho GTPases [33]. SadA, sibA, and sidB, have been identified in Dicty as proteins with similar mechanosensing properties; however, little is known about the downstream pathways involved [34] [35].

## 2.3 Polarization of the Inositol Lipids

The membrane of Dicty is a bilipid layer composed mostly of inositol phospholipids (see Figure 2.4). These lipids act as a binding substrate for Rho GTPases, polymerases, and

### 2.3. Polarization of the Inositol Lipids

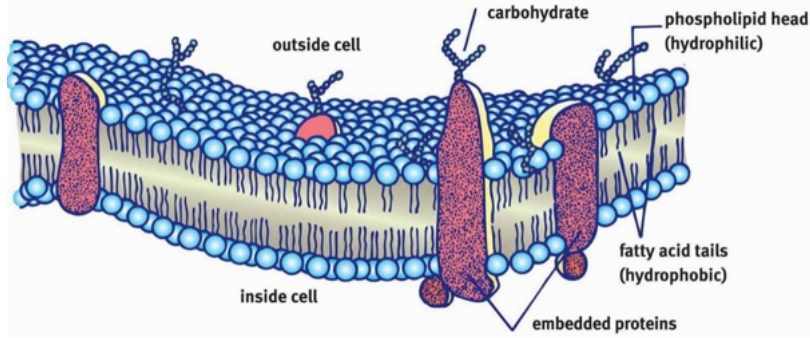


**Figure 2.4:** Structure of the lipid bilayer. Taken from [36].

G proteins. PI(4,5)P<sub>2</sub> is one of the most abundant of the phosphoinositides, second to PI(4)P. PI(4,5)P<sub>2</sub> localizes to the back of a migrating cell and upregulates formin, myosin-II, Ena/VASP, and phosphatase and tensin homolog (PTEN) activity. Conversely, PI(3,4,5)P<sub>3</sub> localizes to the front of the migrating cell and, analogous to PI(4,5)P<sub>2</sub>, is involved in signaling downstream molecules, such as phosphatidylinositol 3-kinase (PI3K) and Rac1, both relevant to dendritic actin polymerization. We focus on the patterns emerging from the interactions of PI(3,4,5)P<sub>3</sub>, PI(4,5)P<sub>2</sub>, PI3K, and PTEN. Although other regulators are known, such as phospholipase C kinase (PLC) (which hydrolyzes PI(4,5)P<sub>2</sub> into diacylglycerol and inositol (1,4,5)-trisphosphate), there is little information regarding their contribution to chemotaxis. We will review known mechanisms and introduce relevant feedback mechanisms hypothesized in the literature.

Class I PI3K further divides into 1A and 1B groups depending on their regulatory subunit binding, p85 and p101, or p87, respectively. We know that Dicty possesses three distinct isoforms of PI3K, namely PI3K1-3. PI3K1 and 2 in Dicty are reportedly similar to class 1A, and PI3K3 is most closely related to class IB PI3Ks [21]. Experimental data suggest that these groups are activated by either tyrosine (Tyr) kinases, in the case of 1A; by G<sub>βγ</sub> subunits, in the case of 1B; or by Ras, both in 1A and 1B isoforms [37] [38]. Addition-

### 2.3. Polarization of the Inositol Lipids

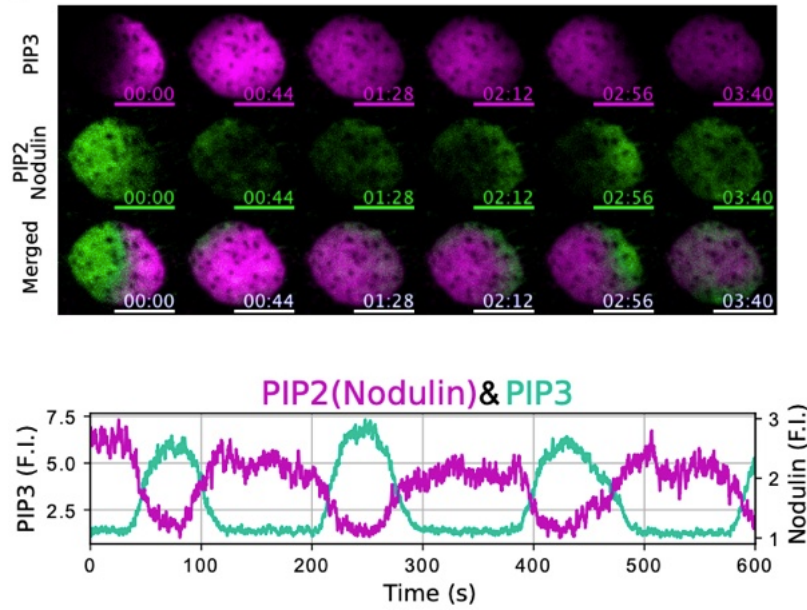


**Figure 2.5:** PIP3 and PIP2 membrane patterns in *Dictyostelium* cells. Taken from [13]

ally, experiments done in human kidney (HEK) cells point out that the sole purpose of the p101 subunit is to recruit PI3K from the cytosol to the membrane via its binding domain [39]. Given that Ras activation follows from  $G_{\beta\gamma}$  activity, PI3K activation may be due initially, and transiently, to  $G_{\beta\gamma}$  and then sustained by Ras. In cells treated with the PI3K inhibitor LY294002, polarity and chemotaxis are defective, suggesting the essential role of PI3K. Although some experiments report contradictory information, this may result from residual PI3K activity or other pathways independent of PI3K [40].

PTEN antagonizes PI3K activity by hydrolyzing PIP3 back to PI(4,5)P2 and is essential for proper cell migration. Cells lacking PTEN have chemotaxis defects and, at later stages, aggregate poorly [41]. In unstimulated cells, PTEN exists bound to the membrane at low concentrations, predominantly at the dorsal region and periphery of the substrate-attached portion of the membrane [42]. The exact mechanisms that govern PTEN localization are unknown. However, we know that PTEN binds with high affinity to PI(4,5)P2 at the back

### 2.3. Polarization of the Inositol Lipids

---

and lateral sides of a migrating cell. Additionally, Nguyen *et al.* [43] provide evidence that the C-terminal of PTEN inhibits its binding domain and blocks its activity. These two observations imply that the activation of PTEN occurs immediately after its binding site is exposed. However, it is unknown how long the active state of PTEN persists or what causes its dissociation from the membrane. At any rate, some studies suggest that PTEN deactivation occurs immediately after membrane dissociation [44]. Although other phosphatases exist in Dicty (PI5-phosphatases, for example), these deletions have no apparent effect in chemotaxis [45].

In migrating *Dictyostelium* cells, the membrane exhibits PI(3,4,5)P3 and PI(4,5)P2-rich domains, exclusive of each other. These patterns correlate with PI3K and PTEN, respectively (see Figure 2.5). We know the feedback from downstream molecules is essential for these patterns to emerge. Consequently, appropriate patterning of PI(4,5,6)P3 and PI(4,5)P2 is necessary for proper chemotaxis. However, the feedback mechanisms in play are still debated and largely obscured. Experimental observations demonstrate that PI(3,4,5)P3 suppresses the membrane association of PTEN while promoting its local dissociation. These observations occur independently of actin polymerization, ruling out the possibility of downstream signaling loops. Additionally, cAMP gradients correlate with reducing membrane-bound PTEN without detectable changes in PI(3,4,5)P3 [46]. In resting *Dictyostelium discoideum* cells, basal activity of Ras and PI3K, coupled with the secretion of cAMP, triggers an increase of PI(4,5)P2 phosphorylation into PI(3,4,5)P3. These PI(3,4,5)P3 “patches” either decay or expand into an expanding wave. Furthermore, experiments in *pten*-null cells showed that cAMP caused a reduction in membrane-bound DdPTEN-G129E without detectable changes in PI(3,4,5)P3. Given that PTEN hydrolyzes PI(4,5)P2 from PI(3,4,5)P3 and additionally has a high binding affinity to PI(4,5)P2, it enables a positive feedback loop for catalytic accumulation [46].

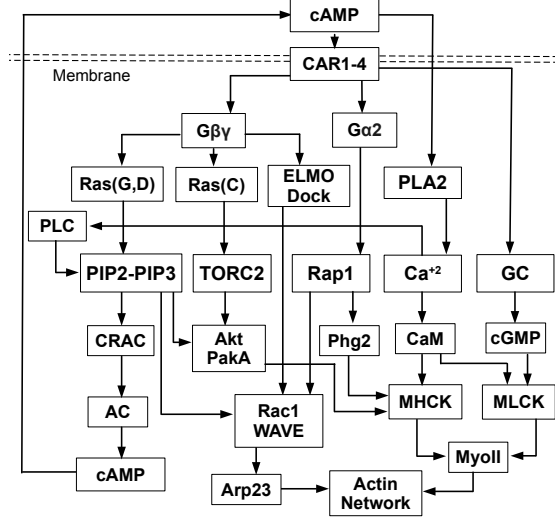


**Figure 2.6:** Pathways involved in the actin network.

Other feedback mechanisms appear in the literature; however, they remain controversial. For example, experiments with  $G_{\beta}^-$  cells suggest a feedback loop to Ras, independent of  $G_{\beta}$  and dependent on actin and PI3K [47, 41]. This claim comes from spontaneous PI(3,4,5)P3 accumulation after cell treatment with actin polymerization inhibitors, correlated to Ras activity in PTEN<sup>-</sup> cells [48]. Actin clusters, initially formed independent of PI(3,4,5)P3, presumably, activate PI3K via feedback loops [49] [48]. A possible explanation for the actin clusters is the basal activity of Rap1 induced by cAMP secretion or  $G_{\beta\gamma}$  activity [15] [50]. With increased PI(3,4,5)P3 expression, further downregulation of the localization of PTEN at the membrane occurs, and PI(3,4,5)P3 accumulates [46]. A different speculated mechanism leading to PI(3,4,5)P3 patches by chemoattractant stimulation uses local and fast activation of Ras via G protein receptors [51]. Fast activation of receptors activates Ras almost immediately and induces PI3K localization; hence, PI(3,4,5)P3 patches emerge.

## 2.4 The Actin Cytoskeleton

Underneath the membrane, actin filaments, microtubules, and stress fibers make up a network that gives rigidity and structural shape to the cell. We refer to this structure as the *cytoskeleton*. In eukaryotes, the cytoskeleton plays a significant role in axonal growth, phagocytosis, cytoplasmic streaming, and organelle transport. In particular, for eukaryotes, the cytoskeleton is essential for migration. Appropriate regulation of the cytoskeleton's properties enables cells to adapt to different environments and external conditions. *Dictyostelium discoideum*, for example, employs distinct modes of migration, such as swimming and crawling. In broad terms, the cytoskeleton regulation depends on the local balance of two types of filament networks. One type is dense and branched, characteristic of the front in a migrating cell. The second type is composed of long and parallel filament bundles characteristic of the trailing edge of the cell and filopodia (see Figure 2.7). As many as five independent signal pathways orchestrate the dynamical change of balance between these two networks (see Figure 2.6). Herein we focus on the effectors of the PIP2 and PIP3 lipids. These include GTPases, formins, nucleating promoting factors, and Arp2/3 (see Figure 2.7).

Small Rho-GTPases act as biomolecular switches for downstream signaling. Their role in signaling is accomplished primarily by providing binding domains. In the Ras superfamily, we group small GTPases into one of the following groups: Ras, Rho, Rab, Ran, and Arf. Rho-GTPases regulate the cytoskeleton composition by activating polymerases. Polymerases are molecules responsible for assembling actin filaments. The nucleating promoting factors (NPF) and formins are relevant to us. In the group of Rho GTPases, we find Rho, Rac, and Cdc42. The latter two, in particular, provide docking sites for nucleating promoting factors via CRIB domains, while the former enhances formin activation. In

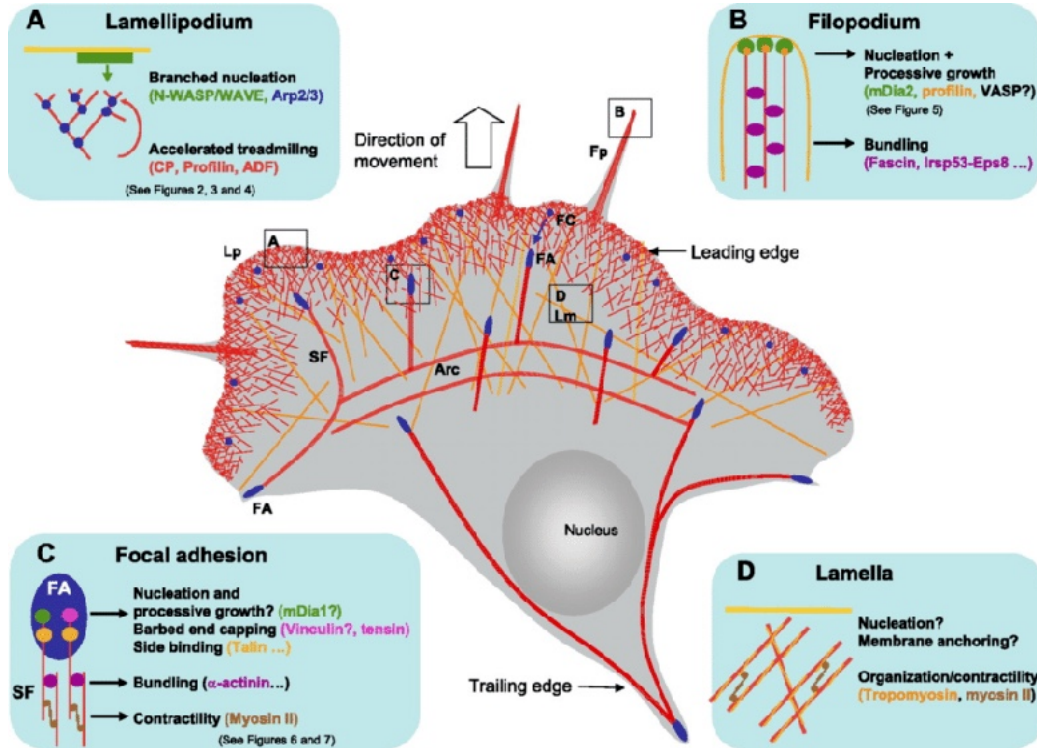
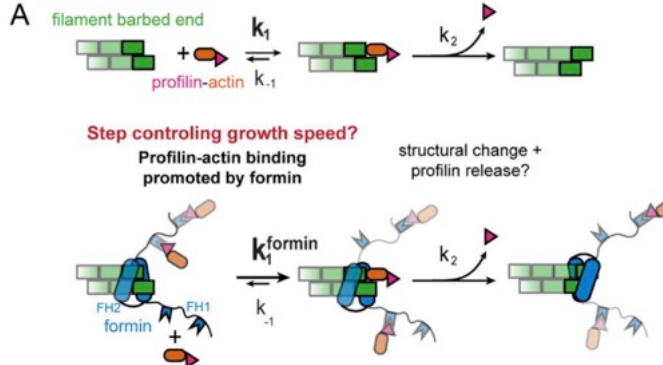


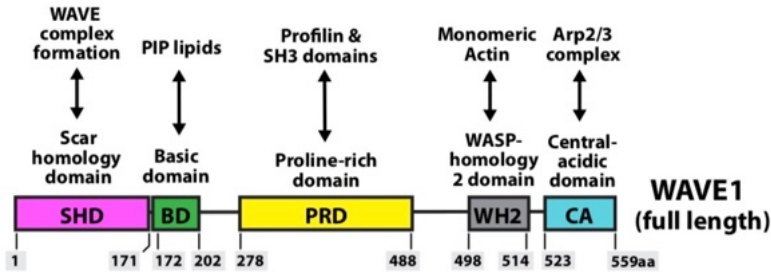
Figure 2.7: The actin cytoskeleton. Taken from [52].

their active form, GTPases are bound to guanine triphosphate (GTP), as opposed to guanine diphosphate (GDP), when inactive. Activation of these molecules depends on the guanine nucleotide exchange factors (GEFs) and GTPase-activating proteins (GAPs). GEFs “turn on” the signal by catalyzing the exchange from GDP-bound to GTP-bound states. Conversely, GAPs “turn off” the signal by GTP hydrolysis.

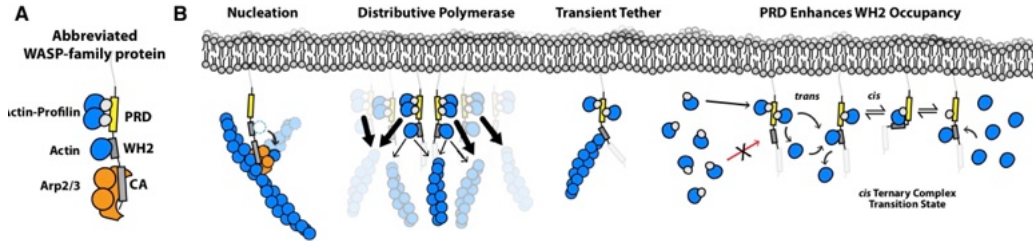
Formins are polymerases that mediate filaments’ anti-capping and elongation activity and may have significant roles in filament bundling via multimeric arms [54]. The most extensive subset of formins in vertebrates is *Diaphanous-related* formins (DRFs). DRFs remain autoinhibited in their rest state. When autoinhibited, the N-terminus blocks the polymerase activity at the C-terminus region. The binding of GTPases to the GTPase binding domain activates DRFs by conformal changes. In mammalian cells, the diaphanous-

**Figure 1**

**Figure 2.8:** Polymerization mechanisms of formins. Taken from [53]

related formin mDia2 is activated through phosphorylation by Rho-associated protein kinase (ROCK) [55]. The mechanism of filament elongation via formins is speculated to occur sequentially, first by removing profilin from the filament's growing end and then delivering monomers (see Figure 2.8). This elongation mechanism uses the formin specialized domains FH1 and FH2. The former has an affinity to profilin, and the latter has a role in membrane binding and filament tethering, providing a mechanism for filament-to-membrane attachment [53][56].


**Figure 2.9:** Domain composition of WAVE1. Taken from [57]

Unlike formins, nucleation-promoting factors promote the assembly of branched actin networks by stimulating Arp2/3-dependent branched polymerization. Common nucleating factors in mammalian cells include SCAR/WAVE, WASP, N-WASP, WHAMM, WASH,



**Figure 2.10:** Polymerization mechanisms of WASP. Taken from [57]

and JMY [57]. Of these, Dicty possesses WASP and Scar/WAVE. Experimental evidence suggests that the GTPase Rac1 activates SCAR/WAVE and WASP [51]. In mammalian cells, PREX1 and PAK (PakA in Dicty) are two Rac GEFs regulated by PI(3,4,5)P3 [51]. NPFs induce the polymerization of filaments via their PWCA motif, which includes a WASP homology (W), a proline-rich (P), and a central/acidic (CA) sequence. Profilin-bound actin monomers bind to the P sequence, while free actin monomers bind to the W domain. The latter central-acidic unit binds and activates the Arp2/3 complex. The proximity of these domains creates a cooperative mechanism that leads to catalytic filament elongation and branching of dense actin networks (Figure 2.9) [57]. It is unknown what the affinities are at each of the PWCA regions. However, some reports investigate the relative kinetic rates in the presence of distinct monomeric actin concentrations [57].

As mentioned before, NPFs have a significant role in Arp2/3 activation. When active, Arp2/3 binds to the barbed end of an existing filament and nucleates a daughter filament. This nucleation leads to branched networks. In migrating Dictyostelium cells, the regulation of Arp2/3 is principally due to SCAR/WAVE [58, 51]. However, when SCAR/WAVE is inhibited, WASP can substitute its function. Although other pathways are known to regulate Arp2/3, the precise biochemical reactions are obscure—for example, the Rap pathway in Dicty. Rap proteins regulate RhoGTPases (Vav2 and Tiamin as GEFs; Arap3 as GAP). Activated Rap1 inhibits myoII (via Phg2) and enhances Arp2/3 activity. A possible local-

ization mechanism for Rap1 could involve the scaffold protein IQGAP, which reportedly leads to its sequestration at the back of the migrating cell [59]. In line with this, other experiments confirmed that activated Rap1 predominantly localizes at the leading edge [15]. The latter two statements provide another mechanism to promote Arp2/3 polymerization at the front. In the classical picture, the ability of formins to use profilin-bound monomers competes with the mechanisms of Arp2/3. However, some reports challenge this view, as Wasp family proteins can deliver monomers to Arp2/3 via their proline-rich domain [57].

As with the membrane's phospholipids, feedback mechanisms from actin to the other upstream regulators discussed in this section remain actively investigated, particularly those involving PI3K and Ras. Sasaki et al. supported the activity of F-actin via pathways other than Ras [49]. In dominant-negative RasG/rasG<sup>-</sup> mutants, chemoattractant exposure induces actin polymerization. However, the pseudopodia are at the right or oblique angles from the stimulation source and with reduced density (small pseudopods). This observation implies that G protein receptors induce actin polymerization via pathways other than Ras. Additionally, the authors showed experimentally that PI3K localization is dependent on F-actin polymerization, as it is apparent that F-actin recruits cytosolic PI3K to the leading edge. PI3K became associated with the cytoskeleton in normal cells after chemoattractant stimulation. However, LatA-treated cells displayed a low level of PI3K1 cytoskeleton association. The conclusion is that PIP3 production is cooperatively regulated by localized Ras activation and F-actin-mediated recruitment of PI3K. An interpretation of the feedback mechanism appears on [60]. “*F-actin network enhances the accumulation of 3'PIs through the ability of class I PI3Ks to bind to F-actin and thus promote a positive feedback loop with PI3K and locally enhancing Ras activity.*” [49, 48], and [61].

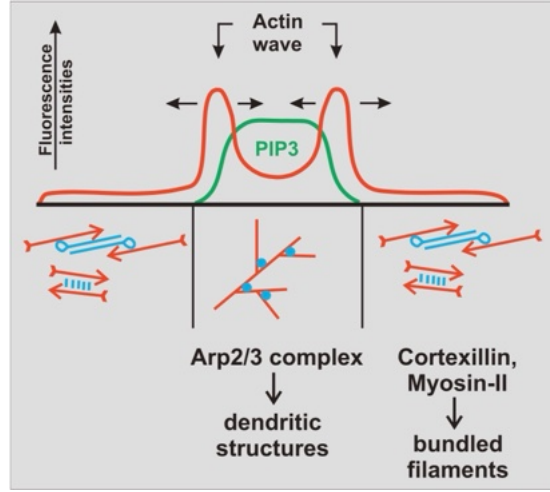


**Figure 2.11:** Structure of an actin wave. Taken from [62].

## 2.5 Actin Waves in *Dictyostelium discoideum*

We now introduce the main object of our investigation, the actin wave patterns observed in Latrunculin-treated *Dictyostelium discoideum* cells. Latrunculin is an actin monomer sequestering drug. Treating the cells with latrunculin deconstructs the cytoskeleton and makes the cells relatively more spherical. After the drug's washout, rebuilding the cytoskeleton leads to wave-like patterns at the substrate-attached surface of the cell (see Figure 2.11). This process involves the following stages [63][62][42] : I) Actin clusters appear at presumably random locations. II) These clusters grow, split, or fuse with one another while traveling across the ventral surface of the membrane. III) At regions with high actin density, a wave of branched actin filaments emerges and propagates, giving rise to patterns characteristic of front-to-back polarization. IV) Actin waves emerge less frequently, and eventually, the cytoskeleton recovers to a wild-type state. The process takes at least 40 minutes (see Figure 2.12).

During the earliest stages, actin clusters spontaneously appear at the substrate-attached portion of the membrane within the first 15 min after latrunculin removal. These clusters are

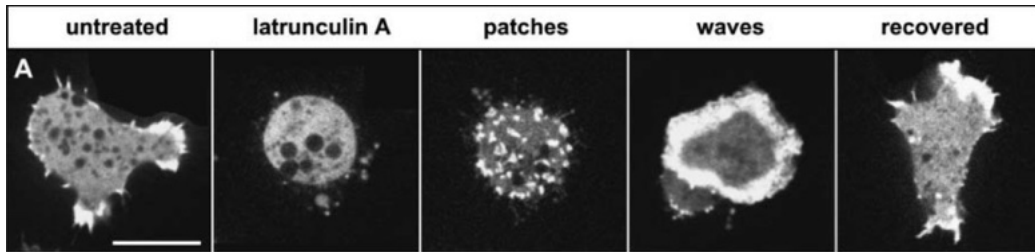


**Figure 2.12:** Typical evolution of actin waves in *Dictyostelium*. Bar, 10  $\mu\text{m}$ . Taken from [63]

mobile and either split, disappear or merge upon collision. Given that less dense structures tend to disappear, it is speculated that a threshold of actin polymerization must be met to sustain them [63]. It is unknown which mechanisms (other than PI(3,4,5)P3 stochastic fluctuations) are responsible for the emergence of clusters. However, evidence supports basal actin polymerization activity independent of PI(3,4,5)P3 [42]. One such possible mechanism is basal clathrin-dependent endocytosis activity, used by cells to explore their environment for bacteria to engulf [62, 64]. Actin clusters appear at sites with high PI(3,4,5)P3 density, usually depleted of PTEN. Within the substrate-attached portion of the membrane, PI(3,4,5)P3 increase correlates with decreasing PTEN fluctuations [42]. Regions depleted of PTEN, referred to as “PTEN holes” in the literature, facilitate sites for accumulation of PI(3,4,5)P3 (see Figure 2.13). More than that, PI(3,4,5)P3 accumulation has excitable properties parallel to the local accumulation of actin. Above a certain threshold, PI(3,4,5)P3 density gets amplified and evolves into a propagating front. Conversely, low PI(3,4,5)P3 densities simply disappear [42]. Similarly, the appearance of PTEN is upregulated by decay in PI(3,4,5)P3 and accumulates in an excitable fashion. The dynamical behavior of PI(3,4,5)P3 and PTEN suggest a cross-inhibitory mechanism; however, such mechanism is unknown [42]. In Figure 2.13, we see how PI(3,4,5)P3 increases in a fast, excitable fashion while its decay is slow and occurs in two steps. The first step comes as a drop to 20-30% of

the maximum expression. The second step is a fast, full drop to depletion.

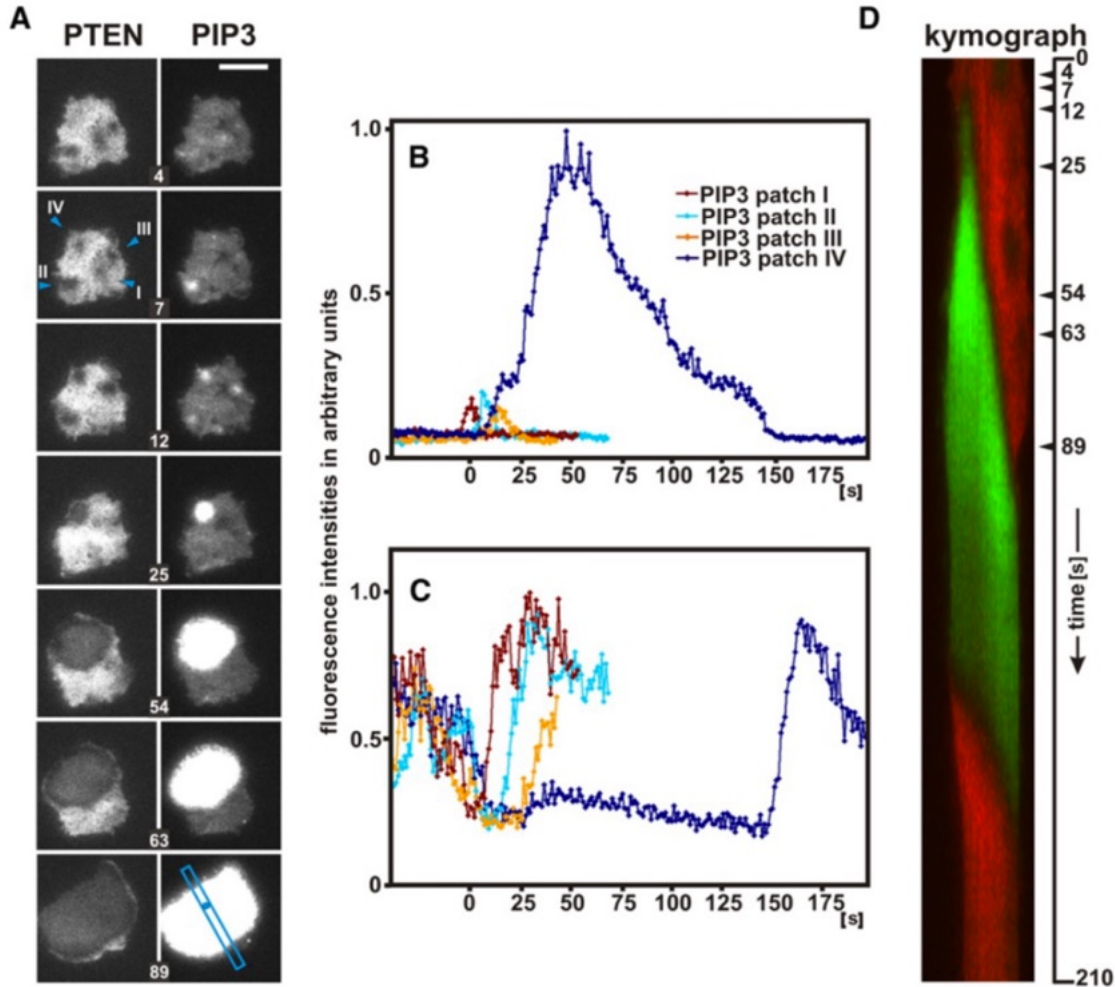


**Figure 2.13:** Transitions between PTEN- and PIP3-rich regions. A) Fluorescence intensities of PTEN (left) and PIP3 (right) are shown in a vertical time-lapse. PIP3 appears inside regions low on PTEN and expand as a wave. B) Time dynamics of PIP3 expression at points I - IV (marked on left panel). C) Dynamics of PTEN expression at points I-IV (marked on left panel). D) Kymograph showing the evolution of PIP3 (green) and PTEN (red) along the blue section in panel A). Bar 10 $\mu$ m Taken from [42]

Following the emergence of an actin cluster, wave-like patterns emerge. The observed actin waves have varying shapes and propagate across the ventral membrane within 20-30 minutes after latrunculin removal. The timing for wave pattern activity is presumed to de-

pend on the cell size, given that actin clusters in smaller cells tend to accumulate faster. The localization of actin clusters is preceded by localized spots of high PIP3 synthesis [65]. Ras activity could explain the synthesis of PIP3 upon stimulation of chemoattractant. However, wave patterns also exist in unstimulated cells, where Ras activity is similar to chemotaxing cells [66]. This observation demonstrates that Ras is activated by pathways other than signal transduction [66]. Furthermore, by performing experiments on migrating cells, the authors of [66] demonstrate that random wave patterns can coexist with front-to-tail polarization simultaneously. The coupling of these two mechanisms for pattern formation is yet to be understood. Figure 2.15 shows an actin wave coexisting with a protruding region.

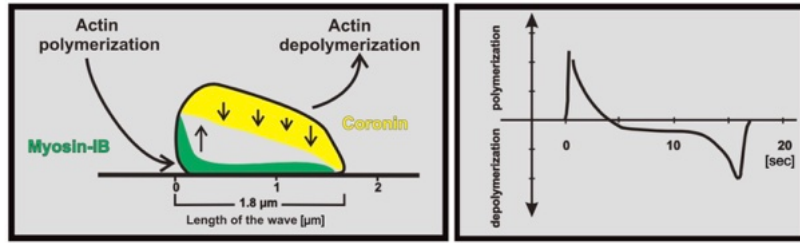


**Figure 2.14:** Spatial organization of actin polymerization factors. Left: vertical slice of a cell. Green and yellow show regions of enriched Myosin and Coronin, respectively. Arrows indicate if actin polymerization is promoted (up) or down-regulated (down). Right: temporal plot of polymerization rates at a fixed point during the pass of an actin wave. Taken from [62].

Propagation of actin waves is sustained by *de novo* actin nucleation [67], with fast polymerization rates at the front and fast depolymerization rates at the back of the wave (see Figure 2.14). The mechanism responsible for propagation could depend on PI(3,4,5)P3 production by PI3K [62]. Concretely, actin waves expand when the interior region is in a PI(3,4,5)P3-rich state and retract when PTEN is present (in the interior) [42]. Recent experiments on giant cells show that the polymerase VASP also has a role in wave propagation. VASP localizes at the front of a propagating wave and precedes Arp2/3 clustering and actin branching [67]. In order to rule out potential feedback from the membrane's curvature, ex-

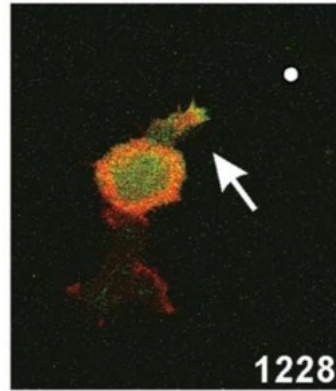


**Figure 2.15:** Coexistence of actin waves and polarization patterns. White dot indicates cAMP source. Arrow points at an emerging Ras cluster. Taken from [66].

periments investigated the relationship between the emergence and propagation of an actin wave and the space between the membrane and the substrate. The observations demonstrate that the substrate-attached portion of the membrane remained constantly flat while an actin wave propagated [63]. More than that, the authors observed that actin waves do not exert forces while traveling across the ventral surface; only upon collision with the boundary were protruding forces evident. It is unclear why the sudden change in force exertion occurs. Actin waves are independent of PTEN, as reported by experiments on PTEN-null cells [64]. In PTEN-null cells, waves still propagate at speeds similar to wild-type cells. However, periodicity is different, and symmetric structures disappear, e.g., horseshoe-shaped waves are absent.

In giant cells, PI(3,4,5)P<sub>3</sub> synthesis becomes unstable at the center. The instability of PI(3,4,5)P<sub>3</sub> is directly related to the radius of an expanding wave. Beyond a critical radius, PI(3,4,5)P<sub>3</sub> enriched regions suddenly transition to a PI(3,4,5)P<sub>3</sub>-depleted state followed by an increase in myosin-II. Figure 2.17 shows a wave that becomes unstable at the center and transitions into a moving band. In some instances, the instability leads to a secondary wave that trails behind, giving rise to doughnut-shaped patterns. This doughnut-shaped wave is

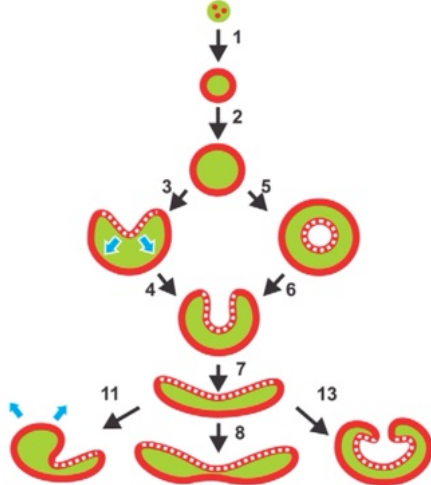


**Figure 2.16:** Emergence of a PIP3 (green) band in giant cells. Taken from [68].

unstable and deforms into a propagating band (Figure 2.16). In an analogous way to normal-sized cells, dense actin networks enclose the PI(3,4,5)P<sub>3</sub> bands; however, the trailing wave is weaker and sometimes missing (Figure 2.18). These trailing waves can emerge spontaneously as well, independent of chemoattractants. Remarkably, moving bands tend to be stable at a width of around 12  $\mu\text{m}$  [68]. The patterns observed in giant cells are consistent with those of normal-sized Dicty. Thus, the expansion and retraction patterns observed in the smaller cell could be explained by the emergence of a moving band. The expanding waves correspond to the leading segments of a band, and the retracting waves to trailing segments (Figure 2.19).

Finally, a propagating wave's culmination occurs at the substrate-attached membrane's perimeter. Remarkably, actin waves can travel over the entire ventral surface, even in giant cells. Moreover, this propagation occurs with an undiminished velocity. Although propagating waves at the substrate-attached portion of the membrane become less frequent with time, the transient state culminates in forming a leading edge, characteristic of wild-type cells [62, 64].

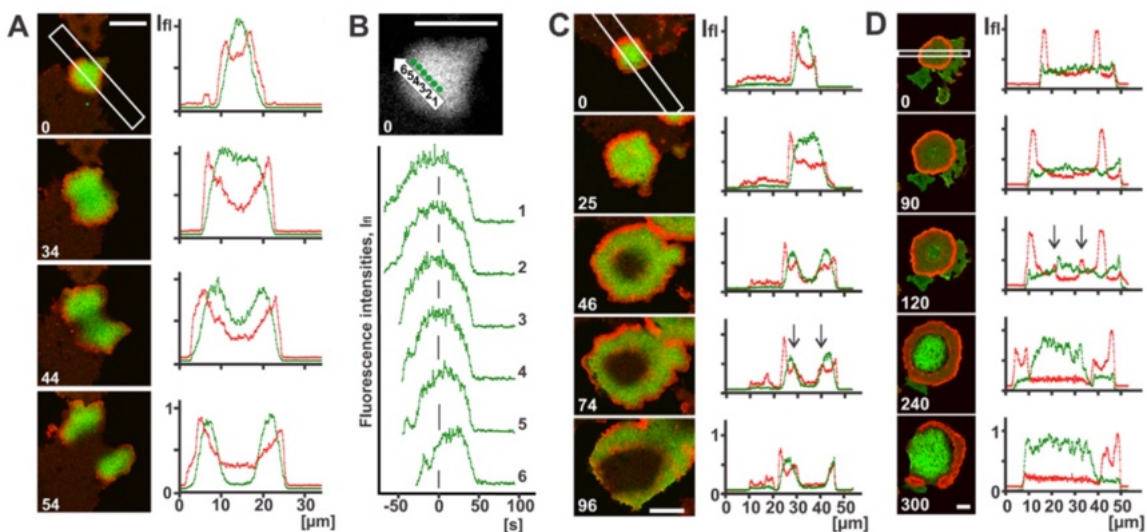


**Figure 2.17:** Circular waves in giant cells. A) A circular wave splits into two propagating waves. PIP3 (green) Actin (red). B) Temporal dynamics of PIP3 at fixed points shown in upper image. C) Circular wave collapses in the center. PIP3 (green), actin (red). D) Actin and myosin patterns in expanding waves. Myosin II (green), actin (red). Bar  $10\mu\text{m}$ . Taken from [68].

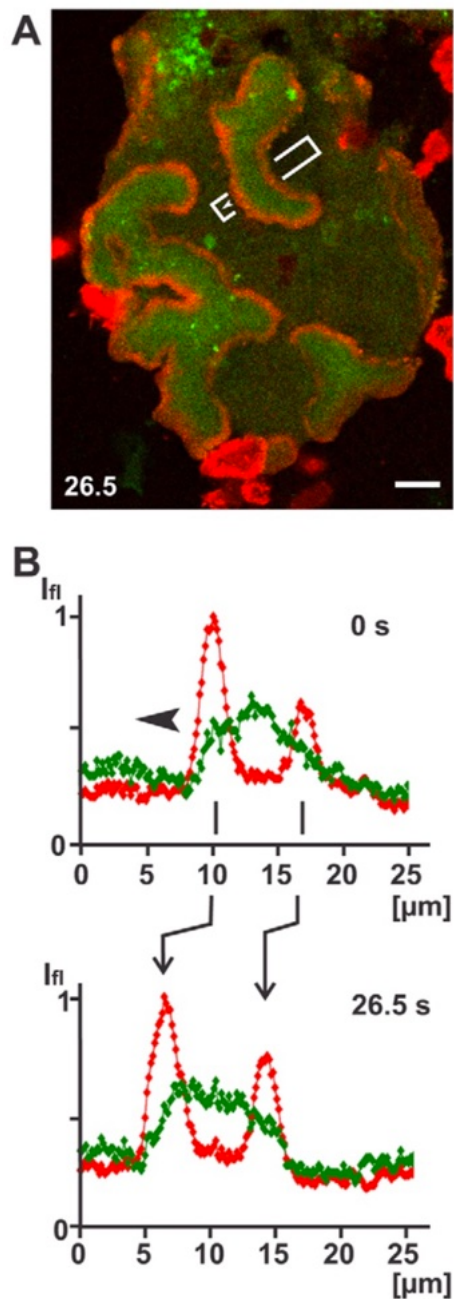


**Figure 2.18:** Spatial dynamics of PIP3 and actin in a propagating band on a giant cell (actin is shown in red, and PIP3 in green). B) Spatial distribution of PIP3 and actin at different times measured along white bar in panel A). Bar 10  $\mu\text{m}$ . Taken from [68].

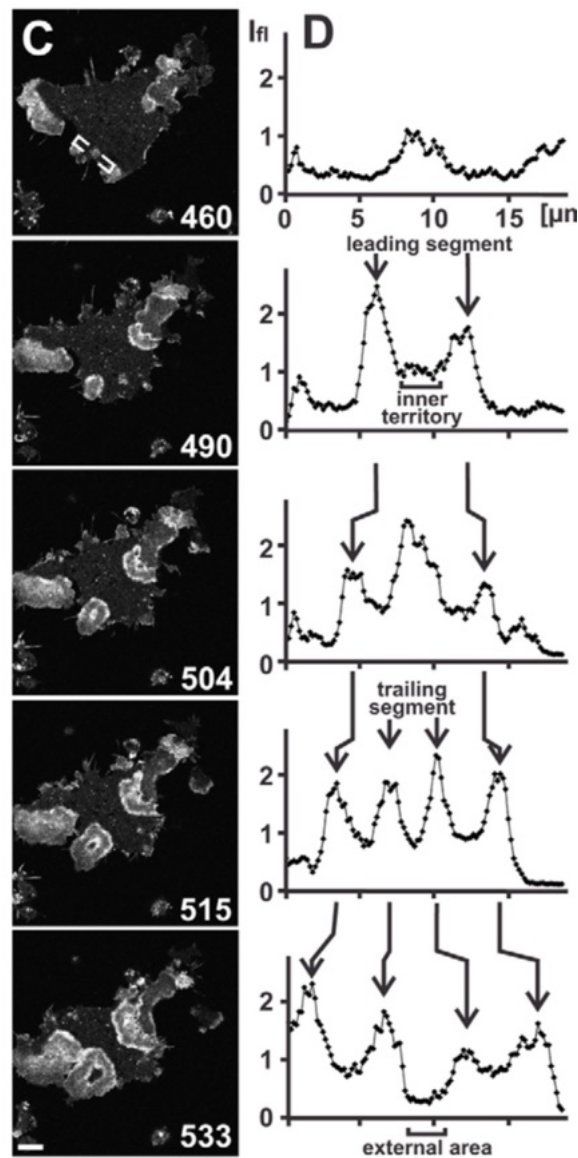


**Figure 2.19:** Fluorescence imaging of a PIP3 band. Taken from [68]. Bar 10 μm .

## Chapter 3

---

### *Investigating Multistationarity in the Phosphoinositide Model*

#### **3.1 Introduction**

A mathematical framework based on a dynamical system that exhibits multiple steady states (or equilibria) is a natural choice for many biological processes. Multiple equilibria may describe the system’s long-term behavior. For example, steady states may point to distinct phenotypes in a given cell model; or dictate biomolecular reactions in response to environmental cues. Therefore, it is essential that, at the outset, the chosen biochemical network contains a representative set of molecular species and that all the critical reactions are included. However, as the complexity of the network increases, so does the uncertainty of its output. That is, the effect perturbations in the model parameters have on the output is difficult to understand. Finding analytical results is not feasible even for networks with a modest number of species and parameters. This problem is particularly complex for systems where parameters might not be available, or underlying biochemical reactions are still debated. In this chapter, our goal is to present a framework that helps us understand the robustness of multistationary properties with respect to our network and our choice of kinetic parameters. As we will see, this method can identify minimal or maximal networks that admit multiple steady-states. Simultaneously, we can explicitly state a multivariate “critical function” that describes the consistent parameter domain whenever kinetic parameters are unknown. The advantage of this method is that we avoid using numerical simulations and parame-

ter sampling, which are usually computationally expensive. Lastly, this technique identifies potential network targets for rescuing or severing the existence of multiple equilibria, which is of clear experimental value in characterizing a system's response. We base our work on the methods introduced by Conradi, Shiu, and Dickenstein [69, 70].

We start by setting the definitions and theory while following a toy problem for exposition. Then, we describe a *Dictyostelium discoideum* model related to the actin wave problem described in the previous section. Next, we describe the global model and simplify the equations to a local ODE system. Finally, we analyze the system and describe the results in detail. We close with a short discussion section pointing out the advantages and shortcomings of our work.

## 3.2 Mass-Action Kinetics and the Multistationary Theorems

We follow the conventions and notation used by the respective authors of [70, 69, 71, 72]. First, we will describe the theory of mass action kinetics. Then, we define the criterion for identifying parameter regions that admit multiple steady states given a biochemical network. We follow the theory with a relevant, albeit simplified, PIP3 phosphorylation model (see Figure 3.1). In our ongoing example, we will show that PTEN upregulation by PIP2 is *necessary* for the system to admit more than one steady state. Similarly, we will show that high decay rates drive the system from a multistationary to a single steady-state regime.

**Definition 3.2.1** (Reaction network). *A reaction network  $G$  consists of a set of species  $S = \{X_1, X_2, \dots, X_s\}$ , and a set of  $m$  reactions of the form*

$$\sum_{i=1}^s \alpha_{j,i} X_i \rightarrow \sum_{i=1}^s \beta_{j,i} X_i. \quad j = 1, 2, \dots, m \quad (3.1)$$

*Where  $\alpha_{i,j}$  and  $\beta_{i,j}$  are non-negative coefficients in  $\mathbf{Z}$  defined by the  $j$ th reaction.*

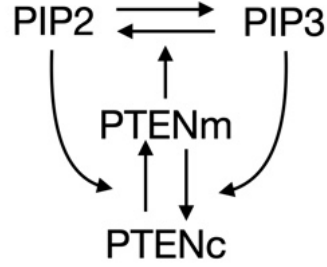


**Figure 3.1:** Reduced phosphorylation network.

**Example 3.2.2** (Reduced phosphorylation network). *We define the reduced phosphorylation model as the system described by the reaction network:*

- 1)  $PIP2 \xrightarrow{1} PIP3,$
- 2)  $PIP3 + PTEN_m \xrightarrow{1} PIP2 + PTEN_m$
- 3)  $2 PIP2 + PTEN_c \xrightarrow{r} 2 PIP2 + PTEN_m$
- 4)  $PTEN_m + PIP3 \xrightarrow{1} PTEN_c + PIP3$
- 5)  $PTEN_c \xrightarrow{\delta} PTEN_m.$

In the example above, PIP2 spontaneously converts to PIP3 (reaction 1). At the same time PIP2 localizes PTEN from the cytosol to the membrane cooperatively (reaction 3). Localized PTEN, in turn, converts PIP3 to PIP2 (reaction 2) and decays proportional to the concentration of PIP3 (reaction 4). As a mathematical convenience we add the spontaneous localization of PTEN at rate  $\delta$  (reaction 5).

Note that the set of species  $S$  is  $\{PIP2, PIP3, PTEN_m, PTEN_c\}$ . For convenience and to simplify upcoming computations, we have chosen to fix most reaction rates to 1. However, the method generalizes to a system with any number of parameters.

**Definition 3.2.3** (Stoichiometric matrix). *Every reaction network  $G$  defines an  $s \times m$  matrix*

$N$  by the component-wise rule

$$N_{i,j} = \beta_{i,j} - \alpha_{i,j}.$$

We define  $N$  as the stoichiometric matrix of the network  $G$ .

**Example 3.2.4.** Our ongoing example (3.2.2) defines the stoichiometric matrix  $N$ :

$$\begin{bmatrix} -1 & 1 & 0 & 0 & 0 \\ 1 & -1 & 0 & 0 & 0 \\ 0 & 0 & 1 & -1 & 1 \\ 0 & 0 & -1 & 1 & -1 \end{bmatrix}$$

In the context of biochemical reactions, each species  $X_i \in S$  introduces a quantifiable property  $x_i \in \mathbf{R}_{\geq 0}$ , such as the average concentration, number of molecules, and fluorescence intensity, for example. We introduce the vector  $\mathbf{x} = [x_1, x_2, \dots, x_s]^T$  to denote the ordered properties of the species set  $S$ . As standard in this context, each network reaction  $G$  takes place at a prescribed rate  $v_j(\mathbf{x})$ . Following Conradi *et al* [69], we assume that the rate function is a continuous ( $\mathcal{C}^0$ ) function and satisfies both *i*) and *ii*) below:

- i)  $v_j(\mathbf{x}) : \mathbf{R}_{\geq 0}^s \rightarrow \mathbf{R}_{\geq 0}$
- ii)  $v_j(\mathbf{x}) = 0$  if and only if  $x_i = 0$  for some  $i$  such that  $\alpha_{j,i} > 0$ .

The above properties mean that  $v_j(\mathbf{x})$  is a non-negative valued function that evaluates to 0 if any reactants are absent. Standard choices for rate functions include Michaelis-Menten, Hill-type, and mass-action kinetics. In this work, we use mass-action kinetics.

**Definition 3.2.5** (Mass-action kinetic rate functions). *For a reaction relation of the form given in (3.1), we define its reaction rate function  $v_j(\mathbf{x})$  as*

$$v_j(\mathbf{x}) = \kappa_j x_1^{\alpha_{j,1}} x_2^{\alpha_{j,2}} \cdots x_s^{\alpha_{j,s}}, \quad j = 1, 2, \dots, m$$

where  $\kappa_j \in \mathbf{R}_{\geq 0}$  is the reaction rate constant.

For notation consideration, we let  $\mathbf{v}(\mathbf{x}) : \mathbf{R}_{\geq 0}^s \rightarrow \mathbf{R}_{\geq 0}^m$  be the vector that evaluates the reaction rate function component-wise, namely:

$$\mathbf{v}(\mathbf{x}) = [v_1(\mathbf{x}), v_2(\mathbf{x}), \dots, v_m(\mathbf{x})]^T.$$

Then, we can define the governing system of ordinary differential equations for  $\mathbf{x}$  as:

$$\frac{d\mathbf{x}}{dt} = N \cdot \mathbf{v}(\mathbf{x}). \quad (3.3)$$

**Example 3.2.6.** We use mass-action kinetics to model our small phosphorylation model (Example 3.2.2). The resulting system of ODEs is:

$$\frac{d\mathbf{x}}{dt} = \begin{bmatrix} -1 & 1 & 0 & 0 & 0 \\ 1 & -1 & 0 & 0 & 0 \\ 0 & 0 & 1 & -1 & 1 \\ 0 & 0 & -1 & 1 & -1 \end{bmatrix} \begin{bmatrix} PIP2 \\ PIP3 \cdot PTEN_m \\ rPIP2^2 \cdot PTEN_c \\ PTEN_m \cdot PIP3 \\ \delta PTEN_c \end{bmatrix}$$

We remark that the assumptions (3.2) imply that the positive orthant  $\mathbf{R}_{\geq 0}^s$  is a forward invariant subspace. That is,  $\mathbf{x}(t) \in \mathbf{R}_{\geq 0}^s$  for all  $t$  whenever  $\mathbf{x}(0) \in \mathbf{R}_{\geq 0}^s$ . In order to simplify the analysis further, we need to find linear combinations in the set  $\mathbf{x}$  that are invariant under the ODE system (3.3). In other words, we want to identify the underlying conserved quantities of the system (3.3). To be precise, we have the following definition.

**Definition 3.2.7** (Conserved linear relations). A linear combination  $\lambda^T \cdot \mathbf{x} = \lambda_1 x_1 + \lambda_2 x_2 + \dots + \lambda_s x_s$ , with  $\lambda_i \neq 0$  for some  $i$  is said to be a conserved linear quantity if

$$\frac{d}{dt} [\lambda^T \mathbf{x}] = 0. \quad (3.4)$$

In other words  $\lambda^T \mathbf{x}$  remains constant for all  $t > 0$ .

In the context of mass-action kinetics described here, we can find such conservation relations by noting that

$$\frac{d}{dt} [\lambda^T \mathbf{x}] = \lambda^T \cdot N \cdot \mathbf{v}(\mathbf{s}) = (N^T \lambda)^T \cdot \mathbf{v}(\mathbf{x}).$$

For non-trivial  $\mathbf{v}(\mathbf{s})$ , we have that the above is zero whenever  $\lambda \in \ker(N^T)$ . Equivalently, since we are working with a finite matrix  $N$ ,  $\lambda$  belongs to the orthogonal complement of the image of  $N$  denoted  $\text{Im}(N)^\perp$ . It follows that  $\dim(\text{Im}(N)^\perp) + \text{rank}(N) = s$ . For more general systems, finding conservation laws is a nontrivial question.

**Definition 3.2.8** (Conservative network). *We say that a network  $G$  is conservative if there exist a strictly positive vector  $w \in \mathbf{R}_{>0}^s$  such that*

$$w \in \text{Im}(N)^\perp,$$

*equivalently,  $w \in \ker(N^T)$ . In other words, there exist a linear conservation relation in which all the species appear with positive coefficients.*

**Definition 3.2.9** (Conservation matrix ). *Let  $d = \dim(\text{Im}(N)^\perp)$ , and let  $\mathbf{w}_1, \mathbf{w}_2, \dots, \mathbf{w}_d$  be a basis for  $\text{Im}(N)^\perp$ , where  $w_i \in \mathbf{R}^s$ . The  $d \times s$  matrix  $W$  whose rows are the basis elements of  $\text{Im}(N)^\perp$  is called the conservation matrix of  $G$ .*

**Example 3.2.10.** *Moving on with our example network, we find that any linear combination of the vectors  $\mathbf{w}_1 = [1 \ 1 \ 0 \ 0]^T$ , and  $\mathbf{w}_2 = [0 \ 0 \ 1 \ 1]^T$  is in  $\text{Im}(N)^\perp$ . Therefore, the conservation matrix of Example 3.2.2 is*

$$W = \begin{bmatrix} 1 & 1 & 0 & 0 \\ 0 & 0 & 1 & 1 \end{bmatrix}$$

*In particular, the conserved quantities are  $\text{PIP2} + \text{PIP3}$  and  $\text{PTEN}_c + \text{PTEN}_m$ . Additionally, note that our network is conservative, as all species appear in at least one conservation*

*law. This result is not surprising, as the network suggests by mere inspection. However, for more complex systems, where the stoichiometric matrix is less structured, inferring conserved quantities from the network is non-trivial.*

The invariant spaces arising from the linear conservation laws give rise to the definition of compatibility classes and dissipative networks. In a few words, a compatibility class is the set of all possible states allowed by the conserved quantities and initial conditions. Dissipative networks refer to those systems where none of the species grows unbounded.

**Definition 3.2.11** (Stoichiometric compatibility class). *Let  $W$  be a  $d \times s$  conservation matrix of a network  $G$ . For any choice of positive constants  $\mathbf{c} \in \mathbf{R}_{>0}^d$ . We define Stoichiometric compatibility class with respect to  $\mathbf{c}$  as the set*

$$\mathcal{S}_\mathbf{c} := \{\mathbf{x} \in \mathbf{R}_{\geq 0}^s \mid W\mathbf{x} = \mathbf{c}\}. \quad (3.5)$$

Hereafter we refer to  $\mathbf{c}$  above as the *conservation constant* vector or, for simplicity *conservation vector*.

**Definition 3.2.12** (Dissipative networks [69]). *A reaction network is dissipative if, for all stoichiometric compatibility classes  $\mathcal{S}_\mathbf{c}$ , there exists a compact set where the trajectories of  $\mathcal{S}_\mathbf{c}$  eventually enter.*

**Lemma 3.2.13.** *All conservative networks are dissipative.*

The proof of lemma 3.2.13 relies on the fact that we can choose the compact set to be the closure of the stoichiometric compatibility class. Since the network is conserved, the before-mentioned closure is bounded. A rigorous proof is given in [73] (Proposition 3).

We note that the sets  $\mathcal{S}_\mathbf{c}$  are forward invariant with respect to the system of differential equations 3.3. It is not a surprise, then, that for an initial condition  $\mathbf{x}(0)$  one can parametrize

a set of  $d$  species in terms of the linear conservation relations that arise from the stoichiometric compatibility class  $\mathcal{S}_c$ , where

$$\mathbf{c} = W\mathbf{x}(0).$$

Thus, we will assume that  $W$  is in reduced echelon form to proceed systematically, and we will refer to  $I = i_1, i_2, \dots, i_d$  as the index set of pivot columns of  $W$ . The intuitive idea of the following definition is to remove redundant equations in the ODE system (3.3). This reparametrization is necessary, as we will inspect the determinant of the system's Jacobian matrix, which otherwise would be trivial.

**Definition 3.2.14** (The conservation-augmented functions). *Let  $G$  be a reaction network with stoichiometric matrix  $N$  and reaction-rate functions  $v(\mathbf{x})$ , such that the corresponding system of evolution equations is of the form*

$$\frac{d\mathbf{x}}{dt} = N \cdot v(\mathbf{x}),$$

*as introduced in equation 3.3. Let  $W$ ,  $\mathbf{c}$ , and  $I$  be the corresponding (row-reduced) conservation matrix, conservation constant vector, and index set of pivot columns of  $W$ , respectively. The conservation-augmented functions  $f_i(\mathbf{x})$  of the network  $G$  is given by*

$$f_i(\mathbf{x}) = \begin{cases} (N \cdot v(\mathbf{x}))_i & \text{if } i \notin I, \\ (W\mathbf{x} - \mathbf{c})_i & \text{if } i \in I \end{cases} \quad (3.6)$$

*for ease of notation we introduce the vector valued function*

$$\mathbf{f}(\mathbf{x}) : \mathbf{R}_{\geq 0}^s \rightarrow \mathbf{R}^s$$

*given by the component-wise evaluation  $\mathbf{f}(\mathbf{x}) = [f_1(\mathbf{x}), f_2(\mathbf{x}), \dots, f_s(\mathbf{x})]^T$ .*

Note that the dynamics of the network are completely characterized by the function  $\mathbf{f}$ . More than that, the set of equilibria of the ODE system 3.3 coincides with the roots of  $\mathbf{f}(\mathbf{x})$ . In other words,  $\mathbf{x}^* \in \mathbf{R}_{\geq 0}^s$  is an equilibrium state of the system whenever  $\mathbf{f}(\mathbf{x}^*) = 0$ .

**Example 3.2.15.** We showed earlier (Example 3.2.10) that the reduced phosphorylation network is conservative. In particular, we could set the conservation relations to be  $\text{PIP}_2 + \text{PIP}_3 = 1$  and  $\text{PTEN}_m + \text{PTEN}_c = 1$ . This choice of constants means that we normalize the system to the total concentration of the individual species' set. With these relations in mind and noting that the pivot indices of the conservation matrix are 1 and 3, we parameterize the equilibria as the roots of the function:

$$f(\mathbf{x}) = \begin{cases} 0 = \text{PIP}_3 + \text{PIP}_2 - 1 \\ 0 = \text{PIP}_2 - \text{PIP}_3 \cdot \text{PTEN}_m \\ 0 = \text{PTEN}_m + \text{PTEN}_c - 1 \\ 0 = -r \cdot \text{PIP}_2^2 \cdot \text{PTEN}_c + \text{PTEN}_m \cdot \text{PIP}_3 - \delta \text{PTEN}_c \end{cases} \quad (3.7)$$

**Definition 3.2.16** (Mono- and multi-stationary networks). Let  $G$  be a reaction network with a conservation-augmented set of functions  $f_i(\mathbf{x})$ . We say that the network  $G$  is multistationary if the equation  $\mathbf{f}(\mathbf{x}) = 0$  admits at least two solutions. Otherwise, we say that  $G$  is monostationary.

Before we state the main theorems of multistationarity, we define positive steady-state reparametrizations. In general, it is possible to use the system  $f(\mathbf{x}) = 0$  to find relations among the species in the set  $S$  (where  $|S| = s$ ). These relations define a subset  $\hat{S}$ , with  $|\hat{S}| = \hat{s} < s$ , such that, at steady state, there exist a map  $\Phi(\hat{\mathbf{x}}) : \mathbf{R}_{>0}^{\hat{s}} \rightarrow \mathbf{R}_{>0}^s$ . As shown in [70], a careful choice of reparametrizations leads to a simplified, more tractable network analysis. We make this precise in the following definition.

**Definition 3.2.17** (Steady-state reparametrizations). *Let  $G$  be a reaction network with  $m$  reactions,  $s$  species, conservation matrix  $W$ , and conservation augmented functions  $f_i(\mathbf{x})$ . We say that  $\Phi(\hat{\mathbf{x}}) : \mathbf{R}_{>0}^{\hat{s}} \rightarrow \mathbf{R}_{>0}^s$  with  $\hat{s} < s$  is a steady-state reparametrization provided*

1. *For the natural projection  $\Pi : \mathbf{R}_{>0}^s \rightarrow \mathbf{R}_{>0}^{\hat{s}}$ , the map  $\Pi \circ \Phi$  is the identity map.*
2. *The image of  $\Phi$  is the set*

$$\{\mathbf{x}^* \in \mathbf{R}_{>0}^s \mid \mathbf{x}^* \text{ is a steady state of the system defined by } G\}$$

**Example 3.2.18.** *Using the steady state equation (3.7) we see that we can reparametrize the steady state of the system with the map  $\Phi(\hat{\mathbf{x}}) : \mathbf{R}_{>0}^2 \rightarrow \mathbf{R}_{>0}^4$  given by:*

$$\begin{bmatrix} PIP2 \\ PTEN_m \end{bmatrix} \mapsto \begin{bmatrix} PIP2 \\ \frac{PIP2}{PTEN_m} \\ PTEN_m \\ \frac{PIP2}{\delta + rPIP2^2} \end{bmatrix} \quad (3.8)$$

*Note that the steady-state is completely characterized by the variables  $PIP2$  and  $PTEN_m$ .*

Now we introduce the main object for identifying multistationary regimes in a network, the critical function  $C(\kappa, \mathbf{x})$ . The expression  $\kappa = [\kappa_1, \kappa_2, \dots, \kappa_m]^T$  is the vector of rate constants coming from the choice of rate functions as introduced in Definition 3.2.5. Explicitly,  $C(\kappa, \mathbf{x}) : \mathbf{R}_{>0}^m \times \mathbf{R}_{>0}^{\hat{s}} \rightarrow \mathbf{R}$  is given by:

$$C(\kappa, \mathbf{x}) = (\det \text{Jac } \mathbf{f}(\mathbf{x}))|_{\mathbf{x}=\Phi(\hat{\mathbf{x}})} \quad (3.9)$$

where  $\Phi(\hat{\mathbf{x}})$  is a steady state reparametrization. Now we are ready to state the main theorems. The result is an application of Brouwer's degree theory, using 0 as a regular value of the dynamical system. We point the reader to the supplementary information on [69] for the proof of the theorems. Here we will restate the formulation given in [70].

**Proposition 3.2.19** (Multistationarity). *Let  $\Phi$  be a steady state reparametrization for a network  $G$  that is conservative and has no boundary steady states in any compatibility class. Let  $N$  be the stoichiometric matrix of  $G$ .*

A. **Multistationarity.**  *$G$  is multistationary if there exist  $(\kappa^*, \hat{\mathbf{x}}^*) \in \mathbf{R}_{>0}^m \times \mathbf{R}_{>0}^{\hat{s}}$  such that*

$$\text{sign}(C(\kappa^*, \hat{\mathbf{x}}^*)) = (-1)^{\text{rank}(N)+1}$$

B. **Monostationarity.**  *$G$  is a monostationary if for all  $(\kappa^*, \hat{\mathbf{x}}^*) \in \mathbf{R}_{>0}^m \times \mathbf{R}_0^{\hat{s}}$*

$$\text{sign}(C(\kappa^*, \hat{\mathbf{x}}^*)) = (-1)^{\text{rank}(N)}$$

**Example 3.2.20.** *In our ongoing example, we have proved that the network is conservative and, therefore, dissipative. It is left to show that the system does not admit boundary equilibria in the respective stoichiometric compatibility class. In our example, this means that a steady state can not have any of the species in the set  $\{0, 1\}$ . Proceeding by contradiction, assume that one of our species at steady state has a value equal to 0 or 1. Using equations (3.7) and the fact that we have two conservation laws, there are only four possible cases.*

**Case 1:**  $PIP3 = 0$  and  $PIP2 = 1$ . *If this is the case then  $0 = PIP2 - PIP3 \cdot PTEN_m$  implies  $0 = 1$ , a contradiction.*

**Case 2:**  $PIP3 = 1$  and  $PIP2 = 0$ . *If otherwise, this is the case, then  $0 = PIP2 - PIP3 \cdot PTEN_m$  implies  $PTEN_m = 0$  and  $PTEN_c = 1$ . Then,  $0 = r \cdot PIP2^2 \cdot PTEN_c + PTEN_m \cdot PIP3 - \delta PTEN_c$  gives  $0 = 1$ , again a contradiction.*

**Case 3:**  $PTEN_m = 0$  and  $PTEN_c = 1$ . *The contradiction to this case follows from the previous one.*

**Case 4:**  $PTEN_m = 1$  and  $PTEN_c = 0$ . If this is true then  $-r \cdot PIP2^2 \cdot PTEN_c + PTEN_m \cdot PIP3 - \delta PTEN_c$  implies  $PIP3 = 0$ . We see from case 1 that this is not possible.

Note that we are only able to do this systematically since the number of species is small. For larger networks however, other approaches are needed, see for example the work in [74].

Now, we will use the steady state reparametrization in Example 3.2.18 and equation (3.9) to compute the critical function. Explicitly:

$$C(r, \delta; PIP2, PTEN_m) = (\delta + rPIP2^2)(1 + PTEN_m) + \frac{\delta PIP2 - rPIP2^3}{\delta PTEN_c + rPIP2^2 PTEN_m}$$

Since the critical function  $C(r, \delta, PIP2, PTEN_m)$  is a rational expression, the sign function only depends on the numerator after aggregating the terms (provided that the denominator contains only positive terms, which is the case here). After algebraic manipulations we get:

$$\text{sign}[C(\cdot)] = \text{sign} [PIP2(\delta - rPIP2^2) + (\delta + rPIP2^2)^2(PTEN_m + PTEN_m^2)] \quad (3.10)$$

**Claim 1: Upregulation of PTEN by PIP2 is necessary to have multiple equilibria.** Indeed, note that from the critical function above we can compute the right side limit of the expression as  $r \rightarrow 0^+$ . We have

$$\lim_{r \rightarrow 0^+} \text{sign}[C(\cdot)] = \delta PIP2 + \delta^2(PTEN_m + PTEN_m^2)$$

*Proof.* By Proposition 3.2.19 (with  $\text{rank}(N)=2$ ), we have that the above expression is always positive for any value of its arguments. Thus, as PTEN upregulation by PIP2 decreases, the system converges to a single steady-state regime regardless of the choice of  $\delta$ . Similarly, we can inspect the limit as  $r \rightarrow \infty$ . Note that, seen as a polynomial in the variable  $r$ , equation (3.10) is of degree 2 with leading coefficient  $PIP2^4(PTEN_m + PTEN_m^2)$ . Thus,

since the leading coefficient is strictly positive the leading term  $r^2$  will dominate, and thus  $\lim_{r \rightarrow \infty} \text{sign}[C(\cdot)] > 0$ . It is left to show, then, that an intermediate value of upregulation  $r$  exists for which the critical function sign is negative. Even in this case, analytical computations become cumbersome, but we can rely on software to solve the system of inequalities. Here, the condition is satisfied whenever

$$\begin{aligned}\delta &< \frac{\text{PIP2}}{8\text{PTEN}_m^2 + 8\text{PTEN}_m} \\ r &> \frac{-2\delta\text{PTEN}_m^2 - 2\delta\text{PTEN}_m + \text{PIP2}}{2\text{PIP2}^2 (\text{PTEN}_m^2 + \text{PTEN}_m)} - \frac{1}{2} \sqrt{\frac{-8\delta\text{PTEN}_m^2 - 8\delta\text{PTEN}_m + \text{PIP2}}{\text{PIP2}^3 \text{PTEN}_m^2 (\text{PTEN}_m + 1)^2}} \\ r &< \frac{1}{2} \sqrt{\frac{-8\delta\text{PTEN}_m^2 - 8\delta\text{PTEN}_m + \text{PIP2}}{\text{PIP2}^3 \text{PTEN}_m^2 (\text{PTEN}_m + 1)^2}} + \frac{-2\delta\text{PTEN}_m^2 - 2\delta\text{PTEN}_m + \text{PIP2}}{2\text{PIP2}^2 (\text{PTEN}_m^2 + \text{PTEN}_m)}\end{aligned}$$

The particular form of the solution is not relevant, only that real solutions exist.

**Claim 2: High decay rates drive the system to a unique steady state regime** *Similar to our first claim, we look at the limit as  $\delta \rightarrow \infty$ .*

*Proof.* It should be clear that, in the limit, the factor of  $\delta^2$  dominates the critical function expression. Thus, eventually the sign of  $C(\cdot)$  is positive regardless of the choice of  $r$ . Proposition 3.2.19 again the system is admits a single steady-state for all of the other parameter choices. To further support our finding we include the bifurcation diagram of the example network for set values  $r = 10.0$  and  $\delta = 0.01$  (Figure 3.2). Note that the results obtained from the multistationarity analysis agree with the plots. Explicitly, note that when  $r \rightarrow 0^+$  the system has a unique steady state, a consequence of *Claim 1*. Similarly, the bifurcation plot for  $\delta$  shows a unique steady state for sufficiently large values of  $\delta$ , as discussed in *Claim 2*.

Just as we proved that negative feedback is necessary for multiple steady states to exist, we can systematically test many mechanisms of a more extensive network and identify

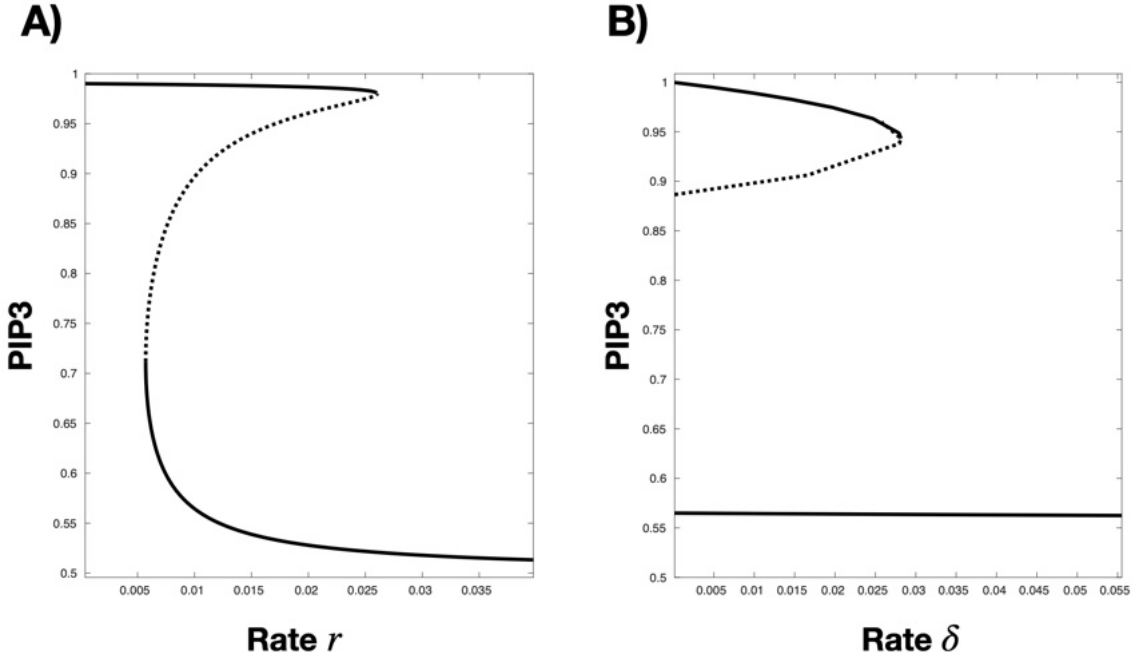


**Figure 3.2:** Bifurcation diagram for a simplified phosphorylation network. A) Steady-state value of PIP3 with respect to the upregulation parameter  $r$ . B) Steady-state value of PIP3 with respect to the decay parameter  $\delta$ . Solid lines and dotted lines indicate stable and unstable equilibria. Initial parameter values are  $r = 10$  and  $\delta = 0.01$ .

which set the dynamical system to a particular regime. Additionally, we can reverse the substitutions in the critical functions to obtain compatible parameters of multistationarity. The following sections explore all of this for a more complex network.

### 3.3 Theoretical Model of the Reaction-Diffusion System

Early models of pattern formation have focused on the role of phosphoinositides, PTEN, and PI3K producing excitable dynamics and wave propagation patterns [12, 75]. However, these early models provide, for the most part, only qualitative predictions. Additionally, the theoretical formulations are somewhat sensitive to network architecture (Figure 3.3). Moreover, some of the mechanisms used rely on abstract constructions rather than “true”

### 3.3. Theoretical Model of the Reaction-Diffusion System

biological mechanisms. The work in [75] uses a modular view of the system, in which excitable subnetworks signal to an oscillatory network which, in turn, feeds back to its input (see [40] for a comprehensive review). However, it is unclear if this latter approach is biologically accurate, as we generally can not measure parameters to guarantee that the temporal scales divide so cleanly. Nevertheless, further work has expanded on the sufficiency of PIP3, PIP2, PTEN, and PI3K coupling for excitable actin patterns at the membrane [13, 14].

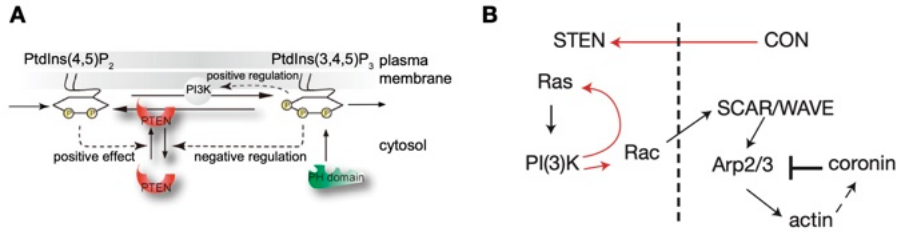


**Figure 3.3:** Phosphoinositide patterning models. A) Taken from [12]. B) Taken from [75]

Therefore, our model uses the Ras-PIP-Actin pathway (see Figure 2.6) as the basis. We will not force any sub-network to have oscillatory or excitable dynamics. We hope that these properties arise from the underlying biochemical architecture. We consider the species set for our reaction-diffusion model: Ras, PI3K, PIP2, PIP3, Rac, Arp23, PTEN, dDia2, and actin. With the multistationary theorems developed in the previous section and bifurcation theory, we aim to understand the patterns of PIP3 that arise from a multistationary system. In particular, we are interested in mechanisms that are essential to the existence of multiple steady states. First, we will develop a general membrane binding reaction model and present the governing reaction-diffusion system. Then, we will uncover the underlying conservation laws. These will be useful when reducing the model to a spatially homogeneous system.

**Table 3.1:** Species in the model

Variables	Description
$\text{Ras}_c, \text{Ras}_m$	Ras Protein
$\text{Rac}_c, \text{Rac}_m$	Rac1 protein
$\text{PI3K}_c, \text{PI3K}_m$	Phosphoinositide 3-kinase
$\text{PTEN}_c, \text{PTEN}_m$	Phosphatase and tensin homolog
PIP2	Phosphatidylinositol (4,5)-bisphosphate
PIP3	Phosphatidylinositol (3,4,5)-trisphosphate
$\text{Arp23}_c, \text{Arp23}_m$	Arp2/3 complex
$\text{dDia2}_c, \text{dDia2}_m$	Diaphanous-related formin
ActinB, ActinM, ActinL	Branched, small, and linear actin filaments
$G_{\beta\gamma}$	G beta-gamma complex

### 3.3.1 Biochemical Reactions

We will base our model on the *basal reactions* from Table 3.2 (cf. Figure 2.6). To distinguish between cytosolic- and membrane-bound species, we use the subscripts  $c$  and  $m$ ; for example, we denote the membrane-bound form of Ras as  $\text{Ras}_m$ . Throughout the rest of the discussion, we will assume that localization immediately precedes activation. We consider this a reasonable assumption as exposure of binding domains usually exposes the mechanisms of protein activity. This assumption will hold for Ras, Rac, PI3K, PTEN, dDia2, and Arp2/3. This modeling approach is typical; see, for example, the signaling model of Cheng *et al.* [24], and the frustrated phagocytosis model of Avila *et al.* [76]. We include a list of variables in Table 3.1. The following few paragraphs will summarize the mechanisms we base our equations on. For clarity, we present the biochemical reactions in a “sectioned” way; however, we do not imply that these sections are disconnected. On the contrary, our model is highly interconnected by feedback pathways (see Figure 2.6). Our work aims to shed light on the necessary and sufficient feedback mechanisms that give rise to multistationary systems, which are the basis of excitable and wave propagation dynamics.

### The Ras model

Our model neglects the signaling upstream of Ras and presumes that the initial signal factor is proportional to the concentration of  $G_{\beta\gamma}$ . As with Rho GTPases, active Ras is bound to guanine triphosphatase (GTP), and inactive Ras is bound to guanosine diphosphate (GDP). Both activation and deactivation of Ras can be spontaneous [66]. The exchange of GTP to GDP occurs via guanine exchange factors (GEFs), while the reverse process is due to GTPase-accelerating proteins (GAPs). In order to maintain the model simple enough for the analysis, we leave out the dynamics of GEFs and GAPs. Feedback to Ras from downstream effectors is experimentally supported by the work of Sasaki *et al.* and Scavello *et al.* [48, 77]. Two hypothesized mechanisms are possible. The first, from PIP3, occurs via the PIP3-Akt pathway. The second comes from experimental results, where elevated Ras activity follows branched actin polymerization after latrunculin washout in cAMP absence. Therefore, we model the rate of the former as proportional to PIP3 and the latter as proportional to ActinB (Figure 3.4).

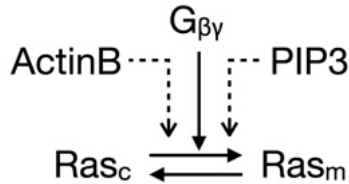


**Figure 3.4:** Ras model.

### The PI3K model

In our model, active Ras positively regulates the activity of PI3K. However, PI3K can also be localized to the membrane by  $G_{\beta\gamma}$  but with lower affinity [78]; thus, we ignore this mechanism. Once PI3K is bound to the membrane, activation depends on the exposure of its phosphorylation unit near its binding domain. Decay of PI3K from the membrane is not

### 3.3. Theoretical Model of the Reaction-Diffusion System

---

well understood, and reportedly it may occur spontaneously [78]. Recent work suggests that feedback from PI(3,4)P<sub>2</sub> and PI(3,4,5)P<sub>3</sub> plays a significant role in its decay via the PLC and AKT pathways, respectively [79]. One of the earliest (and most cited) experimental results on PI3K localization via downstream is due by the Sasaki group [49, 48]. Feedback to PI3K appears to depend on actin polymerization, given that active PI3K localizes to the leading edge after branching actin polymerization. PI3K became associated with the cytoskeleton in normal cells after chemoattractant stimulation. However, in LatA-treated cells, a significantly lower PI3K association arises. The conclusion is that Ras and actin-mediated recruitment of PI3K cooperatively regulate PIP<sub>3</sub> production. An interpretation of the feedback mechanism appears on [37] “*F-actin network enhances the accumulation of 3'PIs through the ability of class I PI3Ks to bind to F-actin and thus promote a positive feedback loop with PI3K and locally enhancing Ras activity...*”. Altogether we model PI3K localization as proportional to active Ras and branched actin and decay as proportional to PIP<sub>2</sub> and PIP<sub>3</sub> (see Figure 3.5).

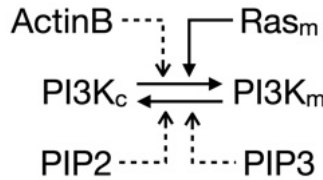


**Figure 3.5:** PI3K model.

### Rac1 model

Given that the mechanisms of Rac1 activation are similar to those of Ras, we analogously model its activity. The primary difference is that Rac1 activation follows interaction with its GEF, which localizes on PI(3,4,5)P<sub>3</sub>-rich membranes. Once active, Rac1 interacts with nucleating promoting factors (NPFs) such as WASP or SCAR/WAVE. These NPFs, in turn,

### 3.3. Theoretical Model of the Reaction-Diffusion System

---

promote the localization of Arp2/3. In our model, we will ignore the dynamics of NPFs in order to keep the system somewhat restricted. Other pathways that converge in Rac1 localization could be mediated by branched actin. The protein GFLB, a Rap GEF, is reportedly localized in branched actin networks in cells undergoing macropinocytosis, phagocytosis, and cytokinesis [80]. Active Rap, in turn, acts as a Rac1 GEF and activates Rac1. Decay of Rac1 by PIP2 occurs by localization of the scaffolding protein IQGAP. IQGAP localizes to PIP2 and, in turn, sequesters active Rac1 [59]. Therefore, we assume that activation of Rac1 is proportional to PI(3,4,5)P3 and branched actin, whereas decay of Rac1 is either spontaneous or proportional to PIP2 (see Figure 3.6).

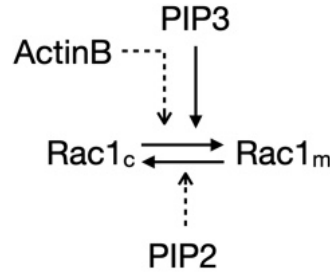


**Figure 3.6:** Rac1 model.

### The Phosphoinositide Model

Here, we restrict the phosphoinositide component to PI(4,5)P2 and PI(3,4,5)P3; however, it is worth noting that the influx of PI(4,5)P2 molecules via phosphorylation of PI(4)P is possible. Analogously, PIP3 is dephosphorylated to lipids other than PI(4,5)P2, such as PI(3,4)P2. Given that PI(4,5)P2 exists at the membrane in a concentration much higher than PI(3,4,5)P3, we will assume a constant decay of PI(3,4,5)P3 proportional to its concentration. Additionally, we model the phosphorylation of PI(4,5)P2 to PIP3 by the action of active PI3K at the membrane. Here, we ignore intermediate complexes. Analogously,

### 3.3. Theoretical Model of the Reaction-Diffusion System

---

we describe the dephosphorylation of PI(3,4,5)P<sub>3</sub> back to PI(4,5)P<sub>2</sub> by the action of PTEN. Mechanistic descriptions of PTEN activation and binding remain largely unclear. In our model, we base our assumptions on the observations by [46]. We assume that PTEN binding to the membrane is exclusive to sites enriched with PI(4,5)P<sub>2</sub>. The decay of PTEN is modeled as either spontaneous or proportional to PIP<sub>3</sub> [46] (see Figure 3.7).

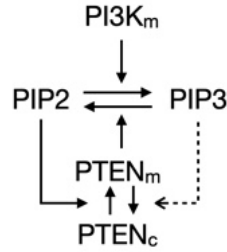


**Figure 3.7:** Phosphoinositide model.

## The Actin model

For computational considerations, we need to simplify actin modeling and focus only on those states of actin filaments we are interested in. We consider three forms of actin: 1) long bundled filaments, typically observed at the back of a migrating cell (ActinL); 2) branched network filaments formed primarily by Arp2/3, which are typical of lamellipodium on the front of a cell (ActinB); and 3) smaller actin filaments and monomers (ActinM) that act as a substrate for either branching or linear networks. Branched actin networks are upregulated by Arp2/3, whereas linear networks depend on formins, such as dDia2 in Dicty. Localization of the dDia homolog mDia depends on PIP<sub>2</sub> [59]. Since formins sequester monomers due to having multiple actin domains, we include an inhibition term in the kinetic rate of Arp2/3 dependent polymerization (see 3.2). Lastly, we ignore the effect of myosin II, as evidence suggests that actin-wave patterns are independent of them [68]. Experiments on myoII null mutant cells further support this last assumption [68]. Thus, we model the

### 3.3. Theoretical Model of the Reaction-Diffusion System

positive regulation of ActinL proportional to dDia, and the positive regulation of ActinB proportional to Arp2/3 and inhibited by dDia2. The conversion of branched or linear actin to ActinM is assumed to occur spontaneously (see Figure 3.8).

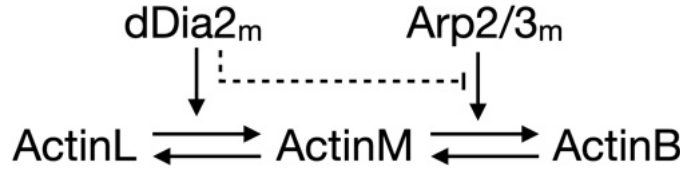


**Figure 3.8:** Actin model.

Basal Reactions	Feedback Mechanisms
$\mathcal{R}_1 := \text{Ras}_c \xrightarrow{k_1 G_{\beta\gamma}} \text{Ras}_m$	<b>Feedback from Branched Actin</b>
$\mathcal{R}_2 := \text{PI3K}_c + \text{Ras}_m \xrightarrow{k_2} \text{PI3K}_m + \text{Ras}_m$	$\mathcal{J}_1 := \text{ActinB}_m + \text{Ras}_c \xrightarrow{m_1} \text{ActinB}_m + \text{Ras}_m$
$\mathcal{R}_3 := \text{PIP2} + \text{PI3K}_m \xrightarrow{k_3} \text{PIP3} + \text{PI3K}_m$	$\mathcal{J}_2 := \text{ActinB}_m + \text{PI3K}_c \xrightarrow{m_2} \text{ActinB}_m + \text{PI3K}_m$
$\mathcal{R}_4 := \text{PIP3} + \text{Rac}_c \xrightarrow{k_4} \text{PIP3} + \text{Rac}_m$	$\mathcal{J}^3 := \text{ActinB}_m + \text{Rac}_c \xrightarrow{m_3} \text{ActinB}_m + \text{Rac}_m$
$\mathcal{R}_5 := \text{Rac}_m + \text{Arp23}_c \xrightarrow{k_5} \text{Rac}_m + \text{Arp23}_m$	
$\mathcal{R}_6 := \text{PIP2} + \text{PTEN}_c \xrightarrow{k_6} \text{PIP2} + \text{PTEN}_m$	
$\mathcal{R}_7 := \text{PTEN}_m + \text{PIP3} \xrightarrow{k_7} \text{PTEN}_m + \text{PIP2}$	<b>Feedback from PIP3</b>
$\mathcal{R}_8 := \text{PIP2} + \text{dDia2}_c \xrightarrow{k_8} \text{PIP2} + \text{dDia2}_m$	$\mathcal{J}_4 := \text{PIP3} + \text{Ras}_c \xrightarrow{m_4} \text{PIP3} + \text{Ras}_m$
$\mathcal{R}_9 := \text{Arp23}_m + \text{ActinM} \xrightarrow{\frac{k_9}{1+\alpha \cdot \text{dDia2}_m}} \text{ActinB} + \text{Arp23}_m$	$\mathcal{J}_5 := \text{PIP3} + \text{PTEN}_m \xrightarrow{m_5} \text{PIP3} + \text{PTEN}_c$
$\mathcal{R}_{10} := \text{dDia2}_m + \text{ActinM} \xrightarrow{k_{10}} \text{ActinL} + \text{dDia2}_m$	$\mathcal{J}_6 := \text{PIP3} + \text{PI3K}_m \xrightarrow{m_6} \text{PIP3} + \text{PI3K}_c$
$\mathcal{R}_{11} := \text{Ras}_m \xrightarrow{k_{11}} \text{Ras}_c$	
$\mathcal{R}_{12} := \text{PI3K}_m \xrightarrow{k_{12}} \text{PI3K}_c$	
$\mathcal{R}_{13} := \text{Rac}_m \xrightarrow{k_{13}} \text{Rac}_c$	<b>Feedback from PIP2</b>
$\mathcal{R}_{14} := \text{Arp23}_m \xrightarrow{k_{14}} \text{Arp23}_c$	$\mathcal{J}_7 := \text{PIP2} + \text{PI3K}_m \xrightarrow{m_7} \text{PIP2} + \text{PI3K}_c$
$\mathcal{R}_{15} := \text{PTEN}_m \xrightarrow{k_{15}} \text{PTEN}_c$	$\mathcal{J}_8 := \text{PIP2} + \text{Rac}_m \xrightarrow{m_8} \text{PIP2} + \text{Rac}_c$
$\mathcal{R}_{16} := \text{dDia2}_m \xrightarrow{k_{16}} \text{dDia2}_c$	
$\mathcal{R}_{17} := \text{PIP3} \xrightarrow{k_{17}} \text{PIP2}$	
$\mathcal{R}_{18} := \text{ActinL} \xrightarrow{k_{18}} \text{ActinM}$	
$\mathcal{R}_{19} := \text{ActinB} \xrightarrow{k_{19}} \text{ActinM}$	

**Table 3.2:** Chemical reactions involved in the *Dictyostelium discoideum* model

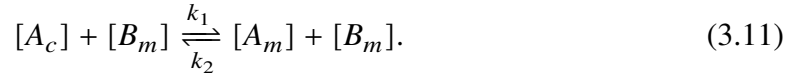
#### 3.3.2 Reaction-Diffusion System

For simplicity and computational considerations, we make the following assumptions. Firstly, we assume that a Dicty cell is perfectly spherical. For species bound to the membrane, we

### 3.3. Theoretical Model of the Reaction-Diffusion System

---

use units of *number of molecules per area*,  $\#/ \mu\text{m}^2$ , and for species in the cytosol, we use density in units of *number of molecules per volume*,  $\#/ \mu\text{m}^3$ . Secondly, our model assumes that membrane binding interactions occur at a thin layer of thickness  $\ell$  between the membrane and cytosol. Thirdly, we assume that binding from the cytosol form of the species  $A_c$  is due to a protein at the membrane,  $B_m$ , which is often the case. This assumption allows us to ignore reactions in the cytosol. Lastly, we assume that diffusion is isotropic and define  $D_s$  as the diffusion constant for the species “s”. We let  $\Omega$  denote the cytosol and  $\partial\Omega$  the membrane domain. Thus, we have the system:



In order to precisely define the binding and unbinding rates ( $k_1$  and  $k_2$ ), we will assume that the species  $A_c$  can interact with  $B_m$  only if it is within distance  $\ell$ . Then, the reaction-diffusion system satisfies

$$\begin{aligned} \frac{\partial}{\partial t}[A_m](y, t) &= D_m \Delta[A_m](y, t) - k_2[A_m](y, t) + k_1[B_m](y, t) \int_{|y-x|<\ell} [A_c](x, t) dx \\ \frac{\partial}{\partial t}[A_c](x, t) &= D_c \Delta[A_c](x, t) \\ D_c \frac{\partial}{\partial n}[A_c](y, t) &= k_2[A_m](y, t) - k_1[B_m](y, t) \int_{|y-x|<\ell} [A_c](x, t) dx. \end{aligned}$$

Where  $\partial/\partial n$  is the outward normal derivative of  $\partial\Omega$ ,  $x$  is a point in  $\Omega$ , and  $y$  is a point at  $\partial\Omega$ . We now assume that  $\ell$  is small enough so that the concentration of nearby cytosolic species within is constant. Thus,

$$k_1[B_m](y, t) \int_{|y-x|<\ell} [A_c](x, t) dx = k_1[B_m](y, t) \cdot [A_c](y, t) \int_{|y-x|<\ell} dx.$$

Note that the latter is equivalent to the volume of a hemisphere of radius  $\ell$  (equal to  $\frac{2}{3}\pi\ell^3$ ).

We scale  $k_1$  as  $k_1 \frac{2}{3}\pi\ell^2$  so that our reaction-diffusion is of the form

$$\begin{aligned}
 \frac{\partial}{\partial t}[A_m](y, t) &= D_m \Delta[A_m](y, t) - k_2[A_m](y, t) + k_1 \ell[B_m](y, t)[A_c](y, t) \\
 \frac{\partial}{\partial t}[A_c](x, t) &= D_c \Delta[A_c](x, t) \\
 D_c \frac{\partial}{\partial n}[A_c](y, t) &= k_2[A_m](y, t) - k_1 \ell[B_m](y, t)[A_c](y, t)
 \end{aligned} \tag{3.12}$$

for all  $x \in \Omega$ , and  $y \in \partial\Omega$ .

We can write the complete reaction-diffusion system using equations (3.12). Since we omitted the cytosol reactions, all the other relevant biochemical interactions will occur at the membrane by design. These membrane reactions appear as mass action kinetic terms on the right-hand side of the respective species. Altogether our system is governed by the following system:

$$\frac{\partial}{\partial t}[\text{Ras}_c] = D_{\text{Ras}_c} \Delta[\text{Ras}_c] \tag{3.13}$$

$$\frac{\partial}{\partial t}[\text{Ras}_m] = D_{\text{Ras}_m} \Delta[\text{Ras}_m] + k_1 \ell[\text{G}_{\beta\gamma}][\text{Ras}_c] - k_{11}[\text{Ras}_m] \tag{3.14}$$

$$D_{\text{Ras}_c} \frac{\partial}{\partial n}[\text{Ras}_c] = -k_1 \ell[\text{G}_{\beta\gamma}][\text{Ras}_c] + k_{11}[\text{Ras}_m] \tag{3.15}$$

$$\frac{\partial}{\partial t}[\text{PI3K}_c] = D_{\text{PI3K}_c} \Delta[\text{PI3K}_c] \tag{3.16}$$

$$\frac{\partial}{\partial t}[\text{PI3K}_m] = D_{\text{PI3K}_m} \Delta[\text{PI3K}_m] + k_2 \ell[\text{Ras}_m][\text{PI3K}_c] - k_{12}[\text{PI3K}_m] \tag{3.17}$$

$$D_{\text{PI3K}_c} \frac{\partial}{\partial n}[\text{PI3K}_c] = -k_2 \ell[\text{Ras}_m][\text{PI3K}_c] + k_{12}[\text{PI3K}_m] \tag{3.18}$$

$$\frac{\partial}{\partial t}[\text{PIP2}] = D_{\text{PIP2}} \Delta[\text{PIP2}] - k_3[\text{PIP2}][\text{PI3K}_m] \tag{3.19}$$

$$+ k_7[\text{PIP3}][\text{PTEN}_m] + k_{17}[\text{PIP3}]$$

$$\frac{\partial}{\partial t}[\text{PIP3}] = D_{\text{PIP3}} \Delta[\text{PIP3}] - k_7[\text{PIP3}][\text{PTEN}_m]$$

### 3.3. Theoretical Model of the Reaction-Diffusion System

---

$$+ k_3[\text{PIP2}][\text{PI3K}_m] - k_{17}[\text{PIP3}] \quad (3.20)$$

$$\frac{\partial}{\partial t}[\text{Rac}_c] = D_{\text{Rac}_c} \Delta [\text{Rac}_c] \quad (3.21)$$

$$\frac{\partial}{\partial t}[\text{Rac}_m] = D_{\text{Rac}_m} \Delta [\text{Rac}_m] + k_4 \ell [\text{PIP3}][\text{Rac}_c] - k_{13}[\text{Rac}_m] \quad (3.22)$$

$$D_{\text{Rac}_c} \frac{\partial}{\partial n}[\text{Rac}_c] = -k_4 \ell [\text{PIP3}][\text{Rac}_c] + k_{13}[\text{Rac}_m] \quad (3.23)$$

$$\frac{\partial}{\partial t}[\text{Arp23}_c] = D_{\text{Arp23}_c} \Delta [\text{Arp23}_c] \quad (3.24)$$

$$\begin{aligned} \frac{\partial}{\partial t}[\text{Arp23}_m] &= D_{\text{Arp23}_m} \Delta [\text{Arp23}_m] + k_5 \ell [\text{Rac}_m][\text{Arp23}_c] \\ &\quad - k_{14}[\text{Arp23}_m] \end{aligned} \quad (3.25)$$

$$D_{\text{Arp23}_c} \frac{\partial}{\partial n}[\text{Arp23}_c] = -k_5 \ell [\text{Rac}_m][\text{Arp23}_c] + k_{14}[\text{Arp23}_m] \quad (3.26)$$

$$\frac{\partial}{\partial t}[\text{PTEN}_c] = D_{\text{PTEN}_c} \Delta [\text{PTEN}_c] \quad (3.27)$$

$$\begin{aligned} \frac{\partial}{\partial t}[\text{PTEN}_m] &= D_{\text{PTEN}_m} \Delta [\text{PTEN}_m] + k_6 \ell [\text{PIP2}][\text{PTEN}_c] \\ &\quad - k_{15}[\text{PTEN}_m] \end{aligned} \quad (3.28)$$

$$D_{\text{PTEN}_c} \frac{\partial}{\partial n}[\text{PTEN}_c] = -k_6 \ell [\text{PIP2}][\text{PTEN}_c] + k_{15}[\text{PTEN}_m] \quad (3.29)$$

$$\frac{\partial}{\partial t}[\text{dDia2}_c] = D_{\text{dDia2}_c} \Delta [\text{dDia2}_c] \quad (3.30)$$

$$\begin{aligned} \frac{\partial}{\partial t}[\text{dDia2}_m] &= D_{\text{dDia2}_m} \Delta [\text{dDia2}_m] + k_8 \ell [\text{PIP2}][\text{dDia2}_c] \\ &\quad - k_{16}[\text{dDia2}_m] \end{aligned} \quad (3.31)$$

$$D_{\text{dDia2}_c} \frac{\partial}{\partial n}[\text{dDia2}_c] = -k_8 \ell [\text{PIP2}][\text{dDia2}_c] + k_{16}[\text{dDia2}_m] \quad (3.32)$$

### 3.3. Theoretical Model of the Reaction-Diffusion System

---

$$\begin{aligned} \frac{\partial}{\partial t} [\text{ActinB}] &= D_{\text{ActinB}} \Delta [\text{ActinB}] + \frac{k_9}{1 + \alpha \cdot d\text{Dia}_2m} [\text{Arp23}_m][\text{ActinM}] \\ &\quad - k_{19} [\text{ActinB}] \end{aligned} \quad (3.33)$$

$$\begin{aligned} \frac{\partial}{\partial t} [\text{ActinL}] &= D_{\text{ActinL}} \Delta [\text{ActinL}] + k_{10} [d\text{Dia}_2m][\text{ActinM}] \\ &\quad - k_{18} [\text{ActinL}] \end{aligned} \quad (3.34)$$

$$\begin{aligned} \frac{\partial}{\partial t} [\text{ActinM}] &= D_{\text{ActinM}} \Delta [\text{ActinM}] - \frac{k_9}{1 + \alpha \cdot d\text{Dia}_2m} [\text{Arp23}_m][\text{ActinM}] \\ &\quad - k_{10} [d\text{Dia}_2m][\text{ActinM}] + k_{18} [\text{ActinL}] + k_{19} [\text{ActinB}] \end{aligned} \quad (3.35)$$

#### 3.3.3 Conservation Laws

To simplify our model, we derive the underlying conservation laws. Herein, a conserved quantity is in the form of total molecules per cell. So, for a given species, the total number of molecules in distinct states (e.g., at the membrane, bound to a complex, or freely diffusing in the cytosol) remains constant. This assumption is only valid if kinetic parameters are significantly larger than the assembly or denaturation processes for the species considered. For the exposition here, we show how one can deduce a conservation law starting from equation (3.12). In such a case, species  $A$  exists in only two states: bound to the membrane and freely diffusing in the cytosol. As before, we let  $x \in \Omega$ , and  $y \in \partial\Omega$  then, note that for a fixed  $t$ , the total number of molecules  $A_t$  is given by:

$$A_t = \int_{\partial\Omega} [A_m](y, t) dy + \int_{\Omega} [A_c](x, t) dx. \quad (3.36)$$

To inspect the change of  $A_t$  with respect to time, we take the partial derivative of the above equation; explicitly,

$$\frac{\partial}{\partial t} A_t = \int_{\partial\Omega} \frac{\partial}{\partial t} [A_m](y, t) dy + \int_{\Omega} \frac{\partial}{\partial t} [A_c](x, t) dx. \quad (3.37)$$

### 3.3. Theoretical Model of the Reaction-Diffusion System

---

With the relations given by (3.12) we have that

$$\begin{aligned} \frac{\partial}{\partial t} A_t &= \int_{\partial\Omega} D_m \Delta [A_m](y, t) - k_2 [A_m](y, \ell) + k_1 \ell [B_m](y, t) [A_c](y, t) dy \\ &\quad + \int_{\Omega} D_c \Delta [A_c](x, t) dx. \end{aligned} \quad (3.38)$$

Using the divergence theorem, applied to the second integral, we obtain

$$\frac{\partial}{\partial t} A_t = \int_{\partial\Omega} D_m \Delta [A_m](y, t) - k_2 [A_m](y, \ell) + k_1 \ell [B_m](y, t) [A_c](y, t) dy \quad (3.39)$$

$$+ \int_{\partial\Omega} D_c \frac{\partial}{\partial n} \cdot [A_c](x, t) dy. \quad (3.40)$$

Now, substituting the boundary condition (3.12), we have

$$\frac{\partial}{\partial t} A_t = \int_{\partial\Omega} D_m \Delta [A_m](y, t) - k_2 [A_m](y, \ell) + k_1 \ell [B_m](y, t) [A_c](y, t) dy \quad (3.41)$$

$$+ \int_{\partial\Omega} k_2 [A_m](y, t) - k_1 \ell [B_m](y, t) [A_c](y, t) dy. \quad (3.42)$$

It should be clear that  $\frac{\partial}{\partial t} A_t = \int_{\partial\Omega} D_m \Delta A_m[y, t] dy$ . Using the divergence theorem once more and noting that the boundary of  $\partial\Omega$  is empty (as it is a closed surface), we obtain the desired result,

$$\frac{\partial}{\partial t} A_t = 0. \quad (3.43)$$

Therefore,  $A_t$  is constant. It follows that our model admits the following conservation laws

$$\int_{\Omega} Ras_c dx + \int_{\partial\Omega} Ras_m dy = Ras_{tot} \quad (3.44)$$

$$\int_{\Omega} PI3K_c dx + \int_{\partial\Omega} PI3K_m dy = PI3K_{tot} \quad (3.45)$$

$$\int_{\partial\Omega} PIP2 + PIP3 dy = PIP_{tot} \quad (3.46)$$

$$\int_{\Omega} PTEN_c dx + \int_{\partial\Omega} PTEN_m dy = PTEN_{tot} \quad (3.47)$$

$$\int_{\Omega} Rac_c dx + \int_{\partial\Omega} Rac_m dy = Rac_{tot} \quad (3.48)$$

$$\int_{\Omega} dDia2_c dx + \int_{\partial\Omega} dDia2_m dy = Ras_{tot} \quad (3.49)$$

### 3.3. Theoretical Model of the Reaction-Diffusion System

---

$$\int_{\Omega} \text{Arp23}_c \, dx + \int_{\partial\Omega} \text{Arp23}_m \, dy = \text{Arp23}_{\text{tot}} \quad (3.50)$$

$$\int_{\partial\Omega} \text{ActinB} + \text{ActinM} + \text{ActinL} \, dy = \text{Actin}_{\text{tot}} \quad (3.51)$$

$$(3.52)$$

#### 3.3.4 Spatially Uniform Model

Given the complexity of the model and the lack of analytical results for non-linear reaction-diffusion systems, we will further simplify the model and reduce it to a system of ODEs. This reduction is valid, as we are interested on spatially uniform protein profiles similar to how it has been done in the work of Avila M. *et al* and Cheng *et al* [24, 76]. This model will be used to analyze the response of the system under uniform stimulation using, at the same time, the well-mixed assumption.

We develop a lumped model by averaging the cytosolic and membrane concentrations across their respective domain. That is, the concentration of any species is independent of its spatial coordinate. Additionally, we will assume that binding rates are uniform across the membrane. We begin with the derivation of the corresponding equation for a general species in the cytosol.

Let  $[A_c]$  denote the concentration of a cytosolic molecule then, let its reaction-diffusion equation be of the form:

$$\frac{\partial}{\partial t} [A_c] = D_c \Delta [A_c] + \sum_i k_i f_i(\mathbf{s}) \quad (3.53)$$

where  $k_i f_i(\mathbf{s})$  denotes a general mass-action kinetic reaction dependent on the set of species  $\mathbf{s}$ . Now, define the average concentration in the cytosol as

$$[\langle A_c \rangle] = \frac{1}{|\Omega|} \int_{\Omega} [A_c] \, dx \quad (3.54)$$

### 3.3. Theoretical Model of the Reaction-Diffusion System

---

and consider its time derivative

$$\frac{d}{dt}[\langle A_c \rangle] = \frac{1}{|\Omega|} \int_{\Omega} \frac{\partial}{\partial t}[A_c] dx. \quad (3.55)$$

By substitution we have

$$\frac{d}{dt}[\langle A_c \rangle] = \frac{1}{|\Omega|} \int_{\Omega} D_c \Delta[A_c] + \sum_i k_i f_i(\mathbf{s}) dx. \quad (3.56)$$

We proceed to apply the divergence theorem on the first term inside the integral, then we have

$$\frac{d}{dt}[\langle A_c \rangle] = \frac{1}{|\Omega|} \int_{\partial\Omega} D_c \frac{\partial}{\partial n}[A_c] dy + \frac{1}{|\Omega|} \int_{\Omega} \sum_i k_i f_i(\mathbf{s}) dx. \quad (3.57)$$

Using our homogeneity assumption for binding rates and concentration profiles in the closure of  $\Omega$ , the above simplifies to

$$\frac{d}{dt}[\langle A_c \rangle] = \frac{|\partial\Omega|}{|\Omega|} D_c \frac{\partial}{\partial n}[A_c] + \sum_i k_i f_i(\mathbf{s}), \quad (3.58)$$

where the right hand side is implied to be a function of  $t$  only.

Then, we use the same principles to deduce the lumped equations for a general membrane-bound species  $[A_m]$ . Let  $[A_m]$  satisfy the reaction diffusion equation

$$\frac{\partial}{\partial t}[A_m] = D_m \Delta[A_m] + \sum_i k_i g_i(\mathbf{s}). \quad (3.59)$$

Analogous to the previous case,  $k_i g_i(\mathbf{s})$  is a general reaction dependent on the concentration of the other species  $\mathbf{s}$ . Let the average concentration of  $[A_m]$  in the membrane be defined as

$$[\langle A_m \rangle] = \frac{1}{|\partial\Omega|} \int_{\partial\Omega} [A_m] dy. \quad (3.60)$$

Now consider its time derivative

$$\frac{d}{dt}[\langle A_m \rangle] = \frac{1}{|\partial\Omega|} \int_{\partial\Omega} \frac{\partial}{\partial t}[A_m] dy \quad (3.61)$$

### 3.3. Theoretical Model of the Reaction-Diffusion System

---

$$= \frac{1}{\partial\Omega} \int_{\partial\Omega} D_m \Delta[A_m] + \sum_i k_i g_i(\mathbf{s}) \, dy. \quad (3.62)$$

In this case, applying the divergence theorem to the first integral evaluates to 0 as the boundary of  $\partial\Omega$  is empty. Thus

$$\frac{d}{dt} [\langle A_m \rangle] = \frac{1}{\partial\Omega} \int_{\partial\Omega} \sum_i k_i g_i(\mathbf{s}) \, dy. \quad (3.63)$$

Now, by our assumption of spatial invariance, the latter simplifies further to

$$\frac{d}{dt} [\langle A_m \rangle] = \sum_i k_i g_i(\mathbf{s}). \quad (3.64)$$

We will often refer to the *base network* as the network arising from the basal reaction shown in Table 3.2 (left). In Figure 3.9, solid lines make up this scenario, whereas dashed lines are feedback mechanisms that we will discuss later.

Before presenting the ordinary differential equations that correspond to our system, we note that for the above derivation, the set of functions  $f_i(\mathbf{s})$  is equal to zero. This result comes from not including cytosolic reactions in our model, only diffusion. Moreover, by construction, we have set the following:

$$D_c \frac{\partial}{\partial n} [A_c] = - \sum_i k_i g_i(\mathbf{s}).$$

It follows that the quantity  $|\partial\Omega|A_m + |\Omega|A_c$  defines a conservation law. This result should not be surprising, as we have carefully preserved species conservation.

Altogether, the corresponding equations for the spatially homogeneous basal system are:

$$\frac{d}{dt} [\text{ras}_m] = k_1 \ell[\text{g}_{\beta\gamma}] [\text{ras}_c] - k_{11} [\text{ras}_m] \quad (3.65)$$

$$\frac{d}{dt} [\text{pi3k}_m] = k_2 \ell[\text{ras}_m] [\text{pi3k}_c] - k_{12} [\text{pi3k}_m] \quad (3.66)$$

$$\frac{d}{dt} [\text{pip3}] = k_3 [\text{pip2}] [\text{pi3k}_m] - k_7 [\text{pip3}] [\text{pten}_m] - k_{17} [\text{pip3}] \quad (3.67)$$

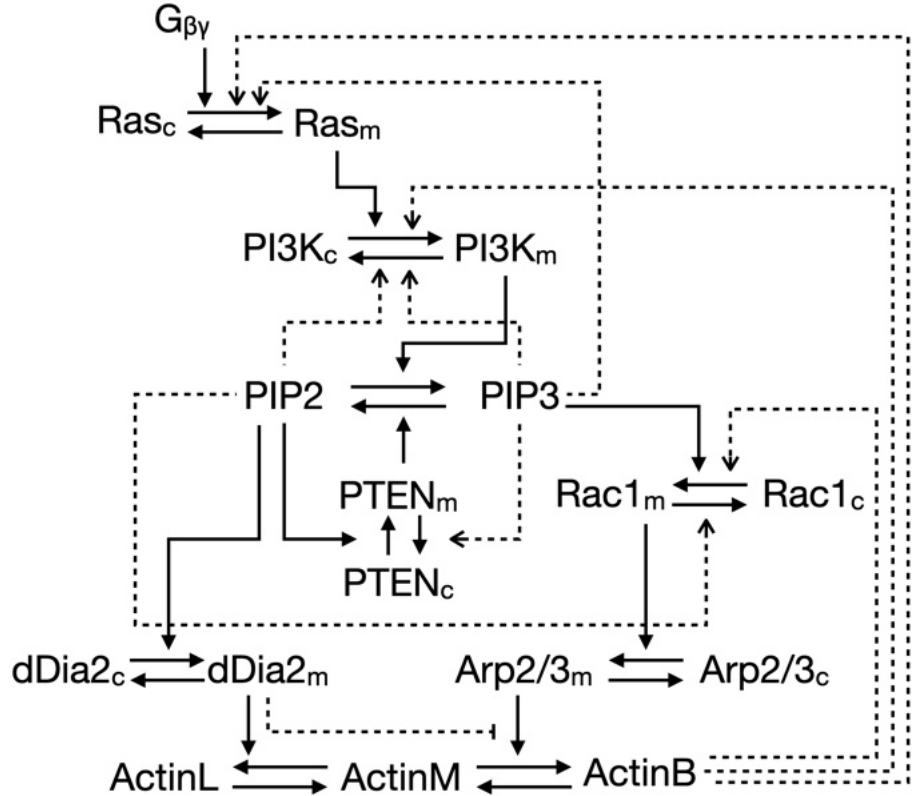


**Figure 3.9:** The *Dictyostelium discoideum* network. Solid lines indicate well established reactions. Dashed lines indicate speculated mechanisms and feedback loops.

$$\frac{d}{dt} [rac_m] = k_4 \ell [pip3] [rac_c] - k_{13} [rac_m] \quad (3.68)$$

$$\frac{d}{dt} [arp23_m] = k_5 \ell [rac_m] [arp23_c] - k_{14} [arp23_m] \quad (3.69)$$

$$\frac{d}{dt} [pten_m] = k_6 \ell [pip2] [pten_c] - k_{15} [pten_m] \quad (3.70)$$

$$\frac{d}{dt} [dia2_m] = k_8 \ell [pip2] [dia2_c] - k_{16} [dia2_m] \quad (3.71)$$

$$\frac{d}{dt} [actinB] = \frac{k_9}{1 + \alpha \cdot [dia2_m]} [arp23_m] [actinM] - k_{19} [actinB] \quad (3.72)$$

$$\frac{d}{dt} [actinL] = k_{10} [dia2_m] [actinM] - k_{18} [actinL]. \quad (3.73)$$

Equipped with the conservation laws:

$$c_1 = v[ras_c] + a[ras_m] \quad (3.74)$$

### 3.3. Theoretical Model of the Reaction-Diffusion System

---

$$c_2 = v[\text{pi3k}_c] + a[\text{pi3k}_m] \quad (3.75)$$

$$c_3 = a[\text{pip2}] + a[\text{pip3}] \quad (3.76)$$

$$c_4 = v[\text{rac}]_c + a[\text{rac}_m] \quad (3.77)$$

$$c_5 = v[\text{arp23}]_c + a[\text{arp23}_m] \quad (3.78)$$

$$c_6 = v[\text{pten}]_c + a[\text{pten}_m] \quad (3.79)$$

$$c_7 = v[\text{dia}]_c + a[\text{dia}_m] \quad (3.80)$$

$$c_8 = a[\text{actinB}] + a[\text{actinM}] + a[\text{actinL}] \quad (3.81)$$

Note the use of lowercase variables of the species. This choice is to distinguish the averaged variables from the local species in equations (3.13)-(3.32). Above,  $a$ ,  $v$ , and  $\ell$  represent a cell's surface area, volume, and membrane thickness. We use  $c_i$  for the conserved quantities. The conserved quantities are the total molecule count of a given species inside a cell or across the membrane, depending on the protein domain. We list typical values in Tables 3.4 and 3.3.

Label	Description	Value	Reference
$Ras^T$	Total Ras molecules at the membrane	300,000#/cell	[24]
$Rac^T$	Total Rac1 molecules at the membrane	1,000,000#/cell <sup>b</sup>	[81]
$PI3K^T$	Total PI3K molecules	16,000#/cell <sup>b</sup>	[82]
$PTEN^T$	Total PTEN molecules	16,000#/cell <sup>b</sup>	[82]
$SCAR/W^T$	Total SCAR/WAVE molecules at the membrane	10,000*	
$Arp2/3^T$	Total Arp2/3 molecules at the membrane	2,000#/cell	[83][84]
$G_{\beta\gamma}^T$	Total G protein molecules	300,000#/cell	[24]
$PIP2$	Typical levels of PIP2	4,000,000#/cell <sup>b</sup>	[81]
$PIP3$	Typical levels of PIP3	7,000#/cell <sup>b</sup>	[81]

<sup>a</sup>Computed from concentration, assuming cell volume  $\approx 2.618^{-13}\text{L}$ .

<sup>b</sup>Computed from concentration, assuming surface area per cell  $\approx 235.62\mu\text{m}^2$ .

**Table 3.3:** Total concentration values.

## 3.4 Results

### 3.4.1 Multistationary Analysis of the Base Network

In this section, we describe the conclusions coming from the multistationary theorems applied to the *basal* set of reactions as depicted in [3.2](#). In Dictyostelium, experimental observations validate the existence of mutually exclusive patterns across the membrane that dictate cytoskeleton properties. On one end, high PIP3 and low PIP2 concentrations promote the accumulation of dendritic actin networks that produce forward forces. Conversely, low PIP3 and high PIP2 profiles enhance myosin recruitment, leading to contractile forces. When properly orchestrated, these responses give rise to wave patterns at the membrane [\[40\]](#). Here we identify sufficient conditions for the existence of the underlying bistability. Additionally, we describe minimal sets of biochemical reactions that give rise to bistable systems. Similarly, we provide a *maximal* set of appended mechanisms that preserves the uniqueness of the steady state and theoretically disrupts wave patterns. Lastly, we uncover consistent parameter values and propose targeted perturbations on the network structure that either rescue or severe bistability.

We begin by inspecting the base reaction network (equations [3.65 - 3.73](#)). First, we show that the hypotheses of the multistationary theorems, namely, that our network is dissipative and contains no boundary equilibria, are fulfilled. Secondly, we prove that the network structure does *not* admit multiple steady states. For simplicity, we have lumped the kinetic rate constants from the system. Namely, expressions such as  $k_1 \ell$  are rewritten simply as  $k_1$ . Up to re-scaling of the parameters, the system is equivalent to that of reactions  $\mathcal{R}_1 - \mathcal{R}_{19}$  (Table [3.2](#)) under mass-action kinetics. Additionally, we let the inhibition coefficient of Arp2/3 by dDia2 be zero  $\alpha = 0$ ; we will revisit the effect of  $\alpha$  later.

Now, let  $\mathbf{x} = [\text{ras}_c, \text{ras}_m, \text{pi3k}_c, \text{pi3k}_m, \text{pip2}, \text{pip3}, \text{rac}_c, \text{rac}_m, \text{arp23}_c, \text{arp23}_m, \text{pten}_c,$

$\text{pten}_m, \text{dia}_c, \text{dia}_m, \text{actinM}, \text{actinL}, \text{actinB}]^T$ . Moreover, let the stoichiometric matrix and reaction-rate functions  $N$  and  $\mathbf{v}(\mathbf{x})$  arise from mass action kinetics.

We begin with the following lemma:

**Lemma 3.4.1.** *The base network (solid lines in Figure 3.9) is both dissipative and contains no boundary steady states.*

*Proof.* To prove that the network is dissipative, it suffices to show that it is a conservative network. Therefore, we show that each species is present in at least one conservation law. This result is clear from equations (3.74) - (3.81). A more general approach is to inspect the orthogonal complement of the image for the underlying stoichiometric matrix. The network is conservative if a strictly positive vector exists in this space. In our case, the space is spanned by the columns of the matrix:

$$\begin{pmatrix} 1 & 1 & 0 & 0 & 0 & 0 & 0 & 0 & 0 & 0 & 0 & 0 & 0 & 0 & 0 & 0 & 0 \\ 0 & 0 & 1 & 1 & 0 & 0 & 0 & 0 & 0 & 0 & 0 & 0 & 0 & 0 & 0 & 0 & 0 \\ 0 & 0 & 0 & 0 & 1 & 1 & 0 & 0 & 0 & 0 & 0 & 0 & 0 & 0 & 0 & 0 & 0 \\ 0 & 0 & 0 & 0 & 0 & 0 & 1 & 1 & 0 & 0 & 0 & 0 & 0 & 0 & 0 & 0 & 0 \\ 0 & 0 & 0 & 0 & 0 & 0 & 0 & 0 & 0 & 1 & 1 & 0 & 0 & 0 & 0 & 0 & 0 \\ 0 & 0 & 0 & 0 & 0 & 0 & 0 & 0 & 0 & 0 & 0 & 1 & 1 & 0 & 0 & 0 & 0 \\ 0 & 0 & 0 & 0 & 0 & 0 & 0 & 0 & 0 & 0 & 0 & 0 & 1 & 1 & 0 & 0 & 0 \\ 0 & 0 & 0 & 0 & 0 & 0 & 0 & 0 & 0 & 0 & 0 & 0 & 0 & 1 & 1 & 0 & 0 \end{pmatrix}$$

It should be clear that the “ones” vector is in this space. Therefore the network is conservative and hence dissipative.

To prove that our network has no boundary equilibria, we use the siphon theorems in [72]. A *siphon* is a set of species  $Z \subseteq \{X_1, \dots, X_n\}$  with the following property: if  $X_i \in Z$

then, for every reaction  $R_j$  with  $X_i$  as a product, at least one of the reactants of  $R_j$  is also in  $Z$ . A *minimal siphon* is a siphon that does not properly contain any other siphon.

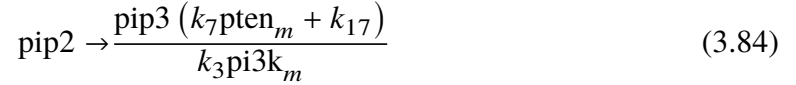
**Lemma 3.4.2** (Siphon Criterion). *If for every minimal siphon  $Z$  there exist a subset  $\{X_{i_1}, \dots, X_{i_k}\} \subseteq Z$ , and a conservation relation  $\lambda_1 x_{i_1} + \dots + \lambda_k x_{i_k} = c$  for some positive  $\lambda_1, \dots, \lambda_k$ , then the network has no boundary equilibria.*

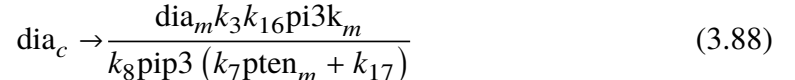
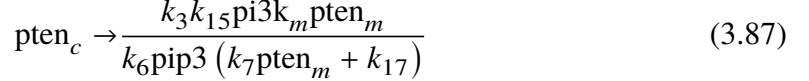
It is easy to check that all the minimal siphons of our network are:

$$\begin{array}{lll} \{\text{ras}_c, \text{ras}_m\} & \{\text{pi3k}_c, \text{pi3k}_m\} & \{\text{pip2}, \text{pip3}\} \\ \{\text{rac}_c, \text{rac}_m\} & \{\text{arp23}_c, \text{arp23}_m\} & \{\text{pten}_c, \text{pten}_m\} \\ \{\text{dia}_c, \text{dia}_m\}, \quad \{\text{actinB}, \text{actinM}, \text{actinL}\} & & \end{array}$$

In addition to the conserved actin species, these are the pair-wise sets of cytosolic and membrane-bound species, which are also conserved quantities. The siphon criterion shows that the network has no boundary equilibrium.  $\square$

To save space, we omit the explicit form of the stoichiometric matrix  $N \in \mathbf{R}^{17 \times 19}$ . However, we have that  $\text{Rank}(N) = 9$ . Therefore, it is possible to parameterize nine of our variables at a steady state. In general, it is not always the case that a parametrization exists, and the existence of such expressions depends highly on the system. In our case, this is possible, and following Definition 3.2.17, we have a positive re-parametrization  $\mathbf{x} = \Phi(\hat{\mathbf{x}})$  given by:





With the above map, we are ready to apply the multistationarity theorems. Here, the critical function  $C(\kappa, \hat{\mathbf{x}})$  will be a rational expression in the variables:  $\text{ras}_m, \text{pi3k}_m, \text{pip}3, \text{rac}_m, \text{arp23}_m, \text{pten}_m, \text{dia}_m, \text{actinM}, k_1, k_2, \dots, k_{19}$ . The network will admit multiple steady states if there exists a parameter set for which the sign of  $C(\kappa, \hat{\mathbf{x}})$  is positive ( $(-1)^{\text{rank}(N)+1} = 1$ ). We omit the explicit form of  $C$  as it has a numerator with 1248 terms and a denominator equal to  $k_7 k_3^2 \text{pi3k}_m^2 \text{pten}_m + k_{17} k_3^2 \text{pi3k}_m^2$ . However, all of the terms in the numerator have a negative sign! This result leads to the following lemma.

**Lemma 3.4.3.** *The basal Dictyostelium network  $\mathcal{R}$  admits a **unique equilibrium** for any choice of positive parameters.*

Hereafter, we will refer to the basal network of *Dictyostelium discoideum* as  $\mathcal{R}$ .

### 3.4.2 Feedback Analysis

We have established that the base network  $\mathcal{R}$  will admit a unique equilibrium for all choices of kinetic parameters. We now want to inspect this mono-stationary property's robustness against the introduction of feedback mechanisms. As we did for  $\mathcal{R}$  in the previous section, we can test for the uniqueness of equilibria after appending new reactions to the network.

Based on hypothesized mechanisms found in literature, we test the possible reactions  $\mathcal{J}_i$  for  $1 \leq i \leq 8$ . The explicit form of these reactions appears in Table 3.2 (right side). We will test all 256 possible combinations and characterize their capacity for multiple steady states. Given that the behavior of the actin wave patterns appears to be that of a bistable system, we are particularly interested in networks that admit multiple steady states.

Before proceeding, we note that conservation laws remain preserved in these networks. Thus, the network is dissipative. Moreover, since we are not introducing new species to the model or introducing outflow or inflow reactions, the network's minimal siphons remain unchanged. Therefore there will be no boundary equilibria. This result guarantees that the multistationarity theorems are valid in all cases.

Noteworthy, the computations required to analyze the characteristic function of the network are expensive. On the one hand, we need to compute the determinant of the Jacobian of a large matrix. On the other hand, for specific cases, we will compute the *convex hull* of the underlying critical function  $C(\kappa, \mathbf{x})$ . The last step will be described later. However, this method is easily programmable, and as we will see here, one can characterize all possible combinations of moderate ( 20 species) networks.

### 3.4.3 Single Steady-State Networks

We begin by presenting the results pertaining *monostationary* networks. That is, networks that preserve the mono-stationary properties of  $\mathcal{R}$ . Afterward, we will describe networks with multistationary properties. However, before diving into the latter, we define Newton polytopes and convex hulls as these are needed to investigate such networks further.

### Single-Mechanism, Single Steady-State Networks

Let us focus first on single mechanisms that do *not* change the behavior of the base network  $\mathcal{R}$ . That is, feedback reactions for which *any* choice of kinetic parameters still engenders a *unique* steady state for any choice of kinetic parameters. Hence, we have the following lemma.

**Lemma 3.4.4.** *The base network  $\mathcal{R}$ , when extended by any single element in the set of reactions  $\{\mathcal{J}_3, \mathcal{J}_4, \mathcal{J}_5, \mathcal{J}_6, \mathcal{J}_8\}$  is monostationary.*

Explicitly, in our set-up, following feedback mechanisms yield a unique steady-state in the underlying ODE system, but only if no other reactions are appended:

$$\begin{aligned}\mathcal{J}_3 &:= \text{ActinB}_m + \text{Rac}_c \xrightarrow{m_3} \text{ActinB}_m + \text{Rac}_m \\ \mathcal{J}_4 &:= \text{PIP3} + \text{Ras}_c \xrightarrow{m_4} \text{PIP3} + \text{Ras}_m \\ \mathcal{J}_5 &:= \text{PIP3} + \text{PTEN}_m \xrightarrow{m_5} \text{PIP3} + \text{PTEN}_c \\ \mathcal{J}_6 &:= \text{PIP3} + \text{PI3K}_m \xrightarrow{m_6} \text{PIP3} + \text{PI3K}_c \\ \mathcal{J}_8 &:= \text{PIP2} + \text{Rac}_m \xrightarrow{m_8} \text{PIP2} + \text{Rac}_c\end{aligned}$$

In Figure 3.10, we show the networks corresponding to the appendages below. The proof for this result is analogous for each case. Therefore, we take  $\mathcal{R} \oplus \mathcal{J}_3$  as a model case to prove.

*Proof.* The network  $\mathcal{R} \oplus \mathcal{J}_3$  admits a unique steady state. First, we remark that the conservation quantities remain unchanged from those of  $\mathcal{R}$ ; thus, the network is conservative. Similarly, using Lemma 3.4.2 and the fact that all minimal siphons of the network  $\mathcal{R} \oplus \mathcal{J}_3$  remain the same as for  $\mathcal{R}$ , we conclude that the network is dissipative. Thus the hypothesis of Theorems 3.2.19 is fulfilled. We find a similar positive reparametrization of steady states

### 3.4. Results

to that of the network  $\mathcal{R}$  as shown above in equations (3.82) - (3.90). The only exception is the map for  $\text{rac}_c$  which becomes:

$$\text{rac}_c \rightarrow \frac{k_{13}k_{19}\text{rac}_m}{m_3k_9\text{actinMarp23}_m + k_4k_{19}\text{pip3}}.$$

Moving on with the analysis, we compute the rank of the corresponding stoichiometric matrix and conclude that the network will admit a unique steady-state if the sign of the critical function  $C(\kappa, \hat{\mathbf{x}}) = -1$ . Indeed, this is the case. The critical function is a rational expression whose denominator contains four positive terms (which we omit) and whose numerator contains 2912 terms, all of which have negative coefficients (again, we omit the explicit form). Therefore, by Proposition 3.2.19, part B), the network  $\mathcal{R} \oplus \mathcal{J}_3$  is *monostationary*.  $\square$

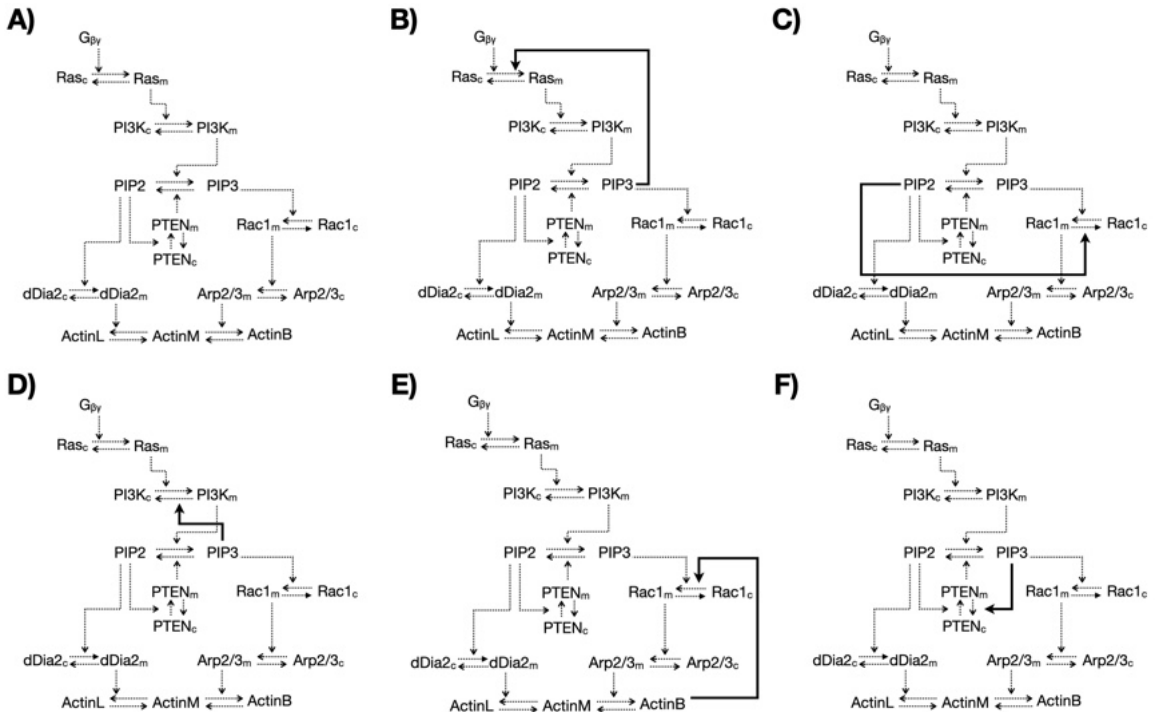


**Figure 3.10:** Single-mechanism, single-steady state networks. A) Base network  $\mathcal{R}$ . B)-F) Single steady-state networks arising from appending only one feedback mechanism.

### Multiple-Mechanism, Single Steady-State Networks

As stated before, we can systematically inspect the number of stationary solutions a given network has using Proposition 3.2.19. This outcome is dependent on satisfying the required hypotheses. As we have seen here, it suffices to guarantee species conservation and account for the necessary decay and production rates. Biologically, one can argue that this is more realistic than ignoring such rates, as it is often done to simplify computations. That aside, we systematically tested all 256 possible combinations of feedback mechanisms appended to  $\mathcal{R}$ . As far as mono-stationary networks are concerned, the following cases admit a *unique* equilibrium. We state the result in the form of a lemma.

**Lemma 3.4.5.** *Let  $\mathcal{P}(S)$  be the power set of  $S$ , let  $J = \{\mathcal{J}_3, \mathcal{J}_6, \mathcal{J}_8\}$ , and  $K = \{\mathcal{J}_4, \mathcal{J}_5\}$  following the definition in Table 3.2. The network  $\mathcal{R}$ , when extended by any set in the family of reactions:*

$$\mathcal{P}(J \cup K) \setminus \left( \bigcup_{\Lambda \in \mathcal{P}(J)} K \cup \Lambda \right)$$

*admits a **unique** steady-state, for all choices of positive kinetic parameters.*

In other words, we can append most combinations of the feedback shown earlier and still get a network with a unique steady state. The only exceptions to this rule are those networks that contain *both*  $\mathcal{J}_4$  and  $\mathcal{J}_5$ . This conclusion is a peculiar finding in our setup. Going back to the meaning of these reactions, neither positive feedback from PIP3 to Ras nor negative feedback from PIP3 to PTEN can yield multiple equilibria on its own. However, the combined action of the two mechanisms does generate multiple steady-states. We prove this fact later.

Here, we introduce a notion of order when talking about reaction networks. We say that a network  $A$  is *bigger* than  $B$  ( $A > B$ ), if the reaction set  $\mathcal{R}_A$  and  $\mathcal{R}_B$  satisfies  $\mathcal{R}_A \supset \mathcal{R}_B$ .

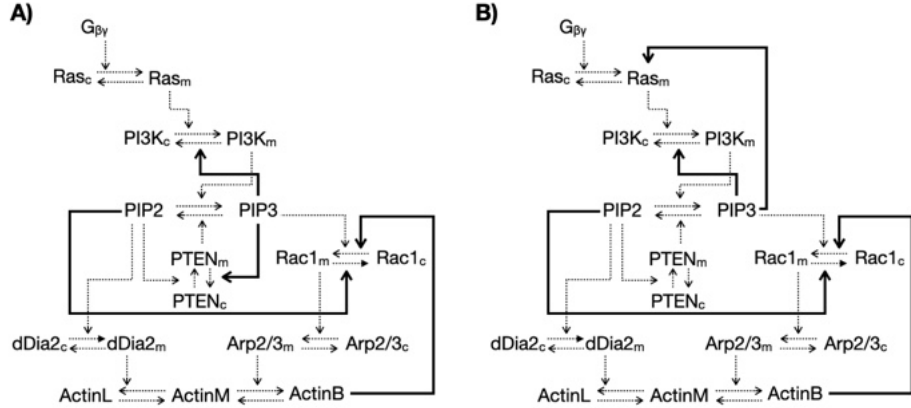


**Figure 3.11:** Maximal monostationary networks. The biggest set of reactions that still preserve single steady-state dynamics in our set-up. A)  $\mathcal{R} \oplus \{\mathcal{J}_3, \mathcal{J}_5, \mathcal{J}_6, \mathcal{J}_8\}$ . B)  $\mathcal{R} \oplus \{\mathcal{J}_3, \mathcal{J}_4, \mathcal{J}_6, \mathcal{J}_8\}$

Thus, a network  $A$  is said to be *maximal* if it is not contained in any other reaction set. We arrive at the following lemma.

**Lemma 3.4.6.** *For the reactions defined in Table 3.2, there are exactly two maximal monostationary networks:*

- i.  $\mathcal{R} \oplus \{\mathcal{J}_3, \mathcal{J}_5, \mathcal{J}_6, \mathcal{J}_8\}$ , and
- ii.  $\mathcal{R} \oplus \{\mathcal{J}_3, \mathcal{J}_4, \mathcal{J}_6, \mathcal{J}_8\}$ .

The diagram of these two networks is included in 3.11.

### 3.4.4 Multiple Steady-State Networks

In the last section, we showed all networks that, in our setting, maintain a unique steady state, similar to the base *Dictyostelium discoideum* network. This subsection describes the feedback mechanisms that give rise to multiple equilibria. In general, once we get the critical function of the system, we need to find criteria that satisfy either conclusion in Proposition 3.2.19. For example, on the one hand, if a system has a unique steady state, then all signs

of the numerator's terms in the critical function are equal and satisfy a constraint. On the other hand, if the system is to admit multiple equilibria, we need to find parameter regions for which the critical function has the desired sign. This latter conclusion is non-trivial to approach. Explicitly, if a rational function has terms with both positive and negative signs, what can we conclude about the sign of the overall expression? In particular, for what values is the function positive or negative? One approach appears in [71], which uses the idea of Newton polytopes in order to find compatible parameter regions; however, this approach might still fail in some cases. Luckily, in our model, this method works every time. Moreover, we can provide parameter regions for most networks that yield multiple steady-states. We describe our results below.

First, let's define some objects that are useful, we borrow the notation from [70].

**Definition 3.4.7** (Newton Polytope). *Consider a real, multivariate polynomial*

$$f = a_1 x^{\sigma_1} + a_2 x^{\sigma_2} + \dots + a_\ell x^{\sigma_\ell} \in \mathbf{R}[x_1, x_2, \dots, x_s] \quad (3.91)$$

where the  $\sigma_i$ 's are distinct and, for all  $i$ , we have  $a_i \neq 0$  and  $\sigma_i \in \mathbf{Z}^s$ . The Newton polytope off is the convex hull of its exponent vectors:

$$\text{NP}(f) := \text{conv}\{\sigma_1, \sigma_2, \dots, \sigma_\ell\} \subseteq \mathbf{R}^s$$

**Lemma 3.4.8** (2.2 in [70]). *For a real, multivariate polynomial  $f$  as in (3.91), if  $\sigma_i$  is a vertex of  $\text{NP}(f)$ , then there exists  $x^* \in \mathbf{R}_{>0}^s$  such that  $f(x^*)$  and  $a_i$  have the same sign.*

Then, let  $C(\kappa, \hat{x})$  be a rational function whose denominator terms are all positive. Then, if any term of the critical function's numerator has a sign equal to  $(-1)^{\text{Rank}(N)}$  and is a vertex of the convex hull for the associated Newton polytope, then the network has multiple equilibria.

We now show the Newton polytope method applied to our ongoing *Dictyostelium discoideum* network.

### Single-Mechanism, Multistationary Networks

We begin by stating the following lemma.

**Lemma 3.4.9.** *The base network  $\mathcal{R}$ , when extended by any single element in the set of reactions  $\{\mathcal{J}_1, \mathcal{J}_2, \mathcal{J}_7\}$  admits multiple steady states.*

As we did earlier, we will only show the proof of one case, namely  $\mathcal{R} \oplus \mathcal{J}_1$  as the rest have analogous proof. The diagrams for these multistationary networks is included in Figure 3.12.

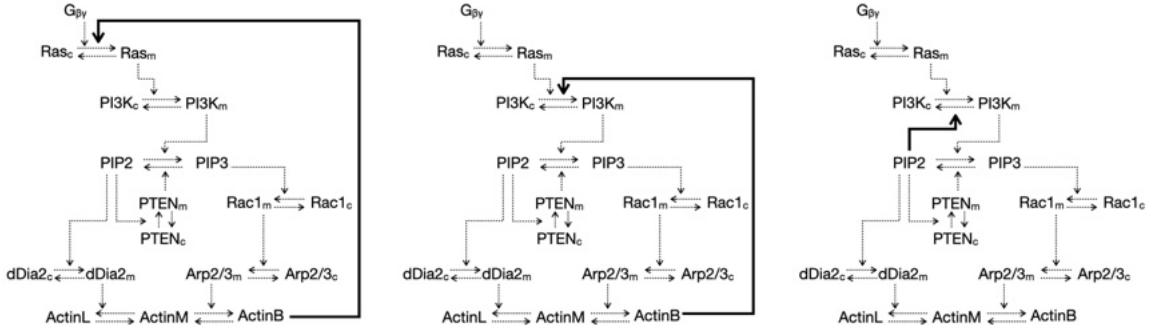


**Figure 3.12:** Single-mechanism, multiple steady-state networks. Multistationary networks with a single feedback mechanism.

*Proof.* The network  $\mathcal{R} \oplus \mathcal{J}_1$  admits multiple steady states. First, note that the network preserves the same conservation laws and minimal siphons. Thus, the network is both conservative and dissipative. Thus, the hypotheses of Proposition 3.2.19 is satisfied. Next, we find a positive reparametrization of steady states by solving the underlying dynamical system. We obtain:

$$\text{ras} \rightarrow \frac{k_{11}k_{19}\text{ras}_m}{\text{actinM } \text{arp23}_m k_9 m_1 + k_1 k_{19}} \quad (3.92)$$

$$\text{pi3k}_c \rightarrow \frac{k_{12}\text{pi3k}_m}{k_2\text{ras}_m} \quad (3.93)$$

$$\text{pip2} \rightarrow \frac{\text{pip3} (k_7\text{pten}_m + k_{17})}{k_3\text{pi3k}_m} \quad (3.94)$$

$$\text{rac}_c \rightarrow \frac{k_{13}\text{rac}_m}{k_4\text{pip3}} \quad (3.95)$$

$$\text{arp23}_c \rightarrow \frac{\text{arp23}_m k_{14}}{k_5\text{rac}_m} \quad (3.96)$$

$$\text{pten}_c \rightarrow \frac{k_3 k_{15} \text{pi3k}_m \text{pten}_m}{k_6 \text{pip3} (k_7 \text{pten}_m + k_{17})} \quad (3.97)$$

$$\text{dia}_c \rightarrow \frac{\text{dia}_m k_3 k_{16} \text{pi3k}_m}{k_8 \text{pip3} (k_7 \text{pten}_m + k_{17})} \quad (3.98)$$

$$\text{actinL} \rightarrow \frac{\text{actinM dia}_m k_{10}}{k_{18}} \quad (3.99)$$

$$\text{actinB} \rightarrow \frac{\text{actinM arp23}_m k_9}{k_{19}}. \quad (3.100)$$

Then, as before, we compute the critical function  $C(\kappa, \hat{\mathbf{x}})$ . This rational expression has a denominator with positive terms and a numerator with 1192 terms, four of which are positive and the rest negative. Since the stoichiometric matrix has rank 9, the network would admit multiple steady states if  $\text{Sign}[C(\kappa, \hat{\mathbf{x}})] = 1^{10} = 1$ . Thus, we must prove that this is the case.

Following the Newton polytope method, we investigate the terms of  $C(\kappa, \hat{\mathbf{x}})$  that are positive. The relevant terms are:

- i.  $k_3^3 k_4 k_5 k_7 k_9 k_{10} k_{11} k_{12} k_{15} k_{16} k_{19}^2 m_1 \cdot \text{actinM arp23}_m \text{dia}_m \text{pi3k}_m^3 \text{pip3 pten}_m \text{rac}_m$
- ii.  $k_3^3 k_4 k_7 k_9 k_{10} k_{11} k_{12} k_{14} k_{15} k_{16} k_{19}^2 m_1 \cdot \text{actinM arp23}_m \text{dia}_m \text{pi3k}_m^3 \text{pip3 pten}_m$
- iii.  $k_3^3 k_5 k_7 k_9 k_{10} k_{11} k_{12} k_{13} k_{15} k_{16} k_{19}^2 m_1 \cdot \text{actinM arp23}_m \text{dia}_m \text{pi3k}_m^3 \text{pten}_m \text{rac}_m$

$$\text{iv. } k_3^3 k_7 k_9 k_{10} k_{11} k_{12} k_{13} k_{14} k_{15} k_{16} k_{19}^2 m_1 \cdot \text{actinM arp23}_m \text{ dia}_m \text{ pi3k}_m^3 \text{ pten}_m .$$

The convex hull computation for the underlying polynomial is beyond the scope of this work. However, highly optimized algorithms are implemented in existing software tools such as Maple, Mathematica, C+, and MATLAB. Here, we implement MATLAB's algorithm, which relies on Barber's work [85]. Out of the 1192 possible vertices, 584 are vertices of the convex hull. In particular, all four terms listed above i) - iv) are on that set. Therefore, choices of parameters exist that admit multiple equilibria in the network.

Note that the kinetic term  $m_1$  is present in all these terms. Thus, the critical function will be negative in the limit,  $\lim_{m_1 \rightarrow 0}$ . This conclusion agrees with the earlier discovery that  $\mathcal{R}$  is a single equilibrium system. It is less trivial to determine the value of  $m_1$  for which  $C(\kappa, \hat{\mathbf{x}})$  changes sign. This threshold value would be highly dependent on the choice of the rest of the parameters. We leave this discussion for later.  $\square$

The other two networks,  $\mathcal{R} \oplus \mathcal{J}_2$  and  $\mathcal{R} \oplus \mathcal{J}_7$  have analogous proofs, so we omit the details. Below are the terms in the set of convex hull vertices relevant to admitting multiple equilibria. The numerator of  $C(\kappa, \hat{\mathbf{x}})$  has 964 terms when appending  $\mathcal{J}_2$ ; and 468 terms when appending  $\mathcal{J}_7$ . Of them, 484 and 216 are vertices of the underlying convex hull, respectively.

For  $\mathcal{R} \oplus \mathcal{J}_2$ , four terms have sign  $(-1)^{\text{Rank}(N)+1} = 1$  and are vertices of the convex hull, these terms are:

- i.  $k_1 k_4 k_5 k_7 k_9 k_{10} k_{12} k_{15} k_{16} k_{19}^2 k_3^3 m_2 + k_4 k_5 k_7 k_9 k_{10} k_{11} k_{12} k_{15} k_{16} k_{19}^2 k_3^3 m_2 \cdot \text{actinM arp23}_m \text{ dia}_m \text{ pi3k}_m^3 \text{ pip3}_m \text{ pten}_m \text{ rac}_m$
- ii.  $k_1 k_4 k_7 k_9 k_{10} k_{12} k_{14} k_{15} k_{16} k_{19}^2 k_3^3 m_2 + k_4 k_7 k_9 k_{10} k_{11} k_{12} k_{14} k_{15} k_{16} k_{19}^2 k_3^3 m_2 \cdot \text{actinM arp23}_m \text{ dia}_m \text{ pi3k}_m^3 \text{ pip3}_m \text{ pten}_m$

- iii.  $k_1 k_5 k_7 k_9 k_{10} k_{12} k_{13} k_{15} k_{16} k_{19}^2 k_3^3 m_2 + k_5 k_7 k_9 k_{10} k_{11} k_{12} k_{13} k_{15} k_{16} k_{19}^2 k_3^3 m_2 \cdot \text{actinM arp23}_m$   
 $\text{dia}_m \text{ pi3k}_m^3 \text{ pten}_m \text{ rac}_m$
- iv.  $k_1 k_7 k_9 k_{10} k_{12} k_{13} k_{14} k_{15} k_{16} k_{19}^2 k_3^3 m_2 + k_7 k_9 k_{10} k_{11} k_{12} k_{13} k_{14} k_{15} k_{16} k_{19}^2 k_3^3 m_2 \cdot \text{actinM arp23}_m$   
 $\text{dia}_m \text{ pi3k}_m^3 \text{ pten}_m .$

For  $\mathcal{R} \oplus \mathcal{J}_7$ , 26 terms have sign  $(-1)^{\text{Rank}(N)+1} = 1$  and are vertices of the convex hull.

We omit them as it is a lengthy list. However, we show one conclusion immediately from looking at a particular term. Explicitly, let us look at

$$-k_3^3 k_4 k_5 k_7^2 k_9 (k_1 + k_{11}) k_{16} k_{18} (k_6 k_{12} - k_{15} m_7) \cdot \text{arp23}_m \text{ pi3k}_m^3 \text{ pip3}^2 \text{ pten}_m^2.$$

We have the following lemma.

**Lemma 3.4.10.** *The network  $\mathcal{R} \oplus \mathcal{J}_7$  is multi stationary for some choice of kinetic parameters whenever  $\frac{k_6 k_{12}}{k_{15}} < m_7$ .*

In other words, if negative feedback to PI3K from PIP2 is the only mechanism present, then we can have multiple equilibria if the feedback rate  $k_7$  is greater than the localization of PTEN by PIP2.

*Proof.* Recall that we are looking for parameter regions that satisfy the hypothesis of multiple equilibria. That is, we are looking for parameters that make the coefficient of a term corresponding to a vertex of the convex hull have sign  $(-1)^{\text{Rank}(N)+1}$  (equal to +1 in this particular case). Therefore, we are solving for

$$-k_3^3 k_4 k_5 k_7^2 k_9 (k_1 + k_{11}) k_{16} k_{18} (k_6 k_{12} - k_{15} m_7) > 0.$$

Noting that all of our kinetic parameters are positive we can rearrange the equation above to

$$\frac{k_6 k_{12}}{k_{15}} < m_7.$$

□

In the above case, note that  $k_{12}$  and  $k_{15}$  are decay rates of PTEN and PI3K. If we would assume these are of a similar magnitude  $k_{12}/k_{15} \approx 1$  (a reasonable assumption), then it is sufficient to have  $k_6 < m_7$  for reaching a multistationary regime. This fact is not at all trivial for systems of this size. Other interesting results might be found by looking at the coefficients of the convex hull. For now, we move on with the characterization of our system.

### Multiple-Mechanism, Multiple Steady-State Networks

We finalize our characterization of stationarity in this section. As we briefly mentioned before, we are lucky that all networks were successfully identified by the theory we developed. In general, we do not expect this to be the case. However, the moderate size of the system aids in the characterization process. Given that the underlying Newton polytope is embedded in a dimension proportional to the number of parameters, a more significant proportion of vertices lie on the convex hull. Although this is speculative, we have looked at other networks with similar properties where the theory works in all cases. This approach is advantageous to traditional methods, where networks become biologically irrelevant due to oversimplification to move forward with the analysis. In any case, we begin this section with the following lemma:

**Lemma 3.4.11.** *With the reactions defined in Table 3.2, let  $J = \{\mathcal{J}_i\}_{i=1}^8$  be the set of feed-back mechanisms and  $\mathcal{P}$  be the power set function. A network  $\mathcal{N}$  of the form:*

$$\mathcal{N} = \mathcal{R} \bigoplus_{\substack{\psi \in S \\ S \in \mathcal{P}(J)}} \psi$$

*admits multiple steady states from some choice of kinetic parameters if and only if  $\mathcal{N}$  does not satisfy the hypothesis of Lemma 3.4.5.*

### 3.4. Results

---

In other words, a network not characterized as mono-stationary by Lemma 3.4.5 has to admit multiple steady states for some choice of kinetic parameters. With this result, we can classify all resulting networks. Of 256 possible combinations, 232 admit multiple equilibria, and 24 are mono-stationary. Moreover, we can identify sufficient conditions for extending the base network  $\mathcal{R}$  to a multistationary system. Any single one of the following appendages is sufficient:

- i. Positive feedback from branched actin to Ras.
- ii. Positive feedback from branched actin to PI3K.
- iii. Negative feedback from PIP2 to PI3K.
- iv. Both positive feedback from PIP3 to Ras, and negative feedback from PIP3 to PTEN.

Label	Units	Description	Value	Reference
$k_1$	$\mu\text{m}^2 \text{s}^{-1}$	Ras binding to the membrane by $G_{\beta\gamma}$	2	[24]
$k_2$	$\mu\text{m}^2 \text{s}^{-1}$	PI3K binding to the membrane by Ras	1	
$k_3$	$\mu\text{m}^2 \text{s}^{-1}$	PIP2 to PIP3 phosphorylation by PI3K	600	[12]
$k_4$	$\mu\text{m}^2 \text{s}^{-1}$	Rac1 binding to the membrane by PIP3	1	
$k_5$	$\mu\text{m}^2 \text{s}^{-1}$	Arp2/3 binding to membrane by Rac1	1	
$k_6$	$\mu\text{m}^2 \text{s}^{-1}$	PTEN binding to the membrane by PIP2	20	
$k_7$	$\mu\text{m}^2 \text{s}^{-1}$	PIP3 to PIP2 dephosphorylation by PTEN	15	[12]
$k_8$	$\mu\text{m}^2 \text{s}^{-1}$	dDia2 binding to membrane by PIP2	1	
$k_9$	$\mu\text{m}^2 \text{s}^{-1}$	Branched actin production by Arp2/3	10	
$k_{10}$	$\mu\text{m}^2 \text{s}^{-1}$	Branched actin production by dDia2	10	
$k_{11}$	$\text{s}^{-1}$	Ras unbinding from membrane	$10^{-2}$	
$k_{12}$	$\text{s}^{-1}$	PI3K unbinding from membrane	$10^{-2}$	
$k_{13}$	$\text{s}^{-1}$	Rac1 unbinding from membrane	$10^{-1}$	
$k_{14}$	$\text{s}^{-1}$	Arp2/3 unbinding from membrane	$10^{-1}$	
$k_{15}$	$\text{s}^{-1}$	PTEN unbinding from membrane	$10^{-5}$	
$k_{16}$	$\text{s}^{-1}$	dDia2 unbinding from membrane	$10^{-2}$	
$k_{17}$	$\text{s}^{-1}$	Basal PIP3 to PIP2 dephosphorylation	$2 \times 10^{-2}$	[12]
$k_{18}$	$\text{s}^{-1}$	Basal dephosphorilation of actin branches	$10^{-2}$	
$k_{19}$	$\text{s}^{-1}$	Basal dephosphorilation of actin filaments	$10^{-2}$	
$m_4$		PIP3 positive feedback to Ras	0.05	
$m_5$		PIP3 negative feedback to PTEN	50	
$D_s$	$\mu\text{m}^2 \text{s}^{-1}$	Diffusion constant for species "s"	0.01 - 10	Typical
$\ell$	$\mu\text{m}$	Membrane thickness scale	0.01	Typical
$a$	$\mu\text{m}^2$	Cell's surface area	235.6	Estimated
$v$	$\mu\text{m}^3$	Cell's volume	261.8	Estimated
$\alpha$	$\mu\text{m}^2 \text{s}^{-1}$	dDia2 inhibition factor	1	

**Table 3.4:** Rate constants recovered via the Newton polytope.

### 3.4.5 Parameter Identification in a Particular Case

We close this section by further inspecting a particular choice of network. We showed before that a sufficient condition for multistationarity for a *Dictyostelium discoideum* network (in the context of this text) is to have both positive feedback from PIP3 to Ras and negative feedback from PIP3 to PTEN. In our notation this is the network  $\mathcal{R} \oplus \mathcal{J}_4 \oplus \mathcal{J}_5$  (see Figure 3.13). However, neither of the appended mechanisms is sufficient by itself. In this subsection, we will explore this relationship further and point out how to use the critical function to find multistationary regions.

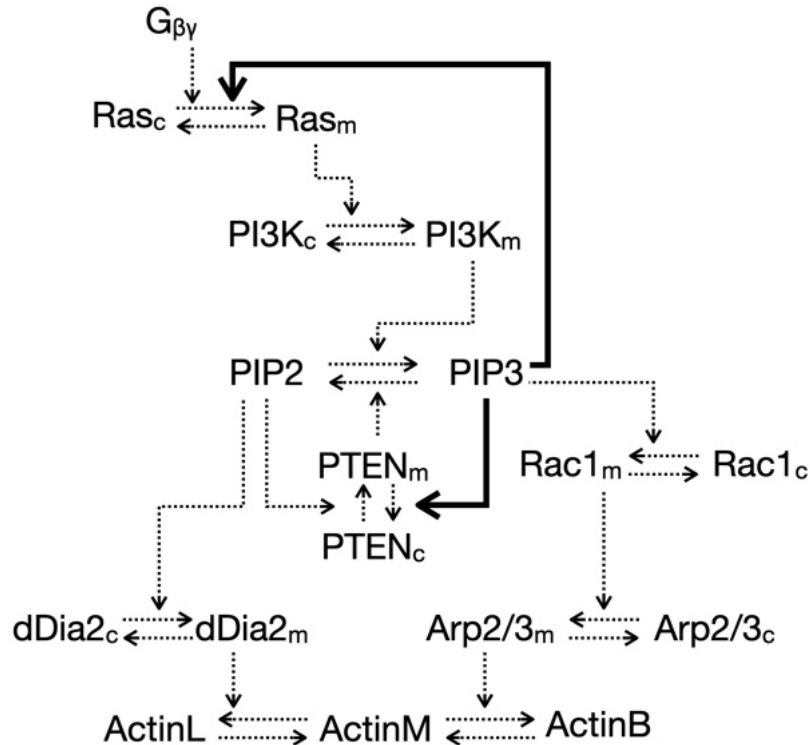


**Figure 3.13:** The network  $\mathcal{R} \oplus \mathcal{J}_4 \oplus \mathcal{J}_5$ .

First, let us note some properties of the network  $\mathcal{R} \oplus \mathcal{J}_4 \oplus \mathcal{J}_5$ . Its corresponding critical function is a rational expression with a positive denominator and a numerator that contains 744 terms. Since the rank of the stoichiometric matrix is equal to 9, we are interested in

parameters for which the sign of the critical function is negative (see Proposition 3.2.19).

Out of the 744, only 60 have negative coefficients; out of those terms, only 6 are vertices of the convex hull. We show these coefficients below. As long as we can prove any of these coefficients is positive, then we can *guarantee* the existence of parameters that yield a system with multiple equilibria.

- i.  $k_3 k_5 k_7^3 k_{12} k_{18} k_{19} (-m_4) (k_6 k_{13} k_8 m_4 + k_4 k_{15} k_8 m_4 + k_4 k_6 k_{16} m_4 - k_4 k_{11} k_8 m_5 + 2k_1 k_4 k_6 k_8 + k_4 k_6 k_{11} k_8)$
- ii.  $k_3^2 k_7^2 k_{12} k_{14} k_{16} k_{18} k_{19} (-m_4) (k_{13} k_6 m_4 + k_4 k_{15} m_4 - k_4 k_{11} m_5 + 2k_1 k_4 k_6 + k_4 k_{11} k_6)$
- iii.  $k_3^2 k_7^2 k_{10} k_{12} k_{14} k_{16} k_{19} (-m_4) (k_{13} k_6 m_4 + k_4 k_{15} m_4 - k_4 k_{11} m_5 + 2k_1 k_4 k_6 + k_4 k_{11} k_6)$
- iv.  $k_3^2 k_5 k_7^2 k_{10} k_{12} k_{16} k_{19} (-m_4) (k_{13} k_6 m_4 + k_4 k_{15} m_4 - k_4 k_{11} m_5 + 2k_1 k_4 k_6 + k_4 k_{11} k_6)$
- v.  $k_3^2 k_7^2 k_9 k_{12} k_{14} k_{16} k_{18} (-m_4) (k_{13} k_6 m_4 + k_4 k_{15} m_4 - k_4 k_{11} m_5 + 2k_1 k_4 k_6 + k_4 k_{11} k_6)$
- vi.  $-k_3 k_5 k_7^2 k_9 k_{12} k_{17} k_{18} (3k_8 k_{13} k_{15} m_4^2 + 3k_6 k_{13} k_{16} m_4^2 + 2k_1 k_8 k_{13} m_4 m_5 - 2k_8 k_{11} k_{13} m_4 m_5 + 6k_1 k_6 k_8 k_{13} m_4 + 3k_6 k_8 k_{11} k_{13} m_4 + 6k_1 k_4 k_8 k_{15} m_4 + 6k_1 k_4 k_6 k_{16} m_4 + k_1^2 k_4 k_8 m_5 + k_1 k_4 k_8 k_{11} m_5 + 3k_1^2 k_4 k_6 k_8 + 3k_1 k_4 k_6 k_8 k_{11})$

First, we can assume that all of our kinetic parameters are positive. Second, we will note that some of these kinetic parameters are decay rates for species with high affinities. Therefore we expect this to be small. For reference, see [24] in the case of Ras, [46] in the case of PTEN, and [59] in the case of formins. So we will assume  $k_{15} = 0$  and  $k_{16} = 0$ . Using algebraic manipulations, we arrive at these two sufficient conditions:

1. If

$$m_5 > \frac{k_6 (k_{13} m_4 + k_4 (2k_1 + k_{11}))}{k_4 k_{11}}$$

then, the coefficients i. -v. are negative.

2. if

$$k_{11} > k_1, \quad m_4 > -\frac{k_1 k_4 (k_1 + k_{11})}{2 (k_1 - k_{11}) k_{13}}, \quad \text{and}$$

$$m_5 > -\frac{3k_6 ((2k_1 + k_{11}) k_{13} m_4 + k_1 k_4 (k_1 + k_{11}))}{2 (k_1 - k_{11}) k_{13} m_4 + k_1 k_4 (k_1 + k_{11})},$$

then, the coefficient vi. is negative.

We estimate some parameters based on current literature (see Table 3.4). Then, we perform a bifurcation analysis on the steady state of the concentration of PIP3 (see Figure 3.15). Finally, we estimate the rest of the parameters based on the trajectories of distinct initial conditions representative of actin wave patterns (see Figure 3.14).

As predicted by our analysis, we see that multiple equilibria do not exist below a threshold of the feedback rate  $m_5$ .

## 3.5 Discussion

Actin waves are an active area of research, and questions such as, what are the necessary mechanisms required for membrane patterning? What is a minimal mechanistic model that produces actin waves? Where does an actin wave emerge? To name a few, remain unresolved. Our work addressed essential and dispensable mechanisms from a multiple steady-state dynamical system perspective. In addition, we identified possible routes of wave disruption, which is of experimental relevance. Finally, although we used the model eukaryote *Dictyostelium discoideum*, the methods are general enough for other systems where multistationarity dynamical systems arise.

Previous work has addressed actin wave models in different capacities [12, 13, 14, 40]. Nevertheless, most actin wave models in the literature are qualitative, and the biological

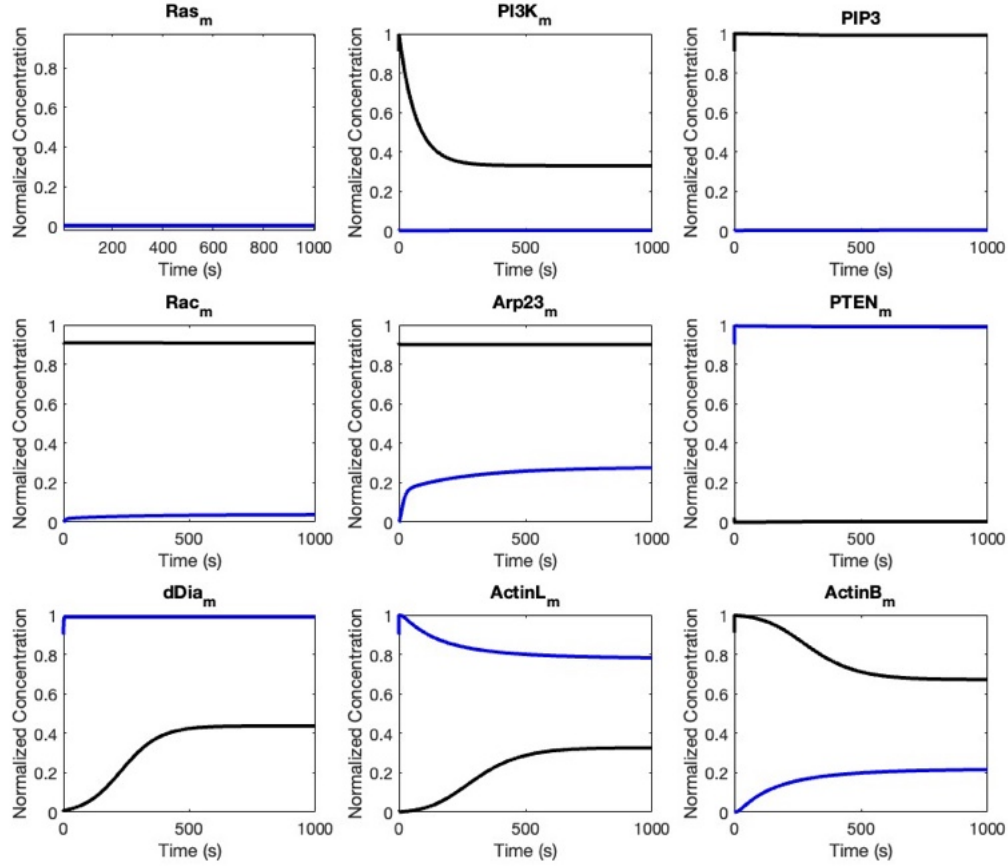


**Figure 3.14:** Trajectories of species starting from different initial conditions. Two trajectories are shown without introducing any perturbation. Blue shows a trajectory with a locally high concentration of PIP2 and its binding proteins. Black shows a trajectory with a locally high concentration of PIP3 and its downstream targets.

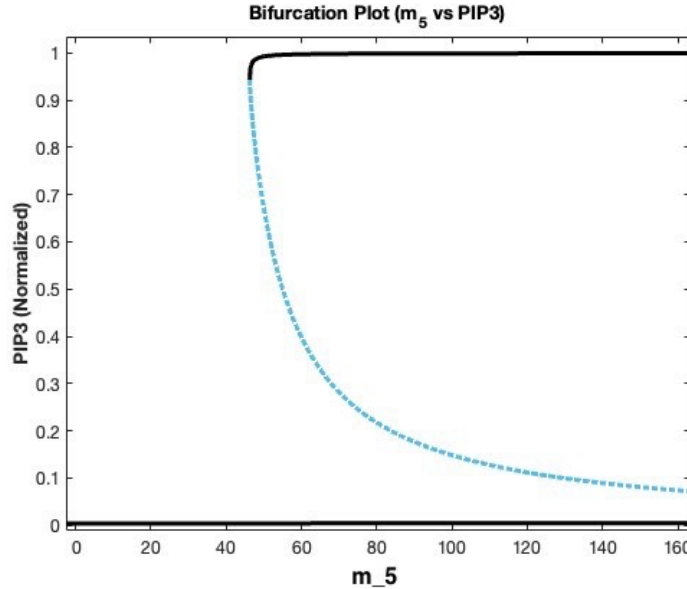


**Figure 3.15:** Bifurcation diagram for PIP3 against  $m_5$ . Solid lines indicate stable equilibria and dashed lines indicate unstable equilibria.

mechanisms are usually not in one-to-one correspondence with the underlying biology. Conversely, although true to biology, complex models leave a series of questionable assumptions in model parameters and the non-linearity of functions used. Take, for example, our previous work in [76]. In the mathematical model, waves arise from two converging pathways that operate at two different time scales (see Figure 3.16). The model successfully replicates wave patterns observed in macrophages. In particular, the simulations identified membrane receptors responsible for the initiation of a wave. However, the macrophage model fails to explain how robust the network architecture is. To be precise, we do not know if a subnetwork can display similar properties or if there are non-essential reactions in the system. Similarly, the choices of some parameters and non-linear feedback functions are subjective.

Our work here makes minimal assumptions on the model dynamics and provides information on the robustness with respect to reaction networks and parameter choices. More-

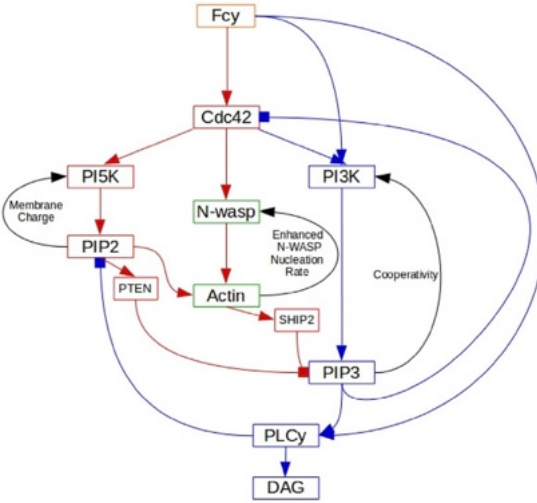


**Figure 3.16:** Biochemical pathways on macrophages. Taken from [76]

over, our method characterizes network architectures that preserve or disrupt bistability. With this, one could design experiments around candidate networks to identify minimal systems. Additionally, we have seen how our approach already explains several observations in the literature.

Trajectories in the local dynamics agree well with the literature (see Figures 3.17 and 3.18). A slightly different version of our model was inspected for global dynamics. In the spatio-temporal model, after the perturbation is introduced, we see PTEN decay and a biphasic PIP3 production, as reported in [62]. However, the lack of PIP3 decay at the center of the expanding wave does not appear in our simulations (see Figure 3.17). Additionally, if we are to take Arp2/3 as an indicator of downstream branched actin activity, our model appears to capture the ring-like structure seen in experimental data. We do not understand the emergence of these “ring” patterns, but we presume it has to do with downstream competition.

At the moment, our model could be elaborated at the downstream steps. We left actin dynamics out of the picture to have a more tractable system and one that is less computation-

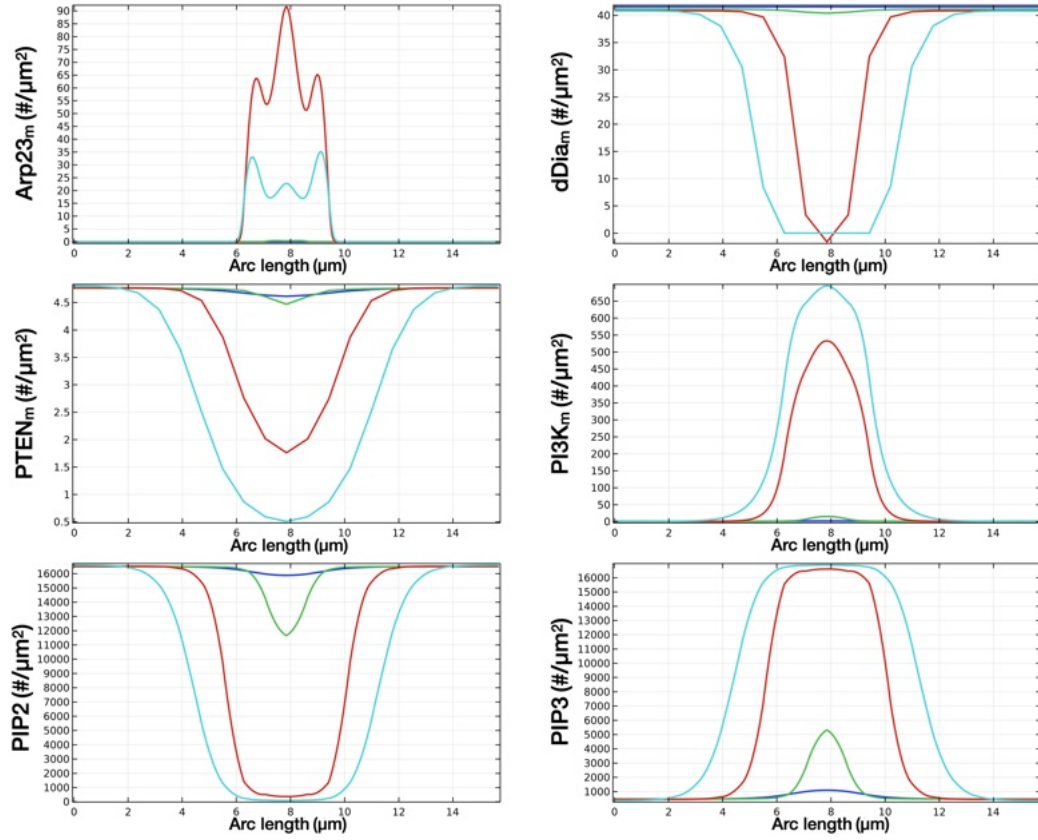


**Figure 3.17:** Global dynamics of species in the model for a sustained perturbation. Color legends: blue  $t = 20s$ , green  $t = 30s$ , red  $t = 40s$ , cyan  $t = 50s$ .

ally expensive. Given the results we obtained, in particular, that downstream competition is sufficient for multistationarity, the model could be improved by adding the actin dynamics step. Another place to improve could be in the parameter fit. We used the newton polytope technique to identify possible candidates, but we are yet to verify that these are biologically realistic. Another approach employs sensitivity analysis to identify critical parameters that account for most of the variance in a prescribed, scalar-valued function. We attempted such an approach using Sobol indices [86] (see Appendix A). However, the choice of a scalar-valued function that captures the spatio-temporal dynamics is non-trivial, and the simulations are computationally prohibitive.

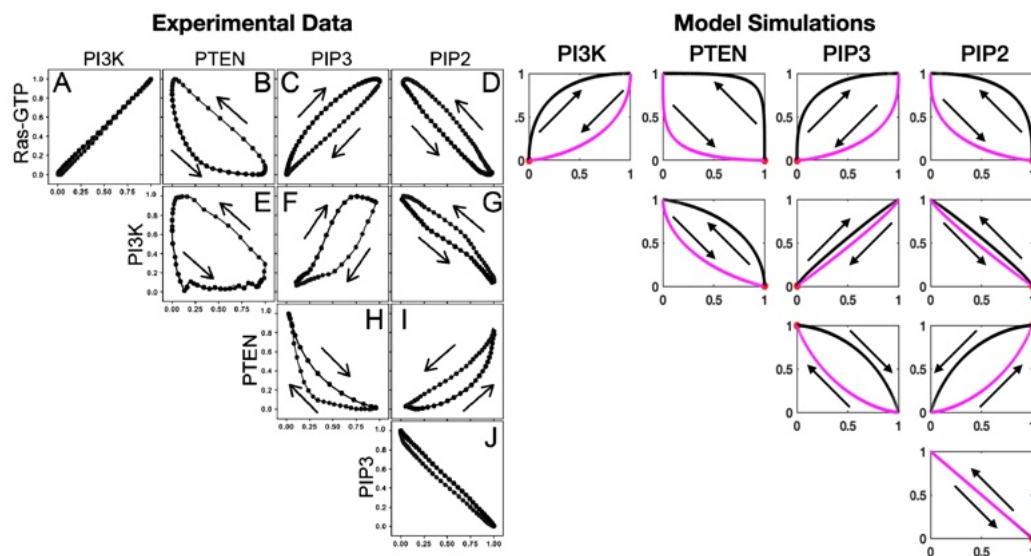


**Figure 3.18:** Normalized trajectories of the network under a perturbation. Left, experimental results from [14]. Right, mathematical model simulations.

## Chapter 4

---

### *Filopodia-like Structures in Dictyostelium*

#### 4.1 Introduction

Filopodia are long, relatively thin protrusions that typically extend perpendicular to the membrane of a cell. These structures are present in many organisms. For instance, filopodia emerge in the social amoeba *Dictyostelium discoideum*, yeast, neurons, fibroblasts, melanoma cells, and epithelial tissues (see Figure 4.1). The role of these thin protrusions is exploratory; it serves as a mechanism to sense local properties of the environment before committing resources and energy to migrate [87]. However, other speculative functions have emerged in recent years. For example, filopodia could have non-trivial roles in phagocytosis, and chemotaxis [88]. Noteworthy, the precise molecular sequence of events that lead to the emergence of a filopodium remains largely unknown. Although migration does not precede the emergence of a filopodium, the emergence rate positively correlates with the density of branched networks that characterize the front of a migrating cell (see Figure 4.1).

Some models have addressed the physical properties of filopodium, such as elongation, length, number of underlying filaments, and their buckling properties. However, more work is needed on protein localization and architecture within a filopodium. In particular, the biochemical pathways involved are unknown. This problem is partly challenging for the divergent signaling pathways driving the cytoskeleton regulation and their redundant role

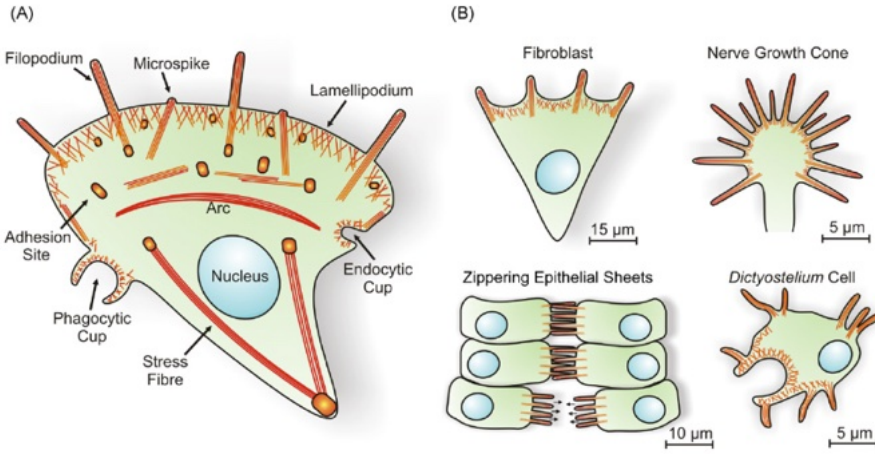


**Fig. 1.** Organization of cellular F-actin structures and filopodia in different cell types. (A) Overview of a schematized cell depicting distinct F-actin-containing structures. Microspikes and filopodia contain bundles of parallel actin filaments with the barbed ends facing towards the cell periphery. (B) Filopodia are found on the surfaces of different cell types. Despite considerable variation in overall cell morphology, the different cell types and/or tissues all express filopodia to various extents, the structural organization of which is highly conserved. The filopodia found in *Dictyostelium* cells appear more flexible as compared to most mammalian counterparts, which might be due to the absence of the actin-bundling protein fascin.

**Figure 4.1:** Different actin structures in a typical cell. Taken from [87]

in regulating migration modes. At any rate, properties of the extracellular matrix, such as stiffness, porosity, and geometry, are emerging as significant regulators, and only some quantitative results are at hand. Finally, the emergence mechanism that leads to a filopodium is unknown, but two influential hypotheses exist, convergent elongation and the *de novo* nucleation (see Figure 4.2).

On the one hand, the convergent elongation model speculates that filopodia emerge from filaments that merge at their barbed ends due to elongation factors. On the other hand, in the *de novo* nucleation model, filament nucleators cluster near the membrane and produce a nascent filament. The current understanding suggests that the mechanism employed depends on the cell type. Experiments in neurons favor the convergent mode [89], while others in *Dictyostelium discoideum* favor the *de novo* nucleation model [87].

In the next section, we will overview previous models that investigate the effect of mechanical feedback on filopodia-related processes. In particular, we will focus on curvature as a localization mechanism. Then, we use as a model basis the observations from Lee *et*

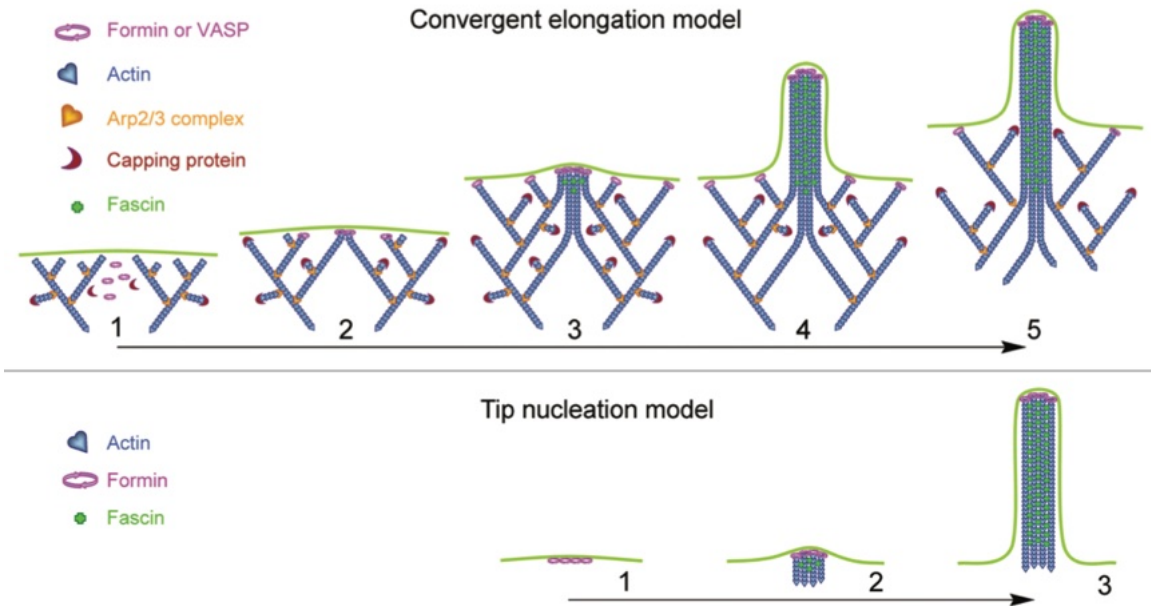


**Figure 4.2:** Different initiation models of filopodia. On the top, the convergent model where filaments converge together and facilitate the emergence of the tip. On the bottom, the nucleation model, where proteins localize at an initiation site preceding the emergence of a filopodia. Taken from [89].

*al.* [90] for an original theoretical framework that describes the localization of emerging filopodia. In the experiments of Lee *et al.*, the authors reproduced filopodia-like structures from a synthetic membrane and proposed a minimal set of molecular components. This minimal construction is an initial step to identify the essential proteins that regulate filopodia formation. Although the experiments focus on filopodia-like structures, the molecular set is present (up to homologs) in almost all model cells of interest. Thus, insights gained from our model are easily generalizable.

We use a hybrid model to capture distinct spatial scales and reduce computational costs where diffusion and membrane binding reactions are deterministic, while polymerization steps are stochastic. To our knowledge, a model that realistically incorporates the basic set of proteins and simulates filopodia-localization properties does not exist in the literature.

Quoting Faix et al., [87] "...is it possible to define a core, biochemical machinery responsible for filopodium initiation and protrusion, which functions in various cell types and is potentially engaged by divergent signaling pathways?".

## 4.2 Curvature Sensing and BAR Proteins

In the last decade, a growing body of literature has brought attention to understanding the role physical properties play in dictating the behavior of a cell model. How can a cell sense the properties of its environment? Furthermore, how can the same cell understand its properties and respond appropriately? The process of extracting physical properties from the environment is what we refer to as *mechanosensing*; the process of transforming this information into intracellular pathways is what we call *mechanotransduction*. For example, in certain types of cancer cells, the curvature can bias the phenotype of the system [91]. Similarly, substrate density and fluid pressure affect stem cell differentiation [92] and DNA synthesis [93]. Other examples of mechanosensing include immune responses, cell migration patterns, and phagocytosis [94]. As technologies evolve, a large body of data has given us insight into the possible pathways and molecular mechanisms at play. However, conclusions are far from being able to describe mechanical systems at the molecular level, and minimal systems found in the literature need more biological tractability.

We direct the reader to the following article by Trubeja and Bao for a broad review on mechanosensing [95]. Here onward, we will be focused on the role curvature has in facilitating filopodia hotspots near the membrane of a cell. Additionally, we explore how the input of the membrane's geometry influences the dynamics of the phosphoinositide-actin pathways. Our primary focus is eukaryotes, paying particular attention to mechanisms of Dicty. We start with an overview of known mechanisms in several systems at different

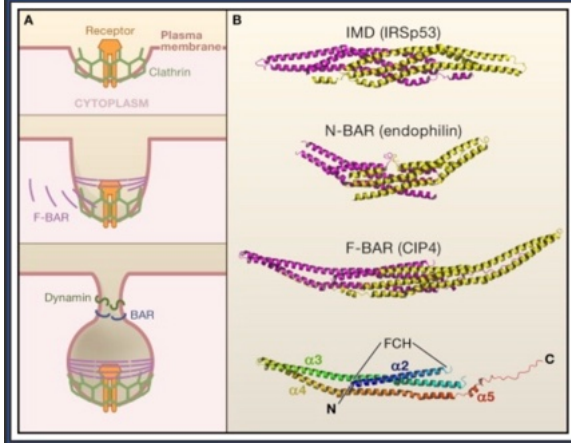


**Figure 4.3:** Curvature sensing via BAR domain proteins. Taken from [97].

scales. Then, we narrow our attention to the curvature-sensing BAR proteins and present some relevant mathematical models.

Remarkably, curvature sensing is a property seen at multiple length scales, where there is a specialized mechanism at each of them. In the smallest regime, local curvature has a 10–100 nm radius. Here, proteins in the Bin/Amphiphysin/Rvs (BAR) domain superfamily can attach to the curved membrane via anchor points attached to the side of their banana-shaped conformation (see Figure 4.3). BAR proteins can support the curved membrane, deform it, or recruit downstream effectors. In cell migration, the I-BAR domain protein IRS-p53 is associated with protrusions and can activate cdc42, formins, and the WAVE complex [96]. Septins and CIP4 localization correlate to lamellipodia and podosome regions around curved membranes in yeast. Similarly, in phagocytes, BAR proteins provide cells with a mechanism to stabilize the membrane during particle intake.

In the medium-length scale (microns), BAR proteins are not effective. Some theories propose that curvature, coupled with membrane tension, exerts forces against the cytoskeleton. These forces trigger pathways that regulate the cortex-membrane architecture, where specific configurations dictate the system's response. These properties include actin

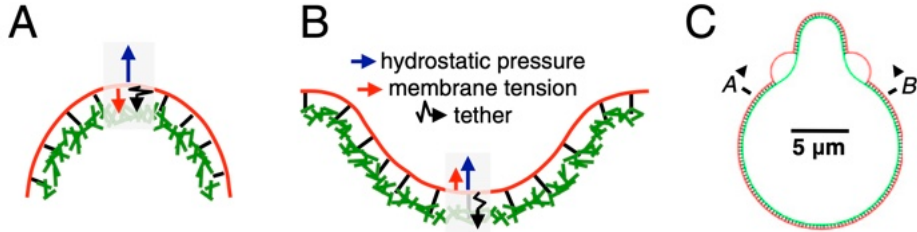


**Figure 4.4:** Physical model of blebbing due to curvature. A) and B) Forces acting on the membrane in positively- and negatively-curved regions, respectively. C) Blebbing typically appears at regions with negative curvature. Taken from [100]

network density, average filament orientation, and motor protein activity [98]. In *Dicystostelium discoideum*, for example, blebbing protrusions originate preferably from a negatively curved membrane region, whereas pseudopods originate at regions of positive curvature. In this model, a bleb occurs when the net outward force goes beyond an empirical threshold representing the severing of crosslinkers, allowing the membrane to detach from the cortex and extend outward [4.4] [99].

Lastly, curvature sensing is a multicellular phenomenon at the largest length scale. Cells confined to particular geometries show proliferation patterns that correlate with the environment's shape. For example, spherical or doughnut-shaped capsules in experiments with endothelial cells show increased proliferation in areas with high local mechanical stress associated with positive curvature. Similarly, local curvature correlates with an increase in the density of focal adhesions. For example, on square patterns, the emergence of adhesions is observed most prominently at the corners. The number and size of these adhesions precede an increase in actin stress fiber formation and traction forces [101]. In turn, stress fibers enhance actin turnover and thus polymerization by severing filaments away from the barbed ends [102].

Our main interest in this chapter is curvature sensing via BAR domain proteins, as filopodia initiation occurs in the sub-micrometer scale. Although the mechanisms of BAR

Classification	Protein	Preferred Lipid
BAR domain	Arfaptin1	Negatively charged lipid
	Arfaptin2	Negatively charged lipid
	PICK1	Negatively charged lipid
	APPL1, 2	PI(3,4,5)P3
	ASAP1	Negatively charged lipid
	SNX4,8,9,18	Negatively charged lipid
N-BAR domain	Amphiphysin1	PI(4,5)P2
	Amphiphysin2	PI(4,5)P2
	Endophilin	PI(4,5)P2
F-BAR domain	Toca1	PI(4,5)P2
	CIP4	PI(4,5)P2
	FBP17	PI(4,5)P2
	FCHo1,2	PI(4,5)P2
	PSTPIP1,2	PI(4,5)P2
	PACSIN-3	PI(4,5)P2
	Nostrin	PI(4,5)P2
I-BAR domain	IRSp53	PI(4,5)P2 (in filopodia) PI(3,4,5)P3 (in lamellipodia)
	MIM	Negatively charged lipid
	IRSTKS	Negatively charged lipid
	PinkBAR	Negatively charged lipid

**Table 4.1:** Lipid localization bias of the BAR superfamily proteins. Synthesized from Suetsgu *et al.* [103].

protein localization are not yet fully understood, we know that the membrane composition plays a significant role. Depending on the specific sub-family, BAR domain proteins have a bias to localize at PI(4,5)P2-or PI(3,4,5)P3-rich regions. On the one hand, BAR proteins use electrostatic interactions between the lipid-binding domains and the negatively charged lipids at the membrane. However, direct insertion into the membrane without specific binding domains is also possible [103]. It is yet unknown why one localization mode is used over the other. The group of Suetsgu *et al.* investigated localization patterns in the BAR domain superfamily; we synthesize their results in Table (4.1) [103] [104].

Downstream effectors of BAR proteins include scaffolding players that interact with

actin polymerases such as formins and nucleating promoting factors. For example, the budding yeast F-BAR domain protein Bzz1 binds yeast WASP. Analogously, mammalian F-BAR domain proteins Toca1 and FBP17 can stimulate actin filament assembly through N-WASP on curved membranes. Similarly, the mammalian endocytic BAR domain protein SNX9 directly binds N-WASP to stimulate actin filament assembly [104]. The I-BAR protein IRSp53 (insulin receptor substrate of 53 kDa) and lamellipodin (also known as Raph1) are of particular interest to us as they correlate to Ena/VASP clustering underneath filopodia structures. IRSp53 can interact with both PI(4,5)P<sub>2</sub> and PI(3,4,5)P<sub>3</sub>, as shown by Suetsugu *et al.* However, in filopodia, IRSp53 significantly prefers to localize around PI(4,5)P<sub>2</sub> [103]. These observations are supported by *in vitro* studies showing that IRSp53 recruits and clusters VASP to assemble actin filaments locally on PI(4,5)P<sub>2</sub>-rich membranes, leading to the generation of protrusions resembling filopodia [105]. Dicty contains a single gene encoding a protein similar to IRSp53 called IBARa. IBARa protein localizes at sites of negative curvature, with myosins (MyoB), and with a reciprocal drop in Arp2/3 accumulation [106].

Only a handful of theoretical models have used BAR domain proteins as a mechanism for curvature sensing. For example, in the model of Gov and Gopinathan (see 4.5), a Turing instability system is responsible for generating protrusions from fluctuations in the membrane. Slow membrane-bound proteins diffuse freely and enhance actin polymerization at areas of increased curvature. As a result, the membrane deforms in the normal direction and increases local curvature, feeding back into the localization of the BAR proteins. This positive feedback loop successfully generates a local protrusion. However, the system is only a two-species model, and the biochemical details are neglected, such as the actin polymerization pathways.

The model by Gov improved in a later article with the addition of myosin motor dynamics to simulate the effect of contractile forces. In this new model, protrusions can travel as

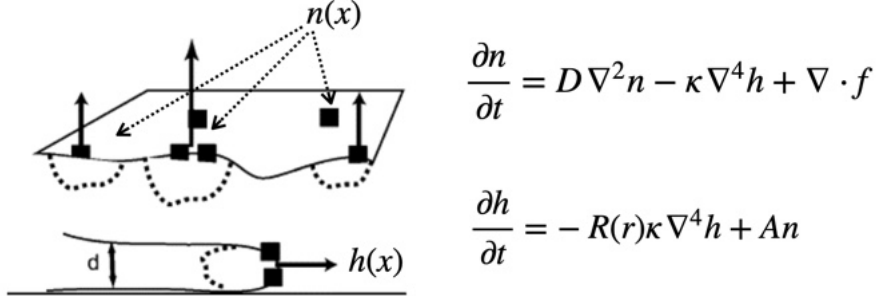


**Figure 4.5:** Turing model of Gov and Gopinathan. Taken from [107]

undamped waves along the one-dimensional membrane. The traveling wave is possible due to myosin creating dips of negative curvature along the leading edge of the wavefront. Actin filaments nucleate at these dips and recruit myosin, resulting in the lateral propagation of a protrusion [108]. We note that some authors challenge the role of curvature in these models. The alternative view suggests that protrusions result from membrane disconnection of the cortex from the membrane, followed by membrane expansion, driven by intracellular flow. Protrusion ceases when the underlying actin network recovers around the emerging projection. Kuusela and Alt, for example, simulated lamella dynamics by coupling cytoskeleton and substrate stresses via adhesion sites in the plasma membrane. This model, however, neglects all the biochemical pathways involved in actin dynamics [109].

Although we do not discuss focal adhesions in detail, it is essential to point out their connection to curvature sensing. Focal adhesions respond to curvature change, and these responses precede changes in F-actin organization, increased levels of phosphorylated myosin, and localization of nuclear Lamin-A [100]. In addition, focal adhesions can signal downstream pathways that lead to RhoA, and ROCK activation via integrins, both of which correlate with contractility and rearward membrane flow (see Figure 4.6) [110]. To date, integrin homologs have not been identified in Dicty. However, the proteins SadA and SadB have a

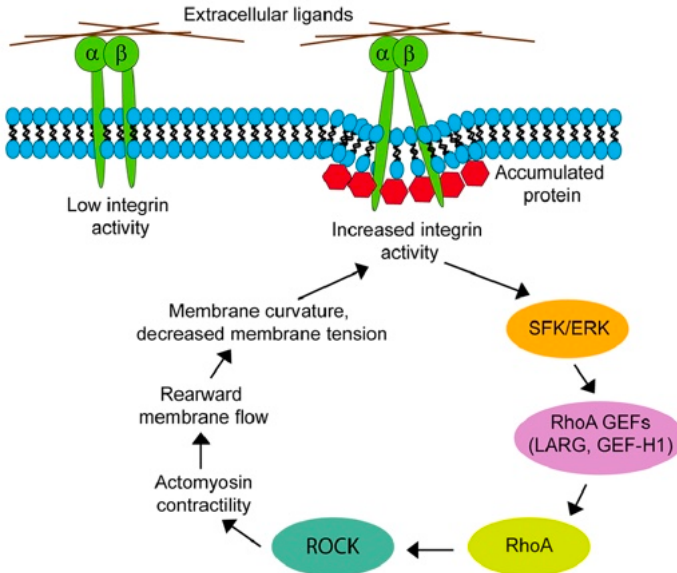


**Figure 4.6:** Role of integrins in mechanosensing. Taken from [110].

similar conformation, but their role in mechanosensing is still obscure [35].

### 4.3 Filopodia Initiation in Synthetic Bilipid Layers

In the textbook picture, a filopodium comprises a bundle of continuous actin filaments along the shaft (see Figure 4.7). Crosslinker proteins hold these filaments together, and the tips are bound to the membrane via formins. Although this picture is approximately correct, recent cryoelectron microscopy images challenge the view that filaments are continuous and devoid of Arp2/3, for example (see Figure 4.8). Moreover, to our interest, there is little information about the chronological sequence of events that lead to a filopodium.

Lee *et al.* experiments begin with a synthetic bilipid layer constructed from frog egg extracts [90]. In these experiments, purified versions of the molecular components lead to a defined temporal sequence of localization events that precede the formation of a filopodium-like structure. First, the F-BAR domain protein Toca-1 localizes at the membrane. The au-

#### 4.3. Filopodia Initiation in Synthetic Bilipid Layers

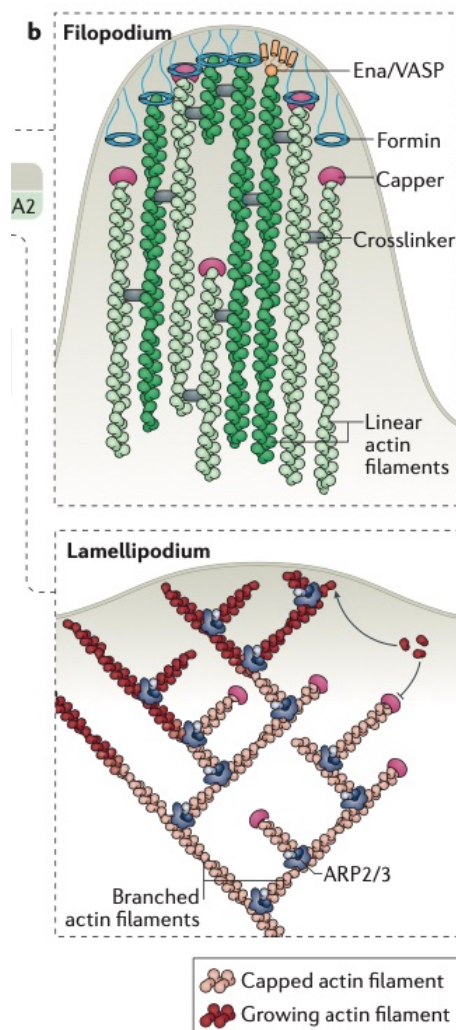


**Figure 4.7:** Typical structure of a filopodium. Taken from [56].

### 4.3. Filopodia Initiation in Synthetic Bilipid Layers

---

thors propose that localization occurs by a negatively charged membrane. Then, N-WASP is recruited and simultaneously localizes Arp2/3 complexes. The polymerization of filaments is observed shortly after due to Arp2/3 recruitment. After an initial burst in actin activity, formins and VASP localize to the tip of the growing filament and bundle together local filaments. The resulting bundles remain stable due to fascin, an actin-binding protein that cross-links filaments.

The underlying network's role is unclear from Lee *et al.* observations, which is true across the literature. However, a few knock-out experiments are at hand. For example, Arp2/3-null cells show no significant defects in the formation of parallel bundles, and experiments with *Dictyostelium Discoideum* cells lacking Nap1 (a WAVE binding protein of the WAVE regulatory complex) produce filopodia structures similar to those of WT cells [90]. These results suggest that WAVE, Arp2/3, and the underlying dendritic network are dispensable for filopodia formation. Nevertheless, there is not enough data to disregard the role of dendritic actin in other cell models such as neurons suggest [87, 111].

Other experiments hypothesized that membrane tension plays a significant role in filopodia initiation and elongation. Tension inhibits elongation by exerting force against a growing filament. Thus, any protrusion needs to overcome the membrane's resistance. The theoretical model of Atilgan investigates the expected number of filaments bundled together that are needed in order to overcome membrane forces [112]. In many experimental models, filopodia contain, on average, a dozen filaments [88]. However, as the filopodium grows, the filament bundles become more diversified and complex, which makes it hard to establish quantitative results. Images show that many filaments of varying lengths usually compose the body. On average, these filaments are 200nm long, but some are as long as 400nm [88].

Lastly, from experimental observations, there is not a clear indicator for the emergence of a filopodium. In most cases, however, the formation of parallel bundles near the mem-

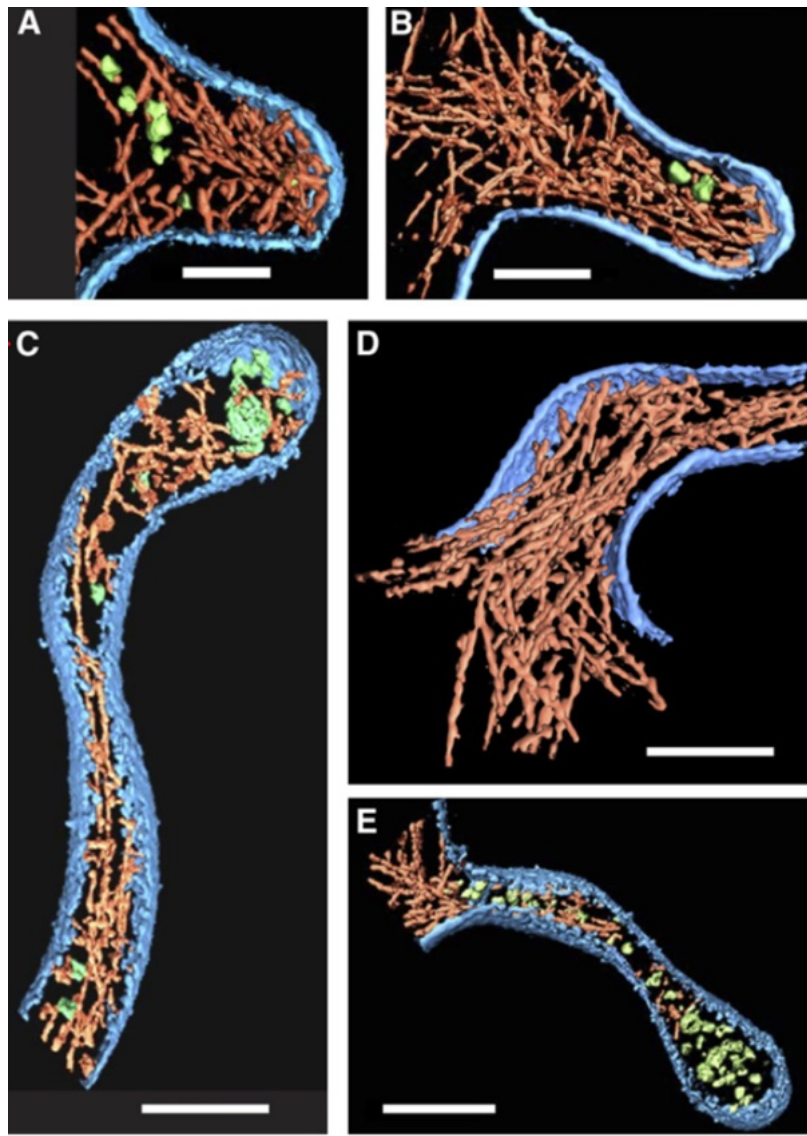


Figure 4.8: Cryo images of a filopodium. Taken from [88].

brane, followed by the assembly of a tethered tip, precedes the elongation step. The nascent tip is approximately 150 nm in length. At the base of an emerging filopodium, the filament bundles are connected to the underlying dendritic network if one is present.

In the case of Dia1 and Dia2 formins, which promote actin filament nucleation and polymerization, interactions with PI(4,5)P<sub>2</sub> appear to be important for their targeting to the

PI(4,5)P2-rich regions of the plasma membrane.

## 4.4 Mathematical Model

In this section, we develop the mathematical model of filopodial initiation that incorporates PIP2, PIP3, formins, actin-bundling proteins, filament capping proteins, Arp2/3, and actin, whose involvement in initiation is well-established in the literature. Our objective is to develop a model that replicates the experimental results seen in frog egg extracts [90], which we use to make theoretical predictions concerning how other experimentally-uncontrolled factors may influence results. In particular, we investigate the possible role of membrane curvature in the localization of formins. The theoretical predictions suggest a mechanism for filopodium initiation hotspots, where filaments are likely to converge.

The biochemical reactions incorporated are a simplified model of the network shown in Figure 4.9. For simplicity, we have chosen not to consider mechanochemical pathways present in wild-type cells. The implementation of our numerical method has not been optimized and even these simulations that exclude membrane coupling take a significant amount of time. Nevertheless, similar simplifications have yielded useful insights in other models, as is the case of Schaus *et al.* [113]. Note, however, that adhesion to a substrate is an important factor in filopodia initiation, as we know that *phg2* mutants in Dicty express fewer protrusions [114]. Nevertheless, the mechanisms of mechanotransduction remain debatable. In the case of adhesion, for example, we know that cells in suspension can express filopodia without activating adhesion pathways [115].

We hypothesize that the following pathway leads to the emergence of a filopodium. First, a PIP3-rich membrane promotes the activation of Rac1 by localization of its GEF. As a result, Rac1 activates the WAVE-Arp23 pathway, which maintains a network of branched

filaments near the membrane. The branching network is maintained by treadmilling, which involves the decay of filaments due to basal depolymerization rates, stochastic inhibition of polymerization via capping proteins, and polymerization regulation from WAVE and WASP [56].

To stimulate the localization of linear polymerases, we introduce a change in membrane lipid composition. Specifically, we change a PIP3-rich region (depleted of PI(4,5)P2 to a PIP(4,5)P2-enriched one (depleted of PIP3). Stochastic changes in the membrane polarity or the basal activity of a phosphatase such as PTEN can support a biophysical basis of this type of perturbation. This change in membrane composition, coupled with membrane curvature, allows curvature-sensing proteins to bind to the membrane. We know that PI(4,5)P2 interacts directly with the membrane curvature sensing BAR and F- BAR domain proteins through their banana-shaped domains [104]. The localization of BAR proteins facilitates formin activity and VASP localization in PI(4,5)P2 regions. At the same time, the increased density of PI(4,5)P2 suppresses the activation of Rac1 by activating its GAP.

Additionally, we assume that actin-bundling proteins localize at PI(4,5)P2 regions independent of BAR proteins. The mechanisms of ABP localization are unknown. Nonetheless, experiments show ABP protein localization in frog egg extracts only after PI(4,5)P2 patterns emerge [90]. Active formins at the membrane liberate capped filament ends due to their anti-capping properties, and ABP proteins stabilize filopodia by bringing filaments together. Formins further promote elongation by fast polymerization, primarily by incorporating ATP/ADP-Pi actin monomers (see Figure 2.8).

Our model is a hybrid of a deterministic and a stochastic model. First, we compute the steady concentration of proteins involved in the cytosol and the membrane in the deterministic step. Next, we use the deterministic step's output as the initial condition for the stochastic component, where a sample of filaments evolves according to the local concentra-

tion of proteins. Finally, we compute the evolution of filaments with a fixed and sufficiently small time step using a  $\tau$ -leaping method over each of the sampled filaments. Note that the local protein concentrations are held constant throughout the stochastic routine. We assume that, locally, the membrane's composition changes slowly compared to the dynamics of the chemical reactions. Our results shed light on the possible role of curvature as a mechanism for filopodia initiation and the role formins and Arp2/3 concentrations have in the process.

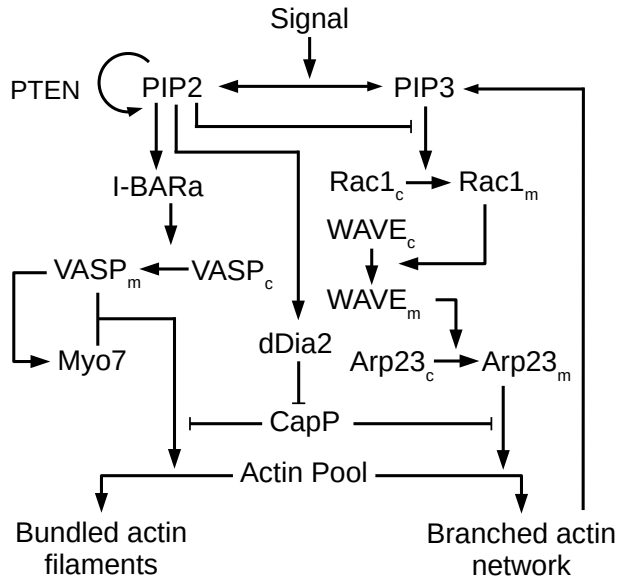


**Figure 4.9:** Diagram of the biochemical pathways leading to actin dynamics.

## Methods

We include a depiction of the model geometry in Figure 4.10. We begin by describing the deterministic part of the hybrid model where we distinguish two domains, the cytosol ( $\Omega_c$ ) and the membrane ( $\Omega_m$ ). The cytosol consists of a two-dimensional rectangular domain, whereas the membrane is considered a one-dimensional linear segment. In the cytosol, we impose periodic conditions on the left and right boundary ( $\Omega_{per}$ ), a Dirichlet boundary condition on the lower bound ( $\Omega_D$ ), and a Neumann condition on the top boundary ( $\Omega_N$ )

which accounts for cytosol-membrane protein localization. Naturally, the membrane is also periodic from left to right. The shape of the membrane is a continuous function connecting the boundaries ( $\Omega_{per}$ ) at the upper limit point.

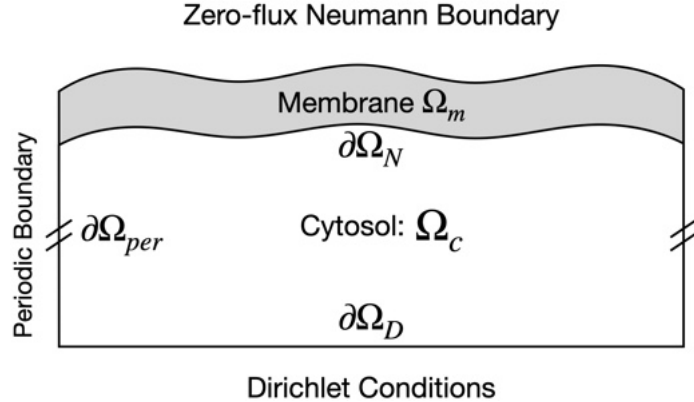


**Figure 4.10:** Geometry for the model.

As in previous sections, we will use the subscripts  $c$  and  $m$  to denote cytosolic and membrane-bound proteins, respectively. The governing equations of the deterministic part are

In the cytosol ( $\Omega_c$ ) we have:

$$\begin{aligned}\frac{\partial Actin_c}{\partial t} &= D_c \Delta Actin_c \\ \frac{\partial Formin_c}{\partial t} &= D_c \Delta Formin_c \\ \frac{\partial Arp23_c}{\partial t} &= D_c \Delta Arp23_c \\ \frac{\partial ABP_c}{\partial t} &= D_c \Delta ABP_c \\ \frac{\partial CapP_c}{\partial t} &= D_c \Delta CapP_c,\end{aligned}$$

together with boundary conditions

$$D_c \frac{\partial Formin_c}{\partial n} = -k_1 \ell h(\mathbf{k}) Formin_c PIP2 + k_2 Formin_m \in \partial\Omega_N$$

$$D_c \frac{\partial Arp23_c}{\partial n} = -k_3 \ell Arp23_c PIP3 + k_4 Arp23_m \in \partial \Omega_N$$

$$D_c \frac{\partial ABP_c}{\partial n} = -k_5 \ell ABP_c Form_m + k_6 ABP_m \in \partial \Omega_N.$$

In the functions above,  $h(\mathbf{k})$  is a feedback function that depends on local membrane curvature  $\mathbf{k}$ ,  $\ell$  is the membrane thickness, and  $\frac{\partial}{\partial n}$  is the normal outward derivative. For simplicity, we use a logistic function for  $h(\mathbf{k})$ , explicitly:

$$h(\mathbf{k}) = \frac{e^{\mathbf{k}}}{1 + e^{\mathbf{k}}}.$$

We compute the curvature of a function  $f$  at a point  $x$  with the concavity-signed Frenet formula. We use the sign of concavity to ensure that, in our particular setting, locally convex regions have negative feedback, whereas locally concave regions have positive feedback. For a continuous function  $f(x)$ , the signed curvature is given by:

$$\mathbf{k}(x) = -\text{Sign}[f''(x)] \frac{|f''(x)|}{(1 + [f'(x)]^2)^{3/2}} = \frac{-f''(x)}{(1 + [f'(x)]^2)^{3/2}}.$$

Note that the feedback goes from 0 to 1 and has a value equal to 0.5 when the curvature is 0. The choice of feedback function is rather empirical. For reference, the work of Tamemoto *et al.* uses a quadratic feedback function to estimate free energy as an integral around the membrane [116]. However, our work uses a local membrane region, so the global estimate is unavailable. In a different context, the effect of linear, exponential, and logistic curvature-related feedback functions on growing one-dimensional domains with Turing instabilities appears in earlier work by Madzvamuse [117]. As mentioned before, we use periodic and Dirichlet conditions at the lateral (left to right) and lower boundaries, respectively (see Figure 4.10). For the concentrations imposed at the lower boundary ( $\Omega_D$ ), refer to Table 4.2.

At the membrane ( $\Omega_m$ ) we have the following system of surface reactions

$$\frac{\partial Formin_m}{\partial t} = k_1 \ell h(\mathbf{k}) Formin_c PIP2 - k_2 Formin_m$$

$$\frac{\partial Arp23_m}{\partial t} = k_3 \ell Arp23_c PIP3 - k_4 Arp23_m$$

$$\frac{\partial ABP_m}{\partial t} = k_5 \ell ABP_c Form_m - k_6 ABP_m$$

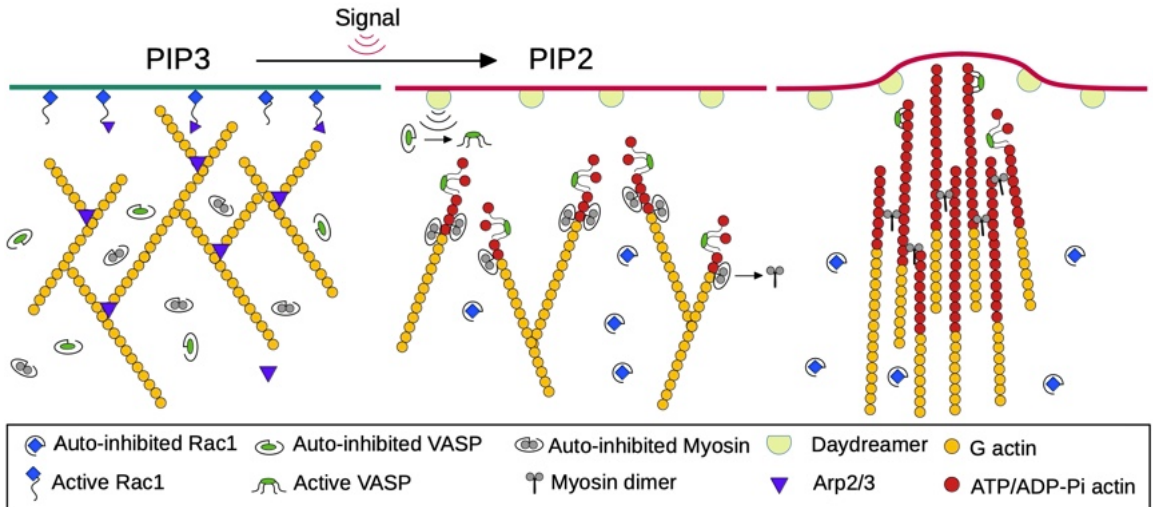


**Figure 4.11:** Diagram of hypothetical mechanism of filopodia initiation.

We solve the steady-state concentration profiles of the membrane system. First, we set all membrane species to 0 and the cytosolic species equal to the Dirichlet boundary concentration for initial conditions. Then, we evolve the system using COMSOL. After convergence, we use the steady-state concentrations as input into the stochastic model. Although the deterministic and stochastic models are “decoupled” from each other, membrane localization at this spatial scale may occur faster than filament dynamics. Therefore, it is relevant to explore this assumption.

The stochastic step of the model occurs as follows. First, we sample a set of actin filaments using the method described in the work of Schaus *et al.* [113]. Each filament has a length equal to  $1\mu m$  and an orientation sampled from a normal distribution with a mean equal to 55 degrees and variance equal to 7 degrees. Here, we measure a filament’s orientation as the angle with respect to the horizontal axis. At each time step, the filaments present

in the simulation evolve according to the local protein concentrations in parallel. For each filament, if its barbed end is close to the membrane ( $< \ell$ ), we use the protein concentrations from the membrane compartment; otherwise, we use the values from the cytosol.

Similar to the work of Schaus *et al.* ([113]), rate transitions depend on the underlying, local, mass-action kinetic system  $\mathbf{x}'$ . We model the probability of an event occurring at a given time step and a given filament compartment (barbed end, pointed end, and filament body) as a Poisson process with a rate proportional to  $\Delta t \mathbf{x}'$ . With  $\Delta t$  being the size of the time step and  $\mathbf{x}'$  the corresponding mass-action kinetic system. Then, if an event takes place, its trajectory follows a Markov process based on diagrams **A**, **B**, and **C**, shown in Figure 4.12. The method is equivalent to the Gillespie algorithm ([118]). At the end of every time step, each filament length evolves deterministically based on the state of its respective endpoints. Filament polymerization can occur at a basal rate or be mediated by formins or Arp2/3. Our model assumes that polymerization rates are faster for filaments bound to formins than those bound to Arp2/3 (see Table 4.2). For those filaments that are attached to a bundling protein, their center of mass moves discretely up the gradient of the highest APB concentration. At the end of the filament length evolution, we update the time step, and the routine starts anew until we reach a prescribed end time.

## 4.5 Results

### 4.5.1 Flat Membrane with a Prescribed Phosphoinositide Pattern

In the experiments done by Lee *et al.*, [90], a glass surface supports a flat membrane. Once the purified proteins are added to the mixture, phosphoinositide patterns emerge spontaneously. Thus, we begin with a simulated flat membrane where we prescribe PIP2 and PIP3 patterns a priori (Figure 4.15 top). In our model, an analogous procedure reproduces

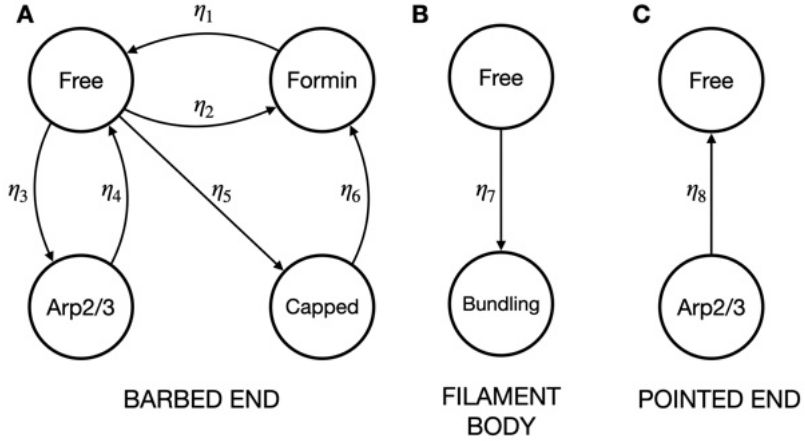


**Figure 4.12:** Markov chains for the filopodia model. A) State transitions at the barbed end. B) State transition along the filament’s body. C) State transition at the pointed end.

some observations in the literature. However, in these flat membrane simulations, we have omitted the fascin role and postponed its effect to curved membranes later. Furthermore, given that we have not endowed formins with a bundling mechanism, filament bundles will only appear in the presence of fascin.

Firstly, as noted in Schaus *et al.*, [113], branching actin networks self-organize, with nascent filaments orienting at  $55^\circ$  degrees relative to the leading edge. In agreement with the model of Schaus, our result suggests a similar self-orientating behavior. Filament orientations are independent of initial configurations and approximate a normal distribution with mean  $55^\circ$  (Figure 4.14).

Secondly, experimental observations suggest that Arp2/3 is dispensable for filopodia initiation [111]. In the standard picture, formins sequester filaments by binding to the barbed ends inhibiting Arp2/3, suggesting that Arp2/3 is unnecessary. However, our model shows that this is not the case. Instead, the Arp2/3 pathway might upregulate the frequency at which filopodia emerge. A secondary role of formins emerges in moderate concentrations of capping proteins ( $200 \text{ #}/\mu\text{m}^2$ ). In this regime, formins uncap filaments which serve as

## 4.5. Results

---

Description	Parameter	Value	Reference
<b>Filament binding Parameters</b>			
Forming unbinding	$\eta_1$	$1\#\text{s}^{-1}$	
Formin binding	$\eta_2$	$5\#\text{s}^{-1}$	
Arp2/3 binding rate	$\eta_3$	$1\#\text{s}^{-1}$	
Arp2/3 unbinding	$\eta_4$	$10\#\text{s}^{-1}$	
Capping	$\eta_5$	$1\#\text{s}^{-1}$	
Uncapping by formins	$\eta_6$	$1\#\text{s}^{-1}$	
Cross-linker binding	$\eta_7$	$10^{-1}\#\text{s}^{-1}$	
Filament debranching	$\eta_8$	$10^{-4}\#\text{s}^{-1}$	
<b>Membrane Binding Parameters</b>			
Formin on rate	$k_1$	$1.6 \times 10^{-10} \mu\text{m}^2\#\text{s}^{-1}$	
Formin off rate	$k_2$	$0.01\text{s}^{-1}$	
Arp2/3 on rate	$k_3$	$1.6 \times 10^{-10} \mu\text{m}^2\#\text{s}^{-1}$	
Arp2/3 off rate	$k_4$	$0.01\text{s}^{-1}$	
ABP on rate	$k_5$	$1.6 \times 10^{-8} \mu\text{m}^2\#\text{s}^{-1}$	
ABP off rate	$k_6$	$1 \times 10^{-9}\text{s}^{-1}$	
<b>Polymerization rates</b>			
Basal polymerization	$\rho_1$	$0.01\mu\text{ms}^{-1}$	
Arp2/3 mediated	$\rho_1$	$0.2\mu\text{ms}^{-1}$	
Formin mediated	$\rho_1$	$0.4\mu\text{ms}^{-1}$	
Cytosol diffusion	$D_c$	$50\mu\text{m}^2\text{s}^{-1}$	Typical
Membrane layer	$\ell$	$0.01\mu\text{m}$	Typical
<b>Dirichlet Boundary</b>			
Actin concentration	—	$602\#\mu\text{m}^{-2}$	[119]
Arp2/3 concentration	—	$602\#\mu\text{m}^{-2}$	[119]
Formins concentration	—	$5\#\mu\text{m}^{-2}$	[119]
ABP concentration	—	$10\#\mu\text{m}^{-2}$	[119]
Capping protein concentration	—	$20\#\mu\text{m}^{-2}$	[119]
Actin monomer diameter	—	.004 $\mu\text{m}$	[113]

**Table 4.2:** Rate constants in the filopodia model

<sup>a</sup>Value is  $10^{-1}$  times that of reference

<sup>b</sup>Value is  $10^{-1}$  times that of reference

a substrate for the underlying branching network. With denser networks, the rate at which filaments converge increases, thus increasing the likelihood of a filopodium emerging. This result reconciles observations that filopodia often emerge from dense networks [89].

Lastly, our model reveals that the underlying network becomes denser at higher concentrations of formin activity (Figure 4.13). Indeed, by plotting the number of filaments in the network against time at different values of formin concentration, we observe that the number of filaments decays quickly to zero when formins are absent. This result is a consequence of capping proteins inhibiting the action of polymerization. Conversely, as formins saturate the membrane, we see a positive increase in filaments. The trend appears to saturate

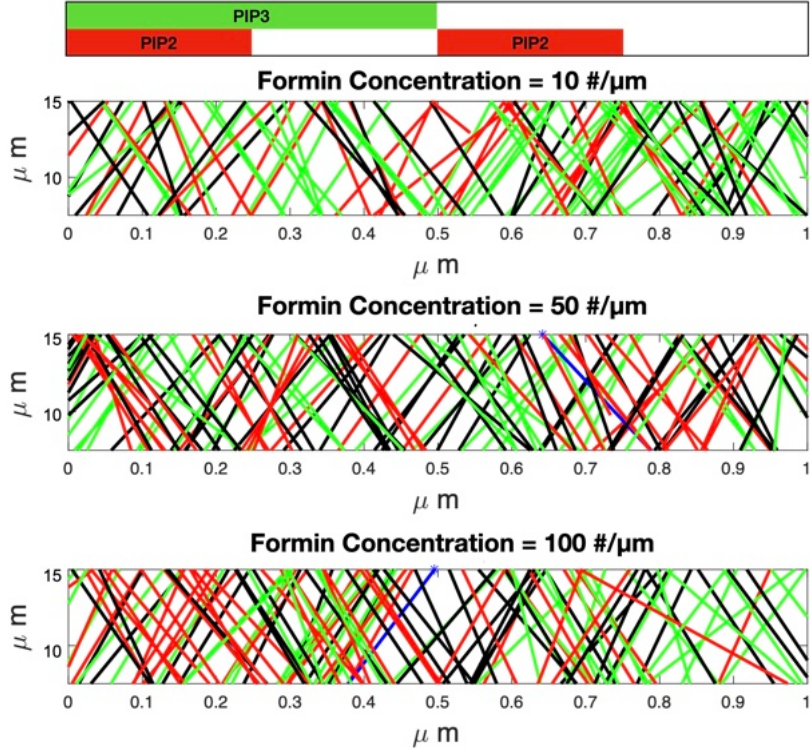


**Figure 4.13:** Network density at different formin concentrations. Top diagram indicates the spatial region where PIP3 and PIP2 is present. Filaments bound to formins at the membrane are colored red. Nucleating filaments from Arp2/3 are shown in blue. Capped filaments are colored green. Free filaments are shown as black.

at around a concentration of  $20 \#/\mu\text{m}$  (see Figure 4.16).

Currently, there isn't an understanding of how the balance of Arp2/3 and formin concentrations impedes or facilitates the emergence of a filopodium. We take a step in resolving this question and simulate a membrane with different protein domains. First, we simulate a membrane where WAVE localizes on the left part of the membrane. Then, PIP2 is enriched only at the first and third quarters of the membrane. This coating will facilitate the binding of Arp2/3 and formins at distinct regions in the membrane. The resulting steady-state for Arp2/3 and formin concentration at the membrane appears in Figures 4.15 and 4.13 (top). As expected, Arp2/3 binds to the membrane on the left side, while formins attach to the

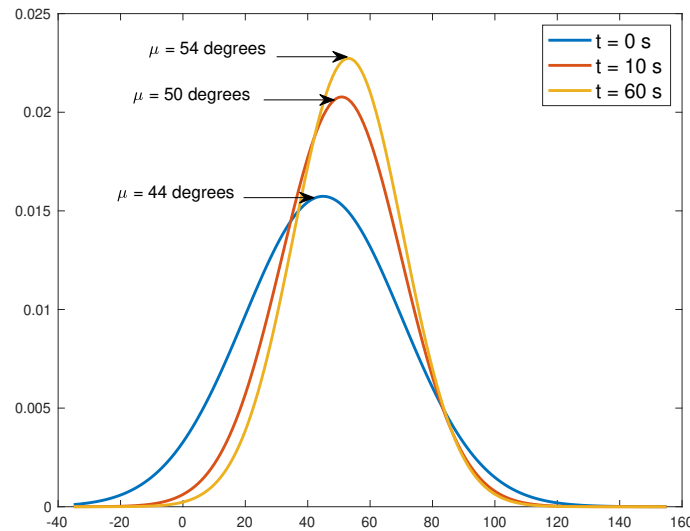


**Figure 4.14:** Distribution of filament orientations.

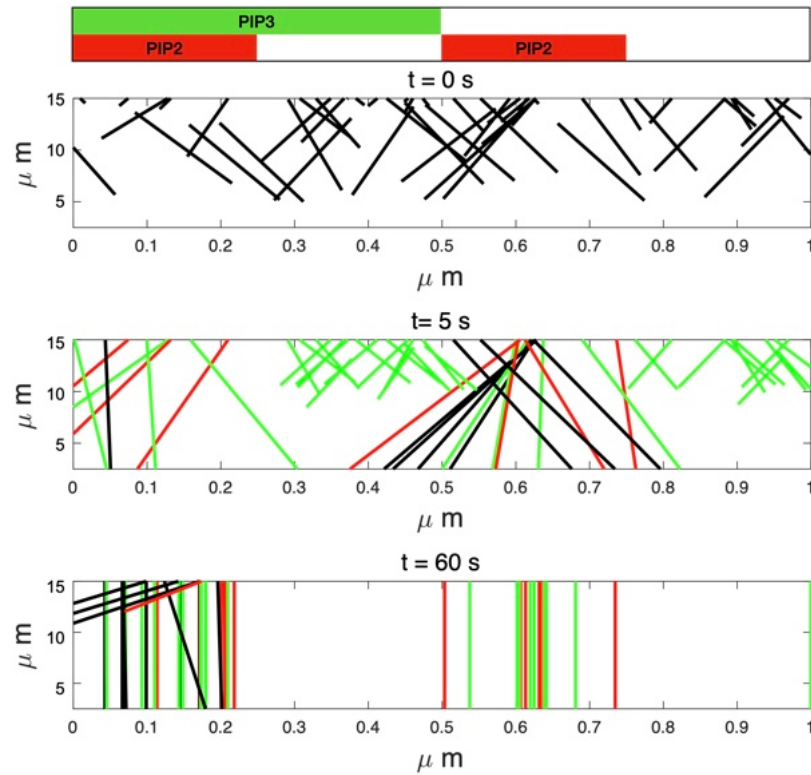


**Figure 4.15:** Filopodia simulation on a flat membrane. Filament color indicate protein bound at the barbed end: green for capping proteins, blue for Arp2/3, and red for formins.

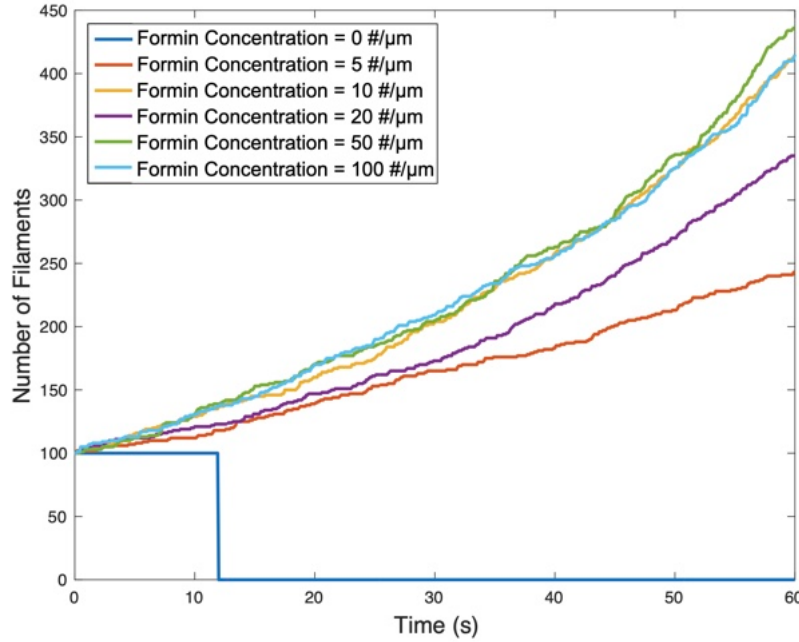


**Figure 4.16:** Number of filaments for varying concentrations of formins

PIP2 regions.

Our results suggest that Arp2/3 is not necessary to produce a filopodium as long as there is an existing substrate of filaments. Moreover, it is only at regions with active formins where a filopodium emerges. This result agrees with observations that filopodia tips are often enriched with processive polymerases like formins and ENA/VASP. Therefore, we hypothesize that the chance of a filopodium emerging increases as the local concentration of formins increases.

#### 4.5.2 Curvature as a Mechanism to Localize Formin Hotspots

In the previous section, we used a simulated phosphoinositide pattern to inspect the different roles of Arp2/3 and formins in filopodium initiation. The reasoning behind using prescribed patterns is that, just as in other phenomena like actin wave patterns, cytoskeleton effects precede membrane patterning. In this context, we want to understand better

how protein aggregate into “hotspots” that facilitate the emergence of filopodia. In other words, by a hotspot, we mean a rise in the concentration of molecular factors that favor an outcome—filopodia in the present. In addition, we investigate how the possible effect of membrane curvature in facilitating the binding of formins at the membrane. We use a membrane with homogeneous PIP<sub>2</sub> and PIP<sub>3</sub> concentrations in these simulations. We investigate three different cases: 1) a flat membrane, 2) a single, symmetric bump, and 3) a sinusoidal membrane with five local maxima (figures 4.17, 4.18, and 4.19).

In the first of these three cases, we observe that, in the absence of a phosphoinositide pattern and without feedback coming from curvature, Arp2/3 and formins localize uniformly across the membrane (Figure 4.17). This result is expected from the PDE formulation, serving as a control check for the simulation. Implementing the filament dynamics reveals no particular localization of filaments either. A simulation spanning 60 seconds results in a uniform localization of filaments near the membrane (see Figure 4.20 left). Although this does not imply that a filopodium can not emerge, we hypothesize it would occur less frequently due to the sparsity of the network.

In the second experiment, we used a membrane with a single bump. The localization of the proteins again results in a constant localization of Arp2/3 along the membrane. Nonetheless, formins concentrate on three key areas. First, as expected, formins localize at the protrusion tip due to curvature feedback. Additionally, two more hotspots of formin localization occur at sites where the membrane is flat. This localization is due to negative curvature having an antagonistic effect in formin localization (see Figure 4.18). This last result is interesting as it reveals an underlying role of negatively curved membranes. Finally, the simulation of filament dynamics supports the emergence of filopodium tips near the base of the protrusion and right behind the protruding membrane (see Figure 4.18 middle).

In the last simulation, we inspect a membrane with multiple protrusions. In this case,

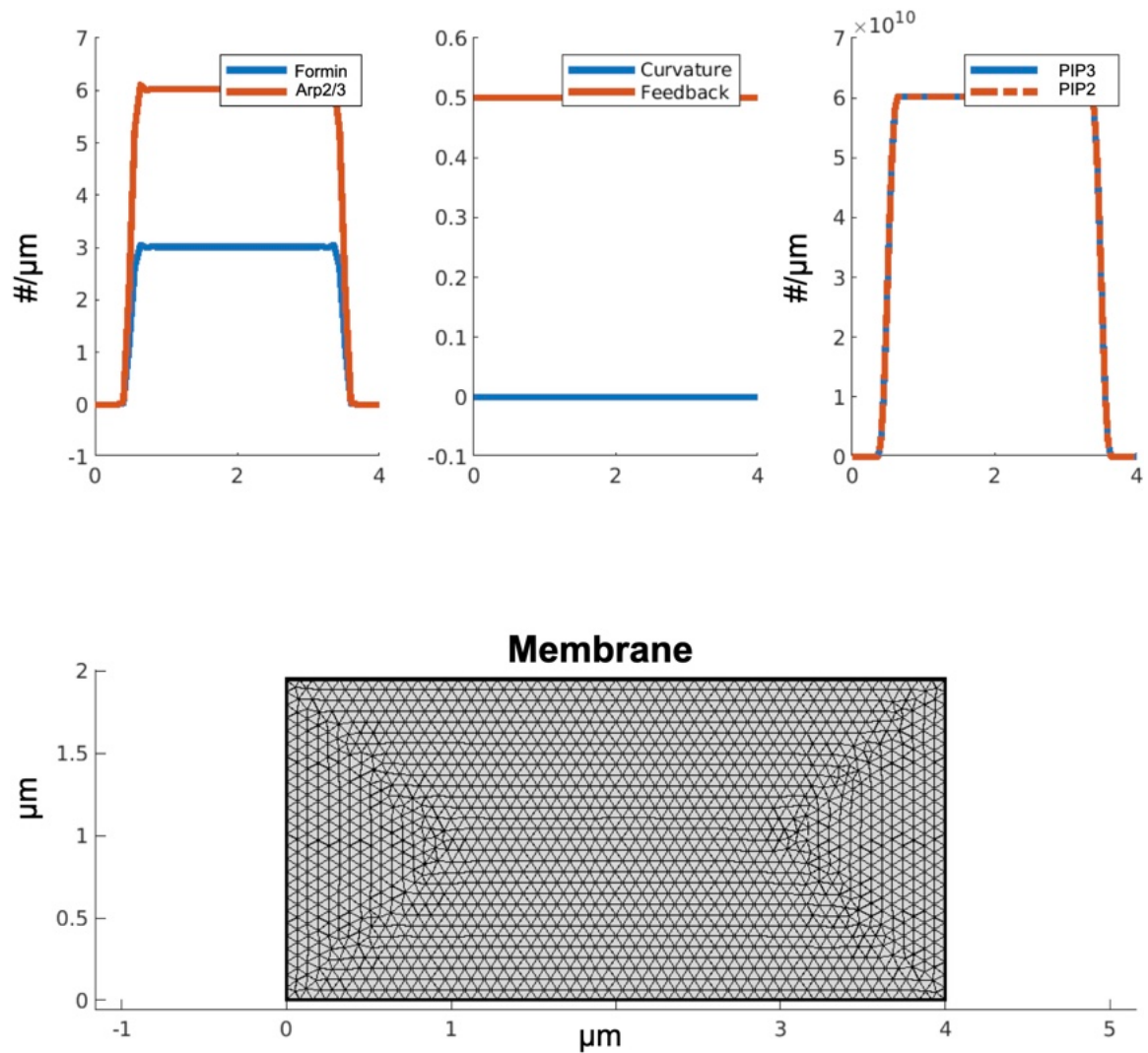


**Figure 4.17:** Protein distribution and curvature feedback for a flat membrane.

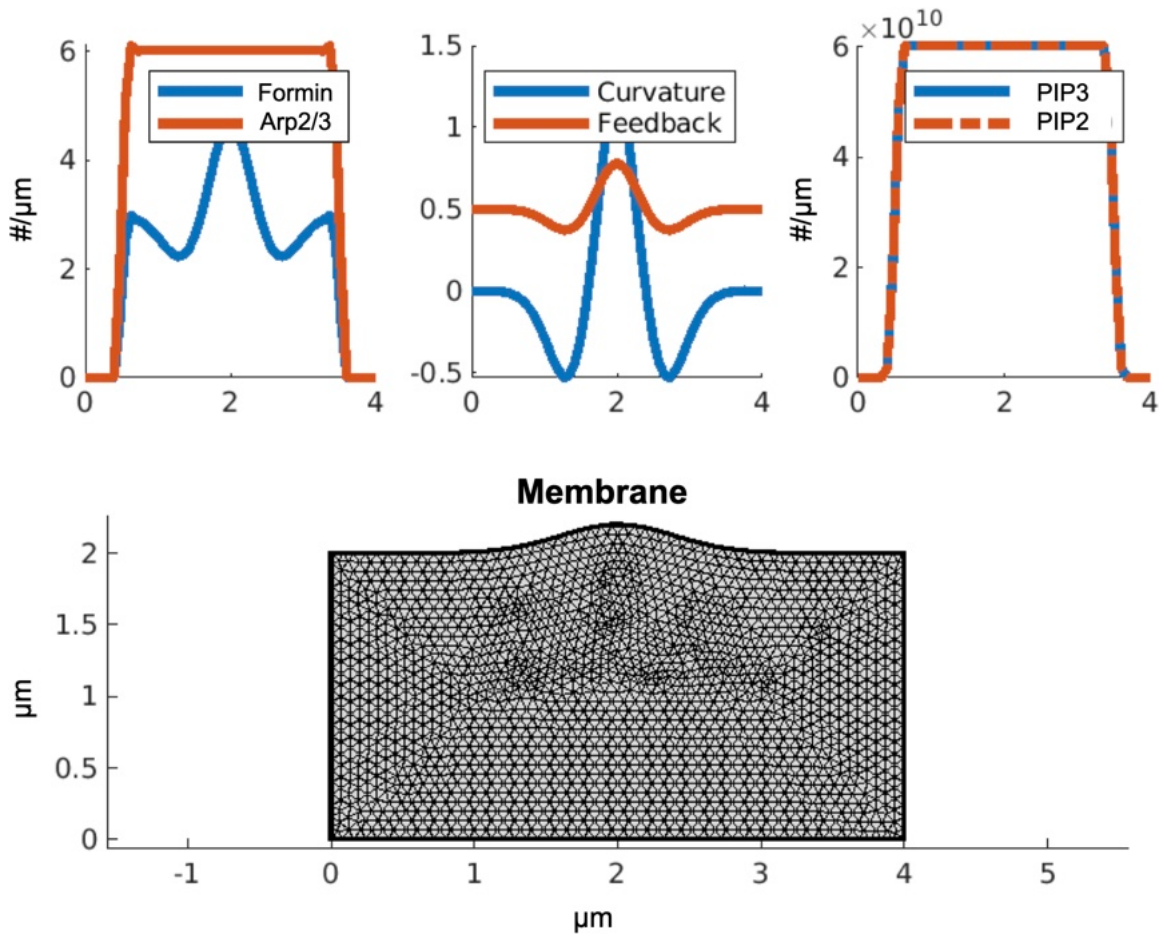


**Figure 4.18:** Protein distribution and curvature feedback for a membrane with one protrusion.

we modeled the membrane with a sinusoidal function having five maxima (see Figure 4.19). Similar to the previous experiment, formins localized at the protrusion front; however, we did not see lateral localization as we did in the single bump simulation due to the lack of an adjacent region of zero curvature (see Figure 4.20 right).

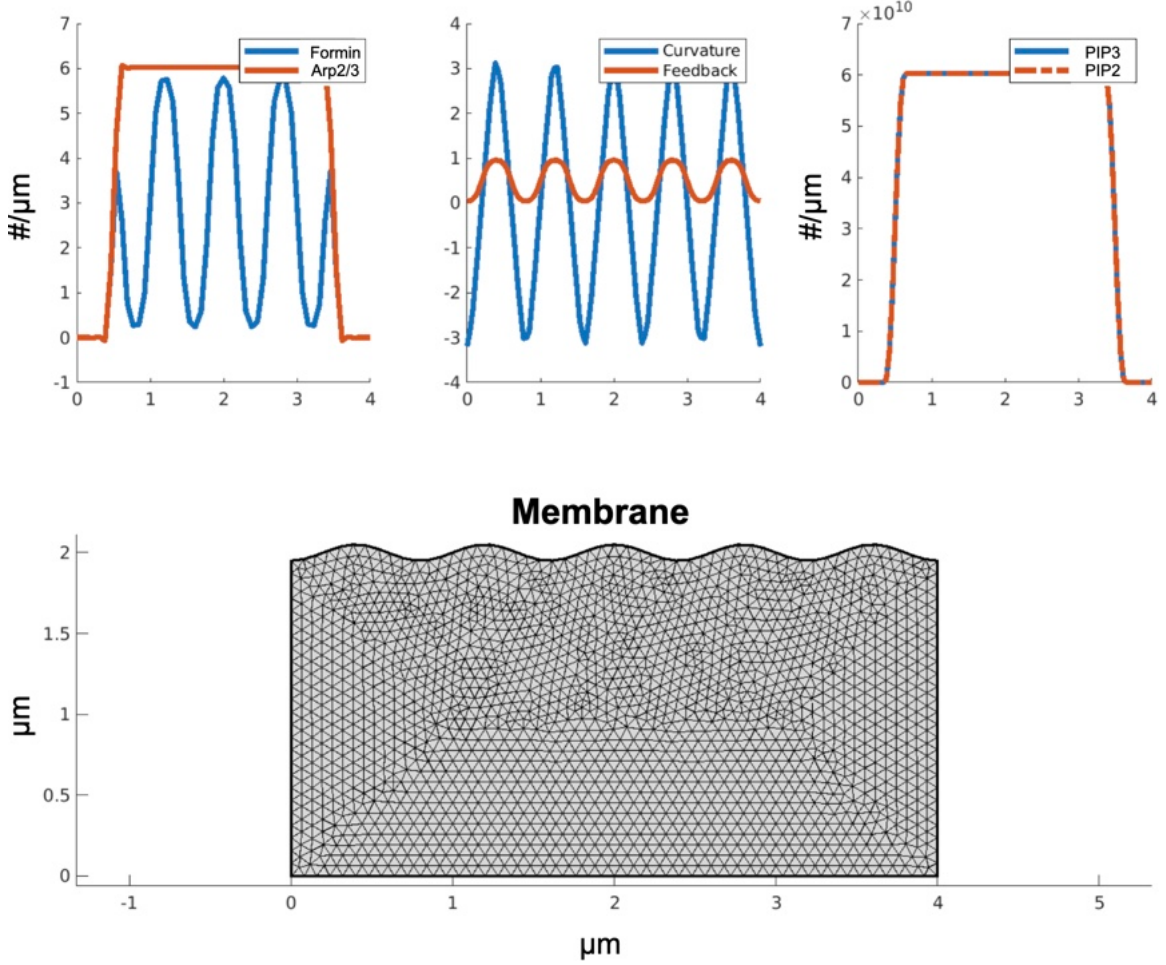


**Figure 4.19:** Protein distribution and curvature feedback for a membrane with five protrusions.

## 4.6 Discussion

Filopodia are structures that serve the cell in exploring its environment. Recent developments in cryo microscopy and fluorescence imaging have shed light on the composition and architecture of these protrusions [88]. However, the mechanisms that lead to filopodia are far more complex than initially thought, and no current model comprehensively integrates the seemingly divergent pathways of actin polymerization. There are many challenges, mainly if the aim is to remain faithful to biology while preserving tractability in

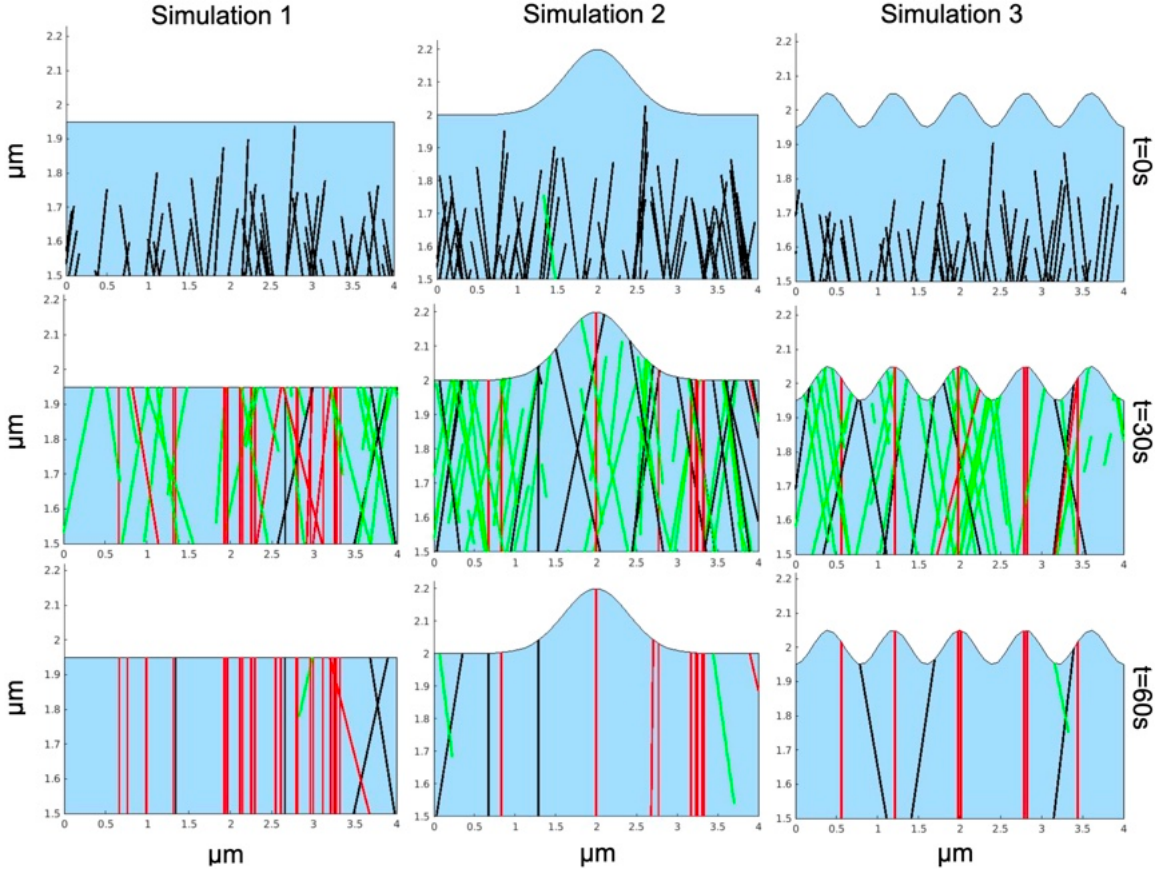


**Figure 4.20:** Effect of membrane curvature in filopodia initiation for different membranes.

mathematical models. Moreover, the role of mechanical input to organisms and precisely how these signals are integrated into the system are problems that remain highly obfuscated.

The earlier work by Schaus [113], and Atilgan [112] shed light on how mechanical properties such as elasticity and membrane fluctuations might influence the actin cytoskeleton dynamics. Nevertheless, the oversimplification of the underlying pathways obscures the role of actin-interacting proteins, such as formins, bundling proteins, and Arp2/3. Additionally, previous models have yet to address possible mechanisms of filopodia initiation, such as membrane curvature, which has gained recent attention [94]. At the time of this writing, we are not aware of other models of filopodia organization that inspect the initia-

tion due to the interplay between Arp2/3, formins, and membrane curvature. In this regard, our results are original and have yielded exciting results.

Our model has shown that curvature could facilitate hotspots of PIP2-enriched domains. These domains localize formins and myosin motors that bundle together filaments in the presence of a branched network. This mechanism could result from curvature sensing proteins, such as BAR and SH3 domain proteins [94]. The underlying branched network is not necessary to initiate a filopodium, but its presence, and density of filaments, facilitate initiation sites, as our simulations suggest. Thus, there is a natural balance between Arp2/3 and formins responsible for the rate at which a filopodium emerges. One could suggest an experiment with controlled ratios of the active form of these proteins in order to estimate its influence on the rate at which filopodia emerge, similarly to what was done by Lee *et al.* [90].

Our model has oversimplified the mechanics of the membrane in order to incorporate protein interactions without compromising the numerical methods. In this regard, our model could benefit from integrating elastic forces that act on the cytoskeleton. We have also left out the membrane shape dynamics for similar reasons, which is essential at later stages of the filopodium life cycle. The model could benefit as well from a dynamically coupled deterministic-stochastic step. Here, we decoupled such dynamics and opted for a two-step model. This consideration had to be taken due to the already slow computation times. However, it is an essential initial step in the direction of filopodia modeling. We hope that our model motivates experimentalists to investigate mechanosensing pathways in Dicty. As we mentioned earlier, no homologs of integrins have been found in Dicty, and the role of proteins with similar compositions remains obscure. Similarly, the function of BAR proteins in Dicty and their role in curvature sensing remains a mystery due to the complex processes that lead to their localization.

---

## Bibliography

- [1] Suzanne Macari, Lauren DiNicola, Finola Kane-Grade, Emily Prince, Angelina Vernetti, Kelly Powell, Scuddy Fontenelle IV, and Katarzyna Chawarska. Emotional expressivity in toddlers with autism spectrum disorder. *Journal of the American Academy of Child & Adolescent Psychiatry*, 57(11):828–836, 2018.
- [2] Anne J Ridley, Martin A Schwartz, Keith Burridge, Richard A Firtel, Mark H Ginsberg, Gary Borisy, J Thomas Parsons, and Alan Rick Horwitz. Cell migration: integrating signals from front to back. *Science*, 302(5651):1704–1709, 2003.
- [3] Andre Levchenko and Pablo A Iglesias. Models of eukaryotic gradient sensing: application to chemotaxis of amoebae and neutrophils. *Biophysical Journal*, 82(1):50–63, 2002.
- [4] Pablo A Iglesias. Chemoattractant signaling in *Dictyostelium*: adaptation and amplification. *Sci. Signal.*, 5(213):pe8–pe8, 2012.
- [5] Sudipto Das, Jack E Dixon, and Wonhwa Cho. Membrane-binding and activation mechanism of PTEN. *Proceedings of the National Academy of Sciences*, 100(13):7491–7496, 2003.
- [6] Carsten Beta. Bistability in the actin cortex. *PMC Biophysics*, 3(1):12, 2010.
- [7] M Bindschadler, EA Osborn, CF Dewey Jr, and JL McGrath. A mechanistic model of the actin cycle. *Biophysical Journal*, 86(5):2720–2739, 2004.
- [8] Till Bretschneider, Hans G Othmer, and Cornelis J Weijer. Progress and perspectives in signal transduction, actin dynamics, and movement at the cell and tissue level: lessons from *Dictyostelium*. *Interface Focus*, 6(5):20160047, 2016.
- [9] Jesus Lacal Romero, Zhouxin Shen, Kimberly Baumgardner, Jing Wei, Steven P Briggs, and Richard A Firtel. The *Dictyostelium* GSK3 kinase GlkA coordinates signal relay and chemotaxis in response to growth conditions. *Developmental Biology*, 435(1):56–72, 2018.
- [10] X Xu. Chemotaxis in the model organism *Dictyostelium discoideum* and human neutrophils. *Cell Dev Biol*, 5:e139, 2016.

- [11] Erik Bernitt, Hans-Günther Döbereiner, Nir S. Gov, and Arik Yochelis. Fronts and waves of actin polymerization in a bistability-based mechanism of circular dorsal ruffles. *Nature Communications*, 8:15863, Jun 2017.
- [12] Yoshiyuki Arai, Tatsuo Shibata, Satomi Matsuoka, Masayuki J Sato, Toshio Yanagida, and Masahiro Ueda. Self-organization of the phosphatidylinositol lipids signaling system for random cell migration. *Proceedings of the National Academy of Sciences*, 107(27):12399–12404, 2010.
- [13] Seiya Fukushima, Satomi Matsuoka, and Masahiro Ueda. Excitable dynamics of Ras triggers self-organized PIP3 signaling for spontaneous cell migration. *bioRxiv*, page 356105, 2018.
- [14] Seiya Fukushima, Satomi Matsuoka, and Masahiro Ueda. Excitable dynamics of Ras triggers spontaneous symmetry breaking of PIP3 signaling in motile cells. *J Cell Sci*, 132(5):jcs224121, 2019.
- [15] Mi-Rae Lee and Taeck J Jeon. Cell migration: regulation of cytoskeleton by Rap1 in *Dictyostelium discoideum*. *Journal of Microbiology*, 50(4):555–561, 2012.
- [16] PB Monk and HG Othmer. Wave propagation in aggregation fields of the cellular slime mould *Dictyostelium discoideum*. *Proceedings of the Royal Society of London. B. Biological Sciences*, 240(1299):555–589, 1990.
- [17] Yasuo Maeda and Junji Chida. Control of cell differentiation by mitochondria, typically evidenced in *Dictyostelium* development. *Biomolecules*, 2013.
- [18] Joe Dan Dunn, Cristina Bosmani, Caroline Barisch, Lyudmil Raykov, Louise H Lefrançois, Elena Cardenal-Muñoz, Ana Teresa López-Jiménez, and Thierry Soldati. Eat prey, live: *Dictyostelium discoideum* as a model for cell-autonomous defenses. *Frontiers in Immunology*, 8:1906, 2018.
- [19] Yougan Cheng, Bryan Felix, and Hans G Othmer. The roles of signaling in cytoskeletal changes, random movement, direction-sensing and polarization of eukaryotic cells. *Cells*, 9(6):1437, 2020.
- [20] Nathan S Alexander, Anita M Preninger, Ali I Kaya, Richard A Stein, Heidi E Hamm, and Jens Meiler. Energetic analysis of the rhodopsin–G-protein complex links the a-5 helix to GDP release. *Nature Structural & Molecular Biology*, 21(1):56–63, Dec 2013.
- [21] Carol L Manahan, Pablo A Iglesias, Yu Long, and Peter N Devreotes. Chemoattractant signaling in *Dictyostelium discoideum*. *Annu. Rev. Cell Dev. Biol.*, 20:223–253, 2004.

- 
- [22] Yuanhua Tang and Hans G Othmer. AG protein-based model of adaptation in *Dictyostelium discoideum*. *Mathematical Biosciences*, 120(1):25–76, 1994.
  - [23] Jean-Louis Martiel and Albert Goldbeter. A model based on receptor desensitization for cyclic AMP signaling in *Dictyostelium* cells. *Biophysical Journal*, 52(5):807–828, 1987.
  - [24] Yougan Cheng and Hans Othmer. A model for direction sensing in *Dictyostelium discoideum*: Ras activity and symmetry breaking driven by a  $G\beta\gamma$ -mediated,  $G\alpha 2$ -Ric8-dependent signal transduction network. *PLoS Computational Biology*, 12(5):e1004900, 2016.
  - [25] Oliver Hoeller, Jared E Toettcher, Huaqing Cai, Yaohui Sun, Chuan-Hsiang Huang, Mariel Freyre, Min Zhao, Peter N Devreotes, and Orion D Weiner.  $G\beta$  regulates coupling between actin oscillators for cell polarity and directional migration. *PLoS Biology*, 14(2), 2016.
  - [26] T Höfer, PK Maini, Jonathan Adam Sherratt, MAJ Chaplain, P Chauvet, D Metevier, PC Montes, and JD Murray. A resolution of the chemotactic wave paradox. *Applied Mathematics Letters*, 7(2):1–5, 1994.
  - [27] Hans G. Othmer, Peter B. Monk, and Paul E. Rapp. A model for signal-relay adaptation in *Dictyostelium discoideum*. II. Analytical and numerical results. *Mathematical Biosciences*, 77(1):79 – 139, 1985.
  - [28] Yuanhua Tang and Hans G Othmer. Excitation, oscillations and wave propagation in a G-protein-based model of signal transduction in *Dictyostelium discoideum*. *Philosophical Transactions of the Royal Society of London. Series B: Biological Sciences*, 349(1328):179–195, 1995.
  - [29] John C Dallon and Hans G Othmer. A discrete cell model with adaptive signalling for aggregation of *Dictyostelium discoideum*. *Philosophical Transactions of the Royal Society of London. Series B: Biological Sciences*, 352(1351):391–417, 1997.
  - [30] Leonard Bosgraaf and Peter JM Van Haastert. A model for cGMP signal transduction in *Dictyostelium* in perspective of 25 years of cGMP research. *Journal of Muscle Research & Cell Motility*, 23(7-8):781–791, 2002.
  - [31] Marcelo Behar, Nan Hao, Henrik G Dohlman, and Timothy C Elston. Mathematical and computational analysis of adaptation via feedback inhibition in signal transduction pathways. *Biophysical Journal*, 93(3):806–821, 2007.
  - [32] Aiman Alam-Nazki and J. Krishnan. A mathematical modelling framework for understanding chemorepulsive signal transduction in *Dictyostelium*. *Journal of Theoretical Biology*, 266(1):140 – 153, 2010.

- [33] Guillaume Charras and Erik Sahai. Physical influences of the extracellular environment on cell migration. *Nature Reviews Molecular Cell Biology*, 15(12):813–824, Oct 2014.
- [34] Sophie Cornillon, Romain Froquet, and Pierre Cosson. Involvement of Sib proteins in the regulation of cellular adhesion in *Dictyostelium discoideum*. *Eukaryotic Cell*, 7(9):1600–1605, 2008.
- [35] Petra Fey, Stephen Stephens, Margaret A. Titus, and Rex L. Chisholm. SadA, a novel adhesion receptor in *Dictyostelium*. *The Journal of Cell Biology*, 159(6):1109–1119, Dec 2002.
- [36] Kaplan Test Prep. *MCAT Biochemistry Review 2022-2023: Online + Book*. Kaplan Publishing, New York, NY, 2021.
- [37] Bart Vanhaesebroeck, Julie Guillermet-Guibert, Mariona Graupera, and Benoit Bilanges. The emerging mechanisms of isoform-specific PI3K signalling. *Nature reviews Molecular cell biology*, 11(5):329, 2010.
- [38] David A. Fruman, Honyin Chiu, Benjamin D. Hopkins, Shubha Bagrodia, Lewis C. Cantley, and Robert T. Abraham. The PI3K pathway in human disease. *Cell*, 170(4):605 – 635, 2017.
- [39] Carsten Brock, Michael Schaefer, H Peter Reusch, Cornelia Czupalla, Manuela Michalke, Karsten Spicher, Günter Schultz, and Bernd Nürnberg. Roles of G $\beta\gamma$  in membrane recruitment and activation of p110 $\gamma$ /p101 phosphoinositide 3-kinase  $\gamma$ . *The Journal of Cell Biology*, 160(1):89–99, 2003.
- [40] Peter N Devreotes, Sayak Bhattacharya, Marc Edwards, Pablo A Iglesias, Thomas Lampert, and Yuchuan Miao. Excitable signal transduction networks in directed cell migration. *Annual Review of Cell and Developmental Biology*, 33:103–125, 2017.
- [41] Miho Iijima and Peter Devreotes. Tumor suppressor PTEN mediates sensing of chemoattractant gradients. *Cell*, 109(5):599–610, 2002.
- [42] Günther Gerisch, Britta Schroth-Diez, Annette Müller-Taubenberger, and Mary Ecke. PIP3 waves and PTEN dynamics in the emergence of cell polarity. *Biophysical Journal*, 103(6):1170–1178, 2012.
- [43] Hoai-Nghia Nguyen, Yashar Afkari, Hiroshi Senoo, Hiromi Sesaki, Peter N Devreotes, and Miho Iijima. Mechanism of human PTEN localization revealed by heterologous expression in *Dictyostelium*. *Oncogene*, 33(50):5688, 2014.

- [44] Jr-Ming Yang, Hoai-Nghia Nguyen, Hiromi Sesaki, Peter N Devreotes, and Miho Iijima. Engineering PTEN function: membrane association and activity. *Methods*, 77:119–124, 2015.
- [45] Harriët M Loovers, Kees Veenstra, Helena Snippe, Xavier Pesesse, Christophe Erneux, and Peter JM Van Haastert. A diverse family of inositol 5-phosphatases playing a role in growth and development in *Dictyostelium discoideum*. *Journal of Biological Chemistry*, 278(8):5652–5658, 2003.
- [46] Satomi Matsuoka and Masahiro Ueda. Mutual inhibition between PTEN and PIP3 generates bistability for polarity in motile cells. *Nature Communications*, 9(1):4481, 2018.
- [47] Satoru Funamoto, Ruedi Meili, Susan Lee, Lisa Parry, and Richard A Firtel. Spatial and temporal regulation of 3-phosphoinositides by PI 3-kinase and PTEN mediates chemotaxis. *Cell*, 109(5):611–623, 2002.
- [48] Atsuo T Sasaki, Chris Janetopoulos, Susan Lee, Pascale G Charest, Kosuke Takeda, Lauren W Sundheimer, Ruedi Meili, Peter N Devreotes, and Richard A Firtel. G protein–independent Ras/PI3K/F-actin circuit regulates basic cell motility. *The Journal of Cell Biology*, 178(2):185–191, 2007.
- [49] Atsuo T Sasaki, Cheryl Chun, Kosuke Takeda, and Richard A Firtel. Localized Ras signaling at the leading edge regulates PI3K, cell polarity, and directional cell movement. *J Cell Biol*, 167(3):505–518, 2004.
- [50] Hiroshi Senoo, Huaqing Cai, Yu Wang, Hiromi Sesaki, and Miho Iijima. The novel RacE-binding protein GflB sharpens Ras activity at the leading edge of migrating cells. *Molecular Biology of the Cell*, 27(10):1596–1605, 2016.
- [51] Peter JM Van Haastert and Peter N Devreotes. Chemotaxis: signalling the way forward. *Nature Reviews Molecular Cell Biology*, 5(8):626, 2004.
- [52] Surya P Amarachinthra. *Cellular architecture and cytoskeletal structures involved in cell haptotaxis*. PhD thesis, Bowling Green State University, 2012.
- [53] Johanna Funk, Felipe Merino, Larisa Venkova, Pablo Vargas, Stefan Raunser, Matthieu Piel, and Peter Bieling. Profilin and formin constitute a pacemaker system for robust actin filament growth. *bioRxiv*, 2019.
- [54] Klemens Rottner and Matthias Schaks. Assembling actin filaments for protrusion. *Current Opinion in Cell Biology*, 56:53–63, 2019.
- [55] Dennis Breitsprecher and Bruce L. Goode. Formins at a glance. *Journal of Cell Science*, 126(1):1–7, 2013, <https://jcs.biologists.org/content/126/1/1.full.pdf>.

- [56] Marie-France Carlier and Shashank Shekhar. Global treadmilling coordinates actin turnover and controls the size of actin networks. *Nature Reviews Molecular Cell Biology*, 18(6):389, 2017.
- [57] Peter Bieling, Scott D Hansen, Orkun Akin, Carl C Hayden, Daniel A Fletcher, R Dyche Mullins, et al. WH2 and proline-rich domains of WASP-family proteins collaborate to accelerate actin filament elongation. *The EMBO Journal*, 37(1):102–121, 2018.
- [58] Andrew J Davidson, Clelia Amato, Peter A Thomason, and Robert H Insall. WASP family proteins and formins compete in pseudopod- and bleb-based migration. *J Cell Biol*, 217(2):701–714, 2018.
- [59] Nagendran Ramalingam, Christof Franke, Evelin Jaschinski, Moritz Winterhoff, Yao Lu, Stefan Brühmann, Alexander Junemann, Helena Meier, Angelika A Noegel, Igor Weber, et al. A resilient formin-derived cortical actin meshwork in the rear drives actomyosin-based motility in 2D confinement. *Nature communications*, 6:8496, 2015.
- [60] Michael C Weiger and Carole A Parent. Phosphoinositides in chemotaxis. In *Phosphoinositides II: The Diverse Biological Functions*, pages 217–254. Springer, 2012.
- [61] Kyung Chan Park, Francisco Rivero, Ruedi Meili, Susan Lee, Fabio Apone, and Richard A Firtel. Rac regulation of chemotaxis and morphogenesis in *Dictyostelium*. *The EMBO Journal*, 23(21):4177–4189, 2004.
- [62] Günther Gerisch. Self-organizing actin waves that simulate phagocytic cup structures. *PMC Biophysics*, 3(1):7, 2010.
- [63] Günther Gerisch, Till Bretschneider, Annette Müller-Taubenberger, Evelyn Simmeth, Mary Ecke, Stefan Diez, and Kurt Anderson. Mobile actin clusters and traveling waves in cells recovering from actin depolymerization. *Biophysical Journal*, 87(5):3493–3503, 2004.
- [64] Günther Gerisch, Mary Ecke, Dirk Wischnewski, and Britta Schroth-Diez. Different modes of state transitions determine pattern in the phosphatidylinositide-actin system. *BMC Cell Biology*, 12(1):42, 2011.
- [65] Markus Lange, Jana Prassler, Mary Ecke, Annette Müller-Taubenberger, and Günther Gerisch. Local Ras activation, PTEN pattern, and global actin flow in the chemotactic responses of over-sized cells. *J Cell Sci*, pages jcs–191148, 2016.

- [66] Mary Ecke and Günther Gerisch. Co-existence of Ras activation in a chemotactic signal transduction pathway and in an autonomous wave-forming system. *Small GTPases*, pages 1–9, 2017.
- [67] Marion Jasnin, Florian Beck, Mary Ecke, Yoshiyuki Fukuda, Antonio Martinez-Sánchez, Wolfgang Baumeister, and Günther Gerisch. The architecture of traveling actin waves revealed by cryo-electron tomography. *Structure*, 2019.
- [68] Matthias Gerhardt, Mary Ecke, Michael Walz, Andreas Stengl, Carsten Beta, and Günther Gerisch. Actin and PIP3 waves in giant cells reveal the inherent length scale of an excited state. *J Cell Sci*, pages jcs–156000, 2014.
- [69] Carsten Conradi, Elisenda Feliu, Maya Mincheva, and Carsten Wiuf. Identifying parameter regions for multistationarity. *PLoS Computational Biology*, 13(10):e1005751, 2017.
- [70] Alicia Dickenstein, Mercedes Perez Millan, Anne Shiu, and Xiaoxian Tang. Multistationarity in structured reaction networks. *Bulletin of Mathematical Biology*, 81(5):1527–1581, 2019.
- [71] Carsten Conradi, Nida Obatake, Anne Shiu, and Xiaoxian Tang. Dynamics of ERK regulation in the processive limit. *ArXiv preprint:1910.14452*, 2019.
- [72] Michael Marcondes de Freitas, Elisenda Feliu, and Carsten Wiuf. Intermediates, catalysts, persistence, and boundary steady states. *Journal of Mathematical Biology*, 74(4):887–932, Aug 2016.
- [73] Hans G Othmer. A graph-theoretic analysis of chemical reaction networks. *Lecture Notes, Rutgers University*, 1:36, 1979.
- [74] Mercedes Pérez Millán and Alicia Dickenstein. The structure of MESSI biological systems. *SIAM Journal on Applied Dynamical Systems*, 17(2):1650–1682, 2018, <https://doi.org/10.1137/17M1113722>.
- [75] Chuan-Hsiang Huang, Ming Tang, Changji Shi, Pablo A Iglesias, and Peter N Devreotes. An excitable signal integrator couples to an idling cytoskeletal oscillator to drive cell migration. *Nature Cell Biology*, 15(11):1307–1316, 2013.
- [76] Marco A Avila Ponce de León, Bryan Félix, and Hans G Othmer. A phosphoinositide-based model of actin waves in frustrated phagocytosis. *Journal of Theoretical Biology*, 527:110764, 2021.
- [77] Margarethakay Scavello, Alexandra R Petlick, Ramya Ramesh, Valery F Thompson, Pouya Lotfi, and Pascale G Charest. Protein kinase A regulates the Ras,

- Rap1 and TORC2 pathways in response to the chemoattractant cAMP in *Dictyostelium*. *J Cell Sci*, 130(9):1545–1558, 2017.
- [78] Michael I. Monine and Jason M. Haugh. Signal transduction at point-blank range: Analysis of a spatial coupling mechanism for pathway crosstalk. *Biophysical Journal*, 95(5):2172 – 2182, 2008.
- [79] Michael P Czech. PIP2 and PIP3: complex roles at the cell surface. *Cell*, 100(6):603–606, 2000.
- [80] Hironori Inaba, Koji Yoda, and Hiroyuki Adachi. The F-actin-binding RapGEF GflB is required for efficient macropinocytosis in Dictyostelium. *Journal of Cell Science*, 130(18):3158–3172, 09 2017, <https://journals.biologists.com/jcs/article-pdf/130/18/3158/1921977/jcs194126.pdf>.
- [81] Adriana T Dawes and Leah Edelstein-Keshet. Phosphoinositides and Rho proteins spatially regulate actin polymerization to initiate and maintain directed movement in a one-dimensional model of a motile cell. *Biophysical Journal*, 92(3):744–768, 2007.
- [82] Lan Ma, Chris Janetopoulos, Liu Yang, Peter N. Devreotes, and Pablo A. Iglesias. Two complementary, local excitation, global inhibition mechanisms acting in parallel can explain the chemoattractant-induced regulation of PI(3,4,5)P3 response in *Dictyostelium* cells. *Biophysical Journal*, 87(6):3764 – 3774, 2004.
- [83] K.-C. Lee, A. Gopinathan, and J. M. Schwarz. Modeling the formation of in vitro filopodia. *Journal of Mathematical Biology*, 63(2):229–261, Oct 2010.
- [84] Varunyu Khamwiwath, Jifeng Hu, and Hans G. Othmer. A continuum model of actin waves in *Dictyostelium discoideum*. *PLoS ONE*, 8(5):e64272, May 2013.
- [85] C. Bradford Barber, David P. Dobkin, and Hannu Huhdanpaa. The quickhull algorithm for convex hulls. *ACM Transactions on Mathematical Software*, 22(4):469–483, dec 1996.
- [86] Ilya M Sobol. Sensitivity estimates for nonlinear mathematical models. *Mathematical Modelling and Computational Experiments*, 1(4):407–414, 1993.
- [87] Jan Faix, Dennis Breitsprecher, Theresia EB Stradal, and Clemens Rottner. Filopodia: Complex models for simple rods. *The International Journal of Biochemistry & Cell Biology*, 41(8-9):1656–1664, 2009.
- [88] Ohad Medalia, Martin Beck, Mary Ecke, Igor Weber, Ralph Neujahr, Wolfgang Baumeister, and Günther Gerisch. Organization of actin networks in intact filopodia. *Current Biology*, 17(1):79–84, 2007.

- [89] Changsong Yang and Tatyana Svitkina. Filopodia initiation: focus on the arp2/3 complex and formins. *Cell Adhesion & Migration*, 5(5):402–408, 2011.
- [90] Kwonmoo Lee, Jennifer L. Gallop, Komal Rambani, and Marc W. Kirschner. Self-assembly of filopodia-like structures on supported lipid bilayers. *Science*, 329(5997):1341–1345, 2010.
- [91] Junmin Lee, Amr A Abdeen, Kathryn L Wycislo, Timothy M Fan, and Kristopher A Kilian. Interfacial geometry dictates cancer cell tumorigenicity. *Nature Materials*, 15(8):856–862, 2016.
- [92] Kristopher A Kilian, Branimir Bugarija, Bruce T Lahn, and Milan Mrksich. Geometric cues for directing the differentiation of mesenchymal stem cells. *Proceedings of the National Academy of Sciences*, 107(11):4872–4877, 2010.
- [93] Judah Folkman and Anne Moscona. Role of cell shape in growth control. *Nature*, 273(5661):345–349, 1978.
- [94] Ewa Sitarska. *Deciphering the role of curvature-sensitive BAR domain proteins for cell migration*. PhD thesis, Ruperto Carola University, 2022.
- [95] Alen Trubelja and Gang Bao. Molecular mechanisms of mechanosensing and mechanotransduction in living cells. *Extreme Mechanics Letters*, 20:91–98, 2018.
- [96] Kevin S Cannon, Benjamin L Woods, John M Crutchley, and Amy S Gladfelter. An amphipathic helix enables septins to sense micrometer-scale membrane curvature. *Journal of Cell Biology*, 218(4):1128–1137, 2019.
- [97] Klaus Futterer and Laura Machesky. “Wunder” F-BAR domains: going from pits to vesicles. *Cell*, 129(4):655–657, 2007.
- [98] Hunter Elliott, Robert S Fischer, Kenneth A Myers, Ravi A Desai, Lin Gao, Christopher S Chen, Robert S Adelstein, Clare M Waterman, and Gaudenz Danuser. Myosin ii controls cellular branching morphogenesis and migration in three dimensions by minimizing cell-surface curvature. *Nature Cell Biology*, 17(2):137–147, 2015.
- [99] Richard A Tyson, Evgeny Zatulovskiy, Robert R Kay, and Till Bretschneider. How blebs and pseudopods cooperate during chemotaxis. *Proceedings of the National Academy of Sciences*, 111(32):11703–11708, 2014.
- [100] Cas van der Putten, Maike Werner, Daniëlle van den Broek, Carlijn Bouten, and Nicholas A Kurniawan. Curvature dynamically regulates cell migration mode and motility. *Biophysical Journal*, 121(3):315a, 2022.

- [101] Tianchi Chen. *Large Scale Curvature Sensing in Cell Migration*. PhD thesis, National University of Singapore (Singapore), 2017.
- [102] Gillian L Ryan, Naoki Watanabe, and Dimitrios Vavylonis. A review of models of fluctuating protrusion and retraction patterns at the leading edge of motile cells. *Cytoskeleton*, 69(4):195–206, 2012.
- [103] Shiro Suetsugu, Shusaku Kurisu, and Tadaomi Takenawa. Dynamic shaping of cellular membranes by phospholipids and membrane-deforming proteins. *Physiological Reviews*, 94(4):1219–1248, 2014.
- [104] Yosuke Senju and Pekka Lappalainen. Regulation of actin dynamics by pi (4, 5) p2 in cell migration and endocytosis. *Current Opinion in Cell Biology*, 56:7–13, 2019.
- [105] Thomas Pokrant, Jens Ingo Hein, Sarah Körber, Andrea Disanza, Andreas Pich, Giorgio Scita, Klemens Rottner, and Jan Faix. Ena/vasp clustering at microspike tips involves lamellipodin but not i-bar proteins, and absolutely requires unconventional myosin-x. *bioRxiv*, 2022.
- [106] Margaret Clarke, Ulrike Engel, Jennifer Giorgione, Annette Müller-Taubenberger, Jana Prassler, Douwe Veltman, and Günther Gerisch. Curvature recognition and force generation in phagocytosis. *BMC Biology*, 8(1):1–22, 2010.
- [107] Nir S Gov and Ajay Gopinathan. Dynamics of membranes driven by actin polymerization. *Biophysical Journal*, 90(2):454–469, 2006.
- [108] Roie Shlomovitz and NS Gov. Membrane waves driven by actin and myosin. *Physical Review Letters*, 98(16):168103, 2007.
- [109] Esa Kuusela and Wolfgang Alt. Continuum model of cell adhesion and migration. *Journal of Mathematical Biology*, 58(1):135–161, 2009.
- [110] Xenia Meshik, Patrick R O’Neill, and N Gautam. Physical plasma membrane perturbation using subcellular optogenetics drives integrin-activated cell migration. *ACS Synthetic Biology*, 8(3):498–510, 2019.
- [111] Anika Steffen, Jan Faix, Guenter P Resch, Joern Linkner, Juergen Wehland, J Victor Small, Klemens Rottner, and Theresia EB Stradal. Filopodia formation in the absence of functional wave-and arp2/3-complexes. *Molecular Biology of the Cell*, 17(6):2581–2591, 2006.
- [112] Erdinç Atilgan, Denis Wirtz, and Sean X Sun. Mechanics and dynamics of actin-driven thin membrane protrusions. *Biophysical Journal*, 90(1):65–76, 2006.

- [113] Thomas E Schaus, Edwin W Taylor, and Gary G Borisy. Self-organization of actin filament orientation in the dendritic-nucleation/array-treadmilling model. *Proceedings of the National Academy of Sciences*, 104(17):7086–7091, 2007.
- [114] Leigh Gebbie, Mohammed Benghezal, Sophie Cornillon, Romain Froquet, Nathalie Cherix, Marilyne Malbouyres, Yaya Lefkir, Christophe Grangeasse, Sébastien Fache, Jeremie Dalous, et al. Phg2, a kinase involved in adhesion and focal site modeling in dictyostelium. *Mol. Biol. Cell*, 15(8):3915–3925, 2004.
- [115] Jörg Albuschies and Viola Vogel. The role of filopodia in the recognition of nanotopographies. *Scientific Reports*, 3(1):1–9, 2013.
- [116] Naoki Tamemoto and Hiroshi Noguchi. Reaction-diffusion waves coupled with membrane curvature. *Soft Matter*, 17(27):6589–6596, 2021.
- [117] Anotida Madzvamuse, Eamonn A Gaffney, and Philip K Maini. Stability analysis of non-autonomous reaction-diffusion systems: the effects of growing domains. *Journal of Mathematical Biology*, 61(1):133–164, 2010.
- [118] Daniel T Gillespie. Stochastic simulation of chemical kinetics. *Annu. Rev. Phys. Chem.*, 58:35–55, 2007.
- [119] Thomas D Pollard, Laurent Blanchoin, and R Dyche Mullins. Molecular mechanisms controlling actin filament dynamics in nonmuscle cells. *Annual Review of Biophysics and Biomolecular Structure*, 29(1):545–576, 2000.
- [120] Yadolah Dodge and Daniel Commenges. *The Oxford Dictionary of Statistical Terms*. Oxford University Press on Demand, 2006.
- [121] Andrea Saltelli, Paola Annoni, Ivano Azzini, Francesca Campolongo, Marco Ratto, and Stefano Tarantola. Variance based sensitivity analysis of model output. Design and estimator for the total sensitivity index. *Computer Physics Communications*, 181(2):259–270, 2010.
- [122] F Kuo, I Sloan, Grzegorz Wasilkowski, and Henryk Woźniakowski. On decompositions of multivariate functions. *Mathematics of Computation*, 79(270):953–966, 2010.
- [123] Eusebius J Doedel. Lecture notes on numerical analysis of nonlinear equations. In *Numerical Continuation Methods for dynamical systems*, pages 1–49. Springer, 2007.

## Appendix A

---

### *Sensitivity Analysis*

In the case of mechanistic biological models, one faces the challenge of fixing values to parameters that are yet to be determined experimentally. Therefore, one should be skeptical and proceed with care in regard to predictions. To better understand how much the output of a model depends on the choice of parameters, one can make use of variance-based sensitivity analysis. This analysis accommodates the variance of the model's output into its parameters. Thus, one can infer how sensitive the model is to a parameter of interest; for example, one that was arbitrarily fixed. Below, we will summarize the method of Sobol [86]. This method allows us to compute, for a given model, the sensitivity indices of its respective parameters.

Let  $\mathbf{x} = x_1, x_2, \dots, x_n$  be the parameter set to consider. For simplicity and exposition we will assume that these are uniformly distributed between  $[0, 1]$ . Indeed, any continuous distribution can be mapped to an uniform distribution by an appropriate transformation [120]. Now, consider a real valued function  $f : \mathbf{K}^n \rightarrow \mathbf{R}$ , with  $\mathbf{K}^n$  being the  $n$ -dimensional unit-hypercube:

$$\mathbf{K}^n = \{\mathbf{x} \mid 0 \leq x_i \leq 1; i = 1, 2, \dots, n\}.$$

We will prove that the function  $f$  can be decomposed into a sum of terms in increasing dimension, and we describe the computation algorithms as introduced in [86] and [121].

To begin, we have the following definition:

**Definition A.0.1** (Summand expansion of  $f$ ). *The function  $f : \mathbf{K}^n \rightarrow \mathbf{R}$  defined by the map  $\mathbf{x} \mapsto f(\mathbf{x})$ , is said to admit a summand expansion if there exists functions  $f_{i_1, i_2, \dots, i_s}(x_{i_1}, x_{i_2}, \dots, x_{i_s})$ , such that*

$$f(\mathbf{x}) = f_0 + \sum_{i=1}^n f_i(x_i) + \sum_{i=1}^{n-1} \sum_{j=i+1}^n f_{i,j}(x_i, x_j) + \sum_{i=1}^{n-2} \sum_{j=i+1}^{n-1} \sum_{k=j+1}^n f_{i,j,k}(x_i, x_j, x_k) + \dots \quad (\text{A.1})$$

with  $f_0$  a constant, and with the property that, for any  $f_{i_1, i_2, \dots, i_s}$  we have:

$$\int_0^1 f_{i_1, i_2, \dots, i_s}(x_{i_1}, x_{i_2}, \dots, x_{i_s}) dx_{i_k} = 0 \quad 1 \leq k \leq s \quad (\text{A.2})$$

The expansion above consists of  $2^n$  terms. Such an expansion exist whenever  $f$  is an square-integrable function over  $\mathbf{K}^n$ . In what follows we use the convention of [86] where an

---

integral, taken over all variables  $x_i$ , except for  $x_j$  is denoted as  $d\mathbf{x}/dx_j$ . Then, the functions  $f_{i_1, i_2, \dots, i_s}$  can be computed in a recursive way as follows. Starting with the constant  $f_0$ , we define its value to be:

$$f_0 = \int_{\mathbf{K}^n} f(\mathbf{x}) d\mathbf{x}.$$

Through these definitions, one should note that these are uniquely defined, given that  $f \in L^2(\mathbf{K}^n)$ . Moving in increasing dimensionality of the arguments, for  $i \in \{1, 2, \dots, n\}$  we let

$$f_i(x_i) = \int_{\mathbf{K}^{n-1}} f(\mathbf{x}) \frac{d\mathbf{x}}{dx_i} - f_0.$$

Continuing in a similar way, we define the functions  $f_{i,j}(x_i, x_j)$  as

$$f_{i,j}(x_i, x_j) = \int_{\mathbf{K}^{n-2}} f(\mathbf{x}) \frac{d\mathbf{x}}{dx_i dx_j} - f_i(x_i) - f_j(x_j) - f_0,$$

and so on. It is easy to see that the definition above satisfies requirement A.2. Moreover, we see that the functions  $f_{i_1, i_2, \dots, i_s}$  are pairwise orthogonal in  $L^2(\mathbf{K}^n)$ . Thus, we see that the representation A.1 is valid in  $L^2(\mathbf{K}^n)$  [122].

Equipped with representation A.1 for  $f$ , we define its total variance as:

$$D(f) = \int_{\mathbf{K}^n} f^2(\mathbf{x}) d\mathbf{x} - \left( \int_{\mathbf{K}^n} f(\mathbf{x}) d\mathbf{x} \right)^2. \quad (\text{A.3})$$

Note that the latter integral is equivalent to  $(f_0)^2$  while the former can be simplified by the orthogonal properties of the functions (equation (A.2)). Explicitly, we get

$$D(f) = \sum_{i=1}^n \int_{\mathbf{K}} f_i^2 d\mathbf{x}_i + \sum_{i=1}^{n-1} \sum_{j=i+1}^n \int_{\mathbf{K}^2} f_{i,j}^2 d\mathbf{x}_i d\mathbf{x}_j + \quad (\text{A.4})$$

$$\sum_{i=1}^{n-2} \sum_{j=i+1}^{n-1} \sum_{k=j+1}^n \int_{\mathbf{K}^3} f_{i,j,k}^2 d\mathbf{x}_i d\mathbf{x}_j d\mathbf{x}_k + \dots. \quad (\text{A.5})$$

Note the similarity with representation (A.1). Following the interpretation of [86], we see the representation above as a distribution of the total variance among combinations of the variables  $x_i$ , in increasing order of dimension. Thus, it makes sense to define the sensitivity indices:

$$S_{i_1, i_2, \dots, i_s} = \frac{1}{D(f)} \int_{\mathbf{K}^n} f_{i_1, i_2, \dots, i_s}^2 d\mathbf{x}, \quad (\text{A.6})$$

Where  $S_{i_1, i_2, \dots, i_s}$  ranges between 0 and 1. This gives rise to the *main, or first order effect indices* and *total effect indices*.

---

**Definition A.0.2.** (*First order index*) For a function  $f(x_1, x_2, \dots, x_n)$ , the main, or first order effect index for  $x_i$  is defined as

$$S_i = \frac{1}{D(f)} \int_{\mathbf{K}} f_i^2 dx_i.$$

The total effect index has a more awkward definition, but is to be interpreted as the total contribution of  $x_i$  on the variance of  $f$ . That is, we sum over all indices that depend on  $x_i$ . Thus, we have the following definition

**Definition A.0.3.** (*Total effect index*) For a function  $f(x_1, x_2, \dots, x_n)$ , the total, effect index for  $x_i$  is defined as

$$S_{Ti} = \sum_{\substack{I \subseteq \{1, 2, \dots, n\} \\ i \in I}} S_I. \quad (\text{A.7})$$

One may ponder that the computation of each individual term in (A.1) is computationally expensive, and indeed it is. However, if we only care about computing the main and total sensitivity indices to a particular parameter, then we can get away with computing only four integrals; two in order to compute the variance of  $f$ , and two more to compute the necessary indices as we will show below. In particular, we will show that all these integrals can be made dependent on  $f$  only. The computation then is amenable to Monte-Carlo approximations.

Now, consider a particular variable of interest  $x_p$ , and divide the parameters into two sets  $y$ , and  $z$ , with  $y = x_p$ , and  $z$  equal to the rest of the variables. We then inspect the decomposition of  $f$  as

$$f(\mathbf{x}) = f_0 + f_1(y) + f_2(z) + f_{1,2}(y, z).$$

It will follow that its sensitivity decomposition is of the form

$$1 = S_1 + S_2 + S_{1,2}.$$

Observe then, that the main effect of  $x_p = y$  coincides with  $S_1$  and the total effect  $S_{Ti} = S_1 + S_{1,2}$  can be determined as  $1 - S_2$ . In order to set the stage for a Monte-Carlo approximation, we note the following relations of  $S_1$  and  $S_2$ . First,

$$D(f)S_1 = \int_{\mathbf{K}} \left( \int_{\mathbf{K}^{n-1}} f(\mathbf{x}) dz \right)^2 dy - f_0^2 \quad (\text{A.8})$$

$$= \int_{\mathbf{K}^{2n-1}} f(y, z) f(y, v) dz dv dy - f_0^2 \quad (\text{A.9})$$

and similarly,

$$D(f)S_2 = \int_{\mathbf{K}^{n-1}} \left( \int_{\mathbf{K}^1} f(\mathbf{x}) dy \right)^2 dz - f_0^2 \quad (\text{A.10})$$

---


$$= \int_{\mathbf{K}^{n+1}} f(y, z) f(u, z) dy du dz, -f_0^2 \quad (\text{A.11})$$

with  $u \in \mathbf{K}$  and  $v \in \mathbf{K}^{n-1}$ . Thus, with all integrals being dependent on  $f$  only, we pose the following Monte-Carlo approximations, with  $N$  being the sample size:

$$f_0 \approx \frac{1}{N} \sum_{j=1}^N f(y_j, z_j), \quad (\text{A.12})$$

$$D(f) + f_0^2 \approx \frac{1}{N} \sum_{j=1}^N f^2(y_j, z_j), \quad (\text{A.13})$$

$$D(f)S_1 + f_0^2 \approx \frac{1}{N} \sum_{j=1}^N f(y_j, z_j) f(y_j, v_j), \quad (\text{A.14})$$

$$D(f)S_2 + f_0^2 \approx \frac{1}{N} \sum_{j=1}^N f(y_j, z_j) f(u_j, z_j). \quad (\text{A.15})$$

Note that each sample  $j$  will consist on a realization for  $y, z, u$ , and  $v$ . At face value, the number of samples needed for convergence remains an open question. However, in [121] the authors propose guidelines and strategies to speed up the convergence rate.

## Appendix B

---

### *Equilibrium Continuation*

A commonly used technique in bifurcation analysis of dynamical systems is the numerical computation of equilibrium curves. In particular, for highly dimensional nonlinear systems, which often can not be solved analytically. Indeed, if used effectively, equilibrium curves can help uncover essential properties of the system such as stability changes, sensitivity to parameters, regions compatible with unique or multiple steady states, and catastrophic behavior. In the recent decades, software tools have emerged to aid in the application of related techniques such as AUTO, XPP, CONTENT, DDE-BIFTOOL, and MATCONT. Our interest here, is to present an exposition of the theory behind these tools. In what follows, we use the notation in the work of [123].

To begin, consider the dynamical system

$$\frac{dx}{dt} = F(x(t), \lambda),$$

where  $x \in \mathbf{R}^n$ ,  $\lambda \in \mathbf{R}$ , and  $F : \mathbf{R}^{n+1} \rightarrow \mathbf{R}^n$ . We are interested in the solution curve  $(x, \lambda)$  to the system  $F(x, \lambda) = 0$ . All along we will assume  $F$  is continuous and differentiable function. First, we address the local existence and uniqueness for *regular* points along the curve. Thus, we say that a point  $(x_0, \lambda_0)$  satisfying  $F(x, \lambda) = 0$  is *regular* if the augmented  $n \times n + 1$  matrix

$$[F_x \mid F_\lambda] = \left[ \begin{array}{cccc|c} \partial_{x_1} f_1 & \partial_{x_2} f_1 & \cdots & \partial_{x_n} f_1 & \partial_\lambda f_1 \\ \partial_{x_1} f_2 & \partial_{x_2} f_2 & \cdots & \partial_{x_n} f_2 & \partial_\lambda f_2 \\ \vdots & \vdots & \ddots & \vdots & \vdots \\ \partial_{x_1} f_n & \partial_{x_2} f_n & \cdots & \partial_{x_n} f_n & \partial_\lambda f_n \end{array} \right], \quad (\text{B.1})$$

when evaluated at  $(x_0, \lambda_0)$ , has rank equal to  $n$ .

**Lemma B.0.1.** *Let  $(x_0, \lambda_0)$  be a regular point of the solution curve  $F(x, \lambda) = 0$ . Then, there exists a unique one-dimensional continuum of solutions  $(x(s), \lambda(s))$  with  $(x(0), \lambda(0)) = (x_0, \lambda_0)$ .*

*Proof.* Observe that if  $(x_0, \lambda_0)$  is a regular point then, either  $F_x$  is invertible otherwise it's singular. In the former case, the *Implicit Function Theorem* guarantees the existence of a unique  $C^1$  function  $g(\lambda) = x$  around a neighborhood of  $(x_0, \lambda_0)$  such that  $F(g(\lambda), \lambda) = 0$ .

---

In the later case, since  $\text{rank}([\mathbf{F}_x \mid \mathbf{F}_\lambda]) = n$  there exists an  $n$ -dimensional column space of  $[\mathbf{F}_x \mid \mathbf{F}_\lambda]$  that arises from excluding the  $i$ -th column, with  $1 \leq i \leq n$ . Therefore, one can recover the conclusion of the implicit function theorem by parametrizing the solution curve with the variable  $x_i$ .  $\square$

As a first approach, one can compute the solution curve parting from a regular point via Newton's method. However, in order to set up an initial guess we must have at hand one such solution. One can proceed either by inspection, or by running a simulation with appropriate initial conditions long enough to ensure convergence to an equilibrium. Assume then that  $(\mathbf{x}_0, \lambda_0)$  is a regular point to  $\mathbf{F}(\mathbf{x}, \lambda) = 0$  and let  $\lambda_1 = \lambda_0 + \Delta\lambda$ . We wish to solve

$$\mathbf{F}(\mathbf{x}, \lambda_1) = 0$$

for  $\mathbf{x}$ . By Newton's method, the sequence

$$\mathbf{x}^{(n+1)} = \mathbf{x}^{(n)} - \mathbf{F}_x^{-1}(\mathbf{x}^{(n)}, \lambda_1) \cdot \mathbf{F}(\mathbf{x}^{(n)}, \lambda_1)$$

will converge provided that the initial guess  $\mathbf{x}^{(0)}$  is close enough. Indeed, if we set our initial guess to

$$\mathbf{x}^{(0)} = \mathbf{x}_0 + \Delta\lambda \frac{d\mathbf{x}}{d\lambda} \Big|_{(\mathbf{x}_0, \lambda_0)} = \mathbf{x}_0 - \Delta\lambda (\mathbf{F}_x^{-1} \cdot \mathbf{F}_\lambda) \Big|_{(\mathbf{x}_0, \lambda_0)}$$

convergence is guaranteed by Newton's method whenever  $\Delta\lambda$  is small enough. One caveat of this approach is the requirement of  $\mathbf{F}_x$  to be non-singular. Such is not the case for *fold points* along the solution curve. Of course, one can choose a different continuation variable to get around the problem however, this is non-practical for computational considerations.

To allow continuation past fold points, the *pseudo-arc length continuation* is often preferred. In fact, current software use but slight variations of this approach. For example, the Moore-Penrose method employed by MATCONT.

We presume that the curve  $(\mathbf{x}, \lambda)$  can be parametrized by a natural arclength parameter  $s$ . As before, we presume that we can get ahold of a solution  $(\mathbf{x}_0, \lambda_0)$ . Additionally, we will need a direction vector  $(dx/ds, d\lambda/ds)$ . Analogous to the previous method we set up a system amenable to Newton's method. Note however, that we won't be fixing the value for  $\lambda_1$  a priori. Thus, we need to impose an extra constraint to the system  $\mathbf{F}(\mathbf{x}_1, \lambda_1) = 0$  to admit a unique solution. Indeed, many choices can be made, one common choice is to require that  $(\mathbf{x}_1, \lambda_1)$  lies on the hyperplane perpendicular to  $(dx/ds, d\lambda/ds)$  (see Figure B.1). Thus, we wish to solve

$$\begin{cases} \mathbf{F}(\mathbf{x}_1, \lambda_1) = 0 \\ \left\langle (\mathbf{x}_1 - \mathbf{x}_0, \lambda_1 - \lambda_0), \left( \frac{d\mathbf{x}}{ds}, \frac{d\lambda}{ds} \right) \Big|_{(\mathbf{x}_0, \lambda_0)} \right\rangle = 0 \end{cases} \quad (\text{B.2})$$

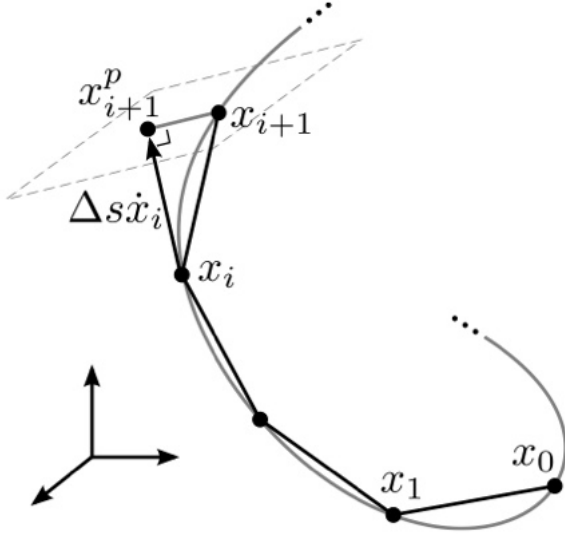


**Figure B.1:** Graphical representation of the pseudo-arc-length method.

where  $\langle \cdot, \cdot \rangle$  denotes the inner product. As before, we can solve this system by Newton's method. As our initial guess we set  $\mathbf{x}_1^{(0)}, \lambda_1^{(0)}$  to be

$$\mathbf{x}_1^{(0)}, \lambda_1^{(0)} = \mathbf{x}_0, \lambda_0 + \Delta s \left( \frac{d\mathbf{x}}{ds}, \frac{d\lambda}{ds} \right) \Big|_{(\mathbf{x}_1, \lambda_1)}$$

where  $\Delta s$  is our step size in the direction of the arclength. Once we find  $(\mathbf{x}_1, \lambda_1)$  we can find its corresponding direction vector by solving the system

$$\left[ \begin{array}{c|c} F_{\mathbf{x}}(\mathbf{x}_1, \lambda_1) & F_{\lambda}(\mathbf{x}_1, \lambda_1) \\ \hline d\mathbf{x}/ds(\mathbf{x}_0) & d\lambda/ds(\lambda_0) \end{array} \right] \left( \frac{d\mathbf{x}}{ds}, \frac{d\lambda}{ds} \right)^T \Big|_{(\mathbf{x}_1, \lambda_1)} = \left[ \begin{array}{c} \mathbf{0} \\ 1 \end{array} \right]$$

where the superscript T denotes transpose. We note that the direction vector should be normalized for good convergence.